New methods for optimizing parallel transmit/receive array coils to small field-of-view excitation for breast and cardiac MRI

by

Pei-Shan Wei

A Thesis submitted to the Faculty of Graduate Studies of

The University of Manitoba

in partial fulfilment of the requirements of the degree of

DOCTOR OF PHILOSOPHY

Department of Physics and Astronomy

University of Manitoba

Winnipeg, Canada

Abstract

In this thesis, we designed new methods for optimizing a coil array that is both transmit and receive and is intended for imaging the breasts and the heart. In particular, we focused on optimizing the array for the application of small field-of-view (FOV) excitation, which allows zooming into a region-of-interest (ROI). As a result, such an array is able to provide higher spatial resolution to diagnose breast tumors and higher temporal resolution to diagnose coronary artery diseases. To achieve this goal, we investigated inductive coupling between array elements, specific absorption rate (SAR) of radiofrequency (RF) power and RF pulse design.

Inductive coupling between coil elements is detrimental to a coil's performance and must be carefully considered in coil optimization for both RF transmission and signal reception. For evaluation, we simulated a two-channel saddle coil array to determine the impact of inductive coupling on the noise correlation matrix. A two-channel coil, which was identical to the simulated model, was constructed to verify the simulation. The coil was characterized on the bench for validating tuning and matching. Inductive coupling was varied by altering the overlapping position of coil elements and by using a preamplifier circuit. We found that the noise correlation coefficient was predictable at different overlapping positions when properly coupled electromagnetic (EM) fields for all coil elements were used in the simulation.

For small FOV excitation, a set of a highly tailored RF pulses are required. We developed a new RF pulse design method, which adapted negative excitation artifacts predicted by Bloch-simulation from a previous iteration to pre-compensate artifacts in

next iteration. The results showed that the proposed method reduced excitation artifacts by about 20% outside the ROI. Additionally, we proposed a strategy, using tilted coil elements that generated more symmetrical B_1^+ fields that reduced hot spots. The results showed that by using this strategy in RF coil design, the root-mean square (RMS) error in the excitation artifacts was reduced by about 25%.

RF safety is a major concern for a transmit coil design. In addition to addressing the impact of inductive coupling on a receive coil design, we also investigated the impact of different inductive coupling scenarios on estimation of SAR. We found SAR values were affected by the length of the RF pulse. The results showed that in the worst case, the peak SAR values were underestimated by 40% when extremely short RF pulses were applied. Hence, it is important to incorporate the inductive coupling in RF coil simulations.

Overall we explored several important concepts for RF array and pulse design: the impact of inductive coupling on noise correlation coefficients and on SAR estimation and new strategies to reduce small FOV excitation artifacts. In particular, we have shown that it is critical to include inductive coupling in SAR estimation, something that has previously been ignored in MRI research. The results shown in this thesis provide guidance for RF array design and also for RF pulse design when optimizing for small FOV excitation.

Acknowledgments

A great many people made this work possible. I would like to thank my advisors Dr. Scott King and Dr. Chris Bidinosti for their guidance, advice, encouragement, and enthusiasm.

I would like to thank my committee members: Dr. Boyd McCurdy, Dr. Gabriel Thomas and Dr. Francis Lin for their advice and support throughout the years.

I am indebted to Dr. Daniel Rickey, without whom, much of this work would not have been possible.

I would like to thank Dr. Hung-Yu Lin for his helpful discussions. In addition, I am grateful to Mike Smith for inspiring the development the RF pulse programming.

I would like to thank Jarod Matwiy for help with the construction of RF coil and general lab stuff. I thank Richard Bernhardt, Calvin Bewsky for the discussion of the breast phantom, and Ernie Packulak for assisting of booting and troubleshooting the parallel transmission system.

I would also like to Sheryl Herrera for her friendship and many useful suggestions she made during this project. I also thank Susan Beshta for taking care of all that administrative stuff for me.

I am grateful for the financial support of the Canadian Breast Cancer Foundation, NSERC, and Mitacs.

I am thankful to my parents to my parents, Ching-Fu Wei and Li-Hui Chou who give me their unconditional love and encouragements.

Finally, I would like to thank my husband, Shih-Ting Kan, for his support, understanding, and patience.

Table of contents

List of figures

List of tables

Glossary

B_0	static magnetic field
B_1	magnetic field produced by an RF coil
B_1^+	transmit magnetic field
B_1^-	receive magnetic field
EM	electromagnetic
FDTD	finite-difference time domain
FEM	finite element method
FOV	field-of-view
NCC	noise correlation coefficient
M_0	net magnetization at thermal equilibrium
M_z	longitudinal magnetization along z-axis
M_z	longitudinal magnetization along z-axis
M_{xy}	transverse magnetization in xy plane
MoM	method of moment
MRI	magnetic resonance imaging
RMS	root-mean-square value

RF	radiofrequency
ROI	region-of-interest
Rx	receive
SAR	specific absorption rate
SNR	signal-to-noise ratio
SENSE	sensitivity encoding
TE	echo time
TR	repetition time
Tx	transmit
T1	spin-lattice relaxation time
T2	spin-spin relaxation time
μ	nuclear magnetic dipole moment
γ	gyromagnetic ratio
ω_0	Larmor frequency

Chapter 1: Introduction

The ultimate goal of the work in this thesis is to achieve higher spatial resolution and higher temporal resolution for breast and cardiac MRI. To achieve this, we developed advanced methods to design RF arrays optimized for these purposes. In this chapter we first present the importance of breast and cardiac MRI, then discuss the associated clinical and technical challenges of these techniques, and finally outline the specific research directions explored in this thesis.

1.1 Clinical challenges

The latest report released by *Statistics Canada* states that cancer and cardiovascular diseases (CVDs) have been the number one and two leading causes of death in Canadians since 2000 [1]. The number of deaths due to these diseases is about half of the total number of deaths in Canada. In addition, CVDs are the second most costly in terms of the total health costs from 2000 to 2008. For example, CVDs are responsible for 6.4% ($12.1 billion) of the total health care expenditure in 2008 [2], [3]. Hence, diagnosis, treatment and management of these diseases are important issues and require extensive study.

Magnetic resonance imaging (MRI) is well known for its superb soft tissue contrast and high spatial resolution images that are made without exposure to ionizing radiation, which is itself a risk factor for causing genetic damage and cancer. Consequently, MRI has been widely used in clinics for cancer diagnosis and staging. In addition, MRI is suitable for detecting anatomical and morphological changes caused by cancers and CVDs. However, there is a need for still higher spatial and temporal resolution,

especially in dynamic applications such as breast and cardiac MRI. Because the breasts and the heart are in the chest region, the patient can be in the supine position for some examination. As a result, we chose to focus on an RF array suitable for this purpose. We developed an optimized radiofrequency (RF array and advanced imaging techniques to improve both breast and cardiac imaging when using a three Tesla (3T) MRI scanner, which is presently the highest field strength commonly in use. Ultimately, we hope this work will elevate the quality of patient care.

1.1.1 The breast

The anatomy of a female breast is shown in Figure 1.1. Breasts are composed of areola, adipose tissue (fat), lobules (glands), ducts and connective tissues that surround the lobules and ducts. Each breast has about 15 to 20 sections of lobes where each lobe consists of many lobules, which are responsible for milk production. Ducts are small tubes that transport milk from the lobes to the nipple. The breasts do not include muscle tissue, but they are attached to the chest wall and are supported by ligaments. There are also many blood vessels, lymph nodes and lymph vessels, which form the lymphatic system in breasts [4].

Both men and women have the same structure of breasts, but female breasts have more adipose and glandular tissues. Therefore, men can also develop breast cancer, but it is rare. There are several types of breast cancers; the most common one is called adenocarcinoma, which starts in glandular tissues. Depending if the cancer spreads out from its origin, the cancers are categorized as non-invasive, e.g. ductal carcinoma in situ and invasive types, e.g. invasive lobular carcinoma. These cancers are treatable

with surgery, chemotherapy and radiation therapy. For example, the five-year survival rate for stage 0 patients is almost 100%. However, if the cancer is detected later, the five-year survival rate drops, e.g. to about 70% for stage 3 patients [5].

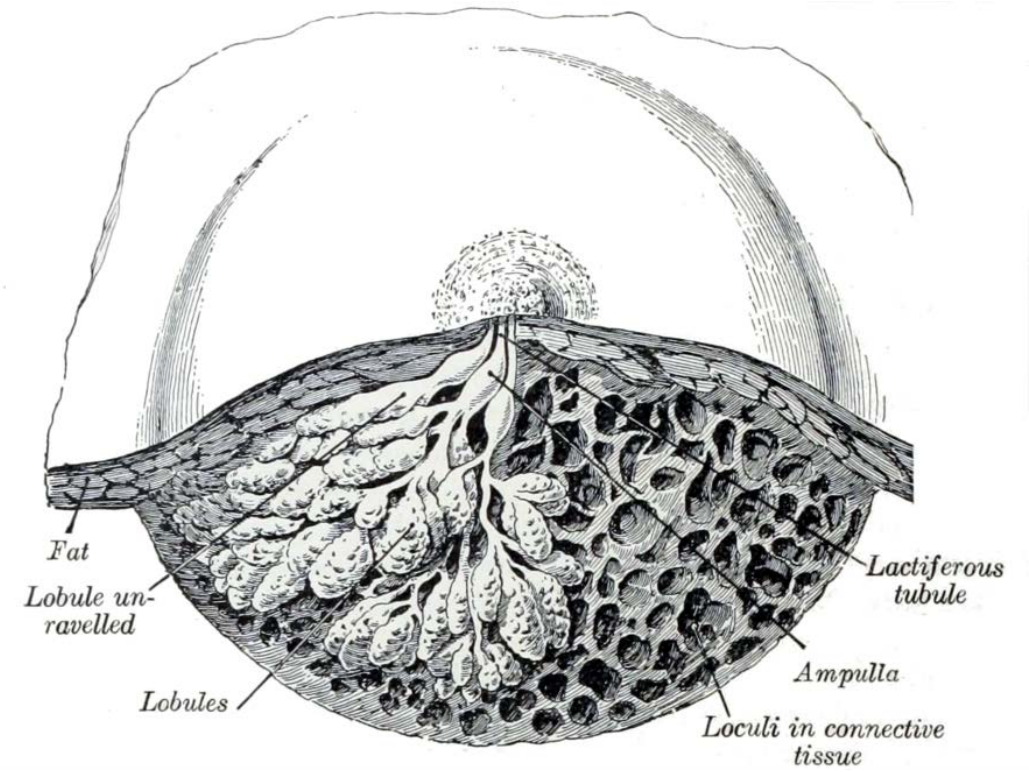

Figure 1.1 Diagram showing the front view of breast anatomy [6].

1.1.1.1Screening of breast cancer

Breast cancer is the most commonly diagnosed cancer in women worldwide [7]. The key to reducing death from breast cancer relies on early detection and proper treatments. Currently, Canadian women in the age range of 50 to 69 years old are in a high-risk population for breast cancer. Thus, they are recommended by the Canadian Cancer Society to receive regular screening tests [4]. Early-stage tumors are very small and patients may not show any symptoms of the disease; as a result, patients may miss

the best time to start treatment. Hence, it is important to have screening tests for early detection.

Mammography is a low-dose X-ray imaging system that is the standard screening tool for examining the breast for cancer (see Figure 1.2). However, it is limited due to a low sensitivity, especially for high-risk young women. Part of the reason is that young women have high density breasts, which mammography struggles with. It also has the problems of exposure to ionizing radiation and being uncomfortable. However, ultrasound imaging is a supplemental tool to mammography. It is not recommended to be used as a screening tool because its sensitivity and specificity are lower than mammography. Ultrasound is useful for distinguishing if a lump detected by mammography is a cyst or a solid mass. Breast MRI is an imaging modality that provides both anatomical and functional information for breast cancer diagnosis and tumor staging. In addition, it has been shown that MRI provides a higher sensitivity than other screening tools for early detection [8].

Figure 1.2 Photograph showing a mammography machine [9]

1.1.1.2 Breast magnetic resonance imaging

The guidance for screening average-risk women with mammography is clear [10]. However, MRI is not recommended for average-risk women because its specificity is modest [11], which leads to high false-positive results. In other words, using MRI for screening will result in more patients presenting with suspicious lesions than when using mammography. These patients will require further tests, i.e. a tissue biopsy, but often the results will be benign. Hence, using MRI as a screening tool may cause unnecessary patient anxiety and waste medical resources. For high-risk woman, the benefit of using MRI along with mammography is convincing [12]–[14] and it is also recommended by the American Cancer Society [5]. However, using MRI along or in combination with mammography is still under debate [15]–[17].

Dynamic contrast-enhanced (DCE) MRI [18] is a standard technique for diagnostic breast imaging. This technique acquires a time series of images that monitors signal changes after an injection of a bolus of contrast agent. Since the contrast agent enhances the signals, by analyzing these images, we can extract pharmacokinetic parameters to characterize the properties of a breast cancer. There are several methods proposed to analyze these images, such as area under the curve (AUC) [19], Toft and Kermode model [20], and general kinetic model [21]. To improve the modest specificity of MRI, it has been shown that using a combination of DCE-MR and diffusion weighted imaging can increase the diagnostic accuracy [15], [22]. More research is in progress to explore different directions to improve the performance of MRI, e.g. development of contrast agents that can target cancer cells and improve MR image contrast [23], [24]

In general, the time required for an MRI examination is much longer than other imaging modalities and leads to low efficiency and high costs for screening. Image quality, quantified by signal-to-noise ratio (SNR) or image resolution, is affected by MRI hardware. If we can provide high image quality and reduce the examination time by implementing advanced imaging technologies, then it is possible to adapt MRI into standard screening programs for early detection of breast cancer and possibly reduce the mortality rate [25].

1.1.2 The heart

The anatomy of a normal heart is shown in Figure 1.3. The heart is a hollow and muscular organ and is located at the center of the chest. The heart is divided into four chambers (two atrium and two ventral) and is connected to blood vessels (arteries and veins). The contraction of the heart wall is triggered by an electrical system. Each contraction pumps the blood through the circulatory system and the direction of blood flow is regulated by valves. The function of the heart is to ensure that the whole body obtains enough oxygen and nutrients to function properly. The size of the heart varies from person to person. In general, the size of a healthy heart is about the size of a fist. However, some diseases lead to an enlarged heart.

1.1.2.1Assessment of coronary artery disease

Coronary artery disease (CAD), also called coronary heart disease or ischemic heart disease is the most common type of heart disease. CAD is caused by a buildup of plaque inside the coronary arteries and results in reduced supply of oxygenated blood to the myocardium. Over time, CAD would likely cause symptoms, such as chest pain

and may lead to heart attack [26]. The development of plaques could take decades; hence, early detection is one of the keys to reduce the risk of death from CAD.

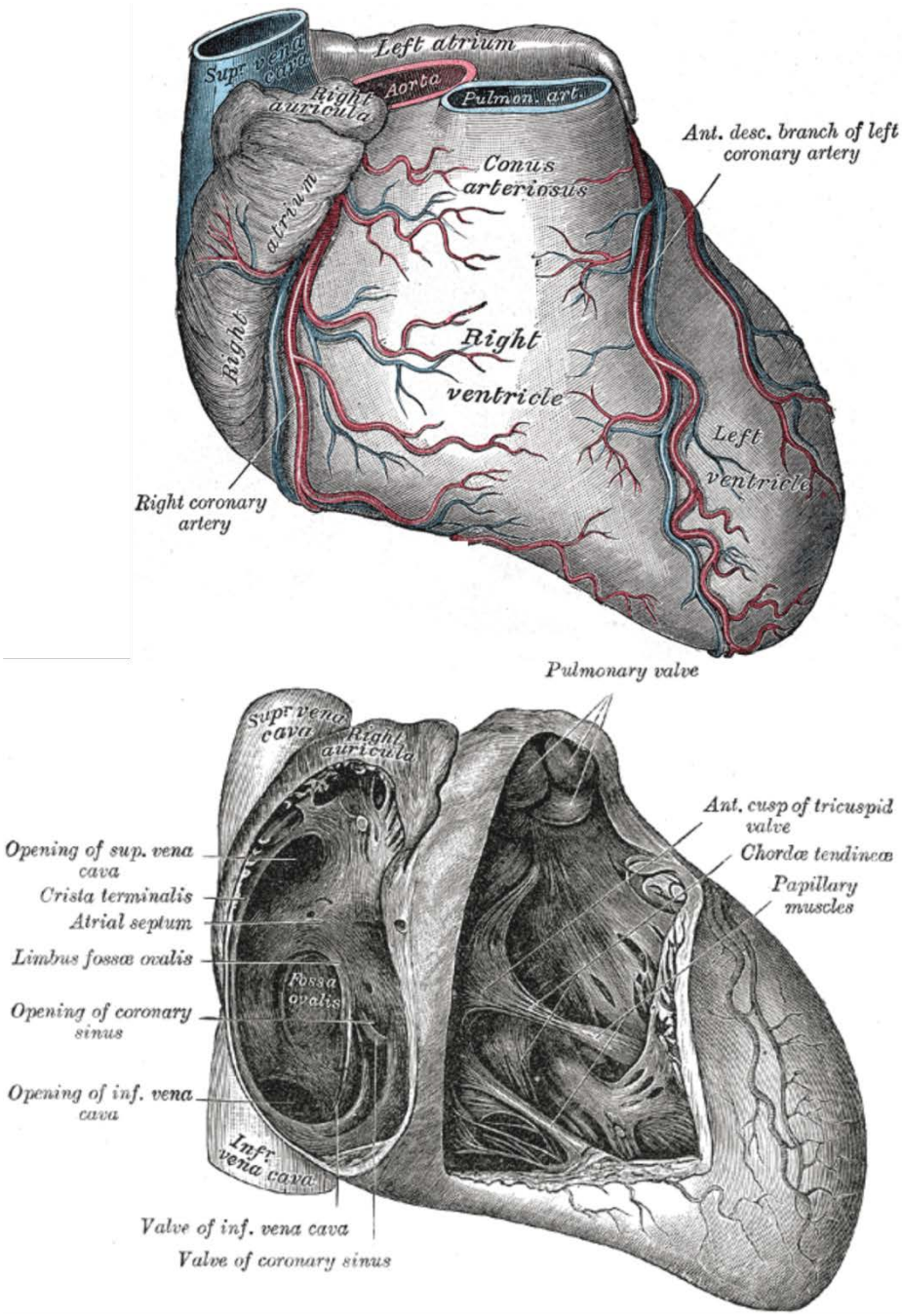

Figure 1.3 Diagram showing parts of vessels (exterior) and myocardium (interior) in the heart [6].

There is no single test that can definitively diagnose CAD. To evaluate the function or anatomy or both of a heart, there are many tests recommended for the patient. These include electrocardiogram, echocardiography, computed tomography angiography and cardiac x-ray angiography. Cardiac MRI is one of the non-invasive imaging techniques that can provide functional and anatomical information. Because of its motion and small blood vessels the heart is difficult to image with MRI. MR is slow, thus it requires development of fast imaging techniques.

1.1.2.2 Cardiac magnetic resonance imaging

Cardiac MRI [27] has been considered a potential tool for the detection of CAD and assessment of myocardial perfusion [28]–[30] because of its high image resolution and lack of radiation exposure. One particular technique is called contrast-enhanced myocardial perfusion first-pass imaging that analyzes serial images during the first pass of a contrast agent. However, there are trade-offs between spatial resolution, temporal resolution, volume coverage, and SNR. These trade-offs are due to a small temporal acquisition window in each cardiac cycle. In addition, the image quality suffers from motion artifacts and susceptibility artefacts. Different accelerated dynamic imaging techniques such as TSENSE [31], k-t SENSE [32], and compressed sensing [33] have been shown to improve these trade-offs. But there is always room for more improvement. Further developments of cardiac MRI could provide a more accurate diagnosis and help subsequent treatment decisions. Therefore, with the assistance of advanced MRI technology, the number of deaths due to CAD could decline.

1.2 Technical limitations of clinical MRI at 3T

Currently, 3T MRI scanners are becoming more common in clinical imaging. The increased field strength offers several advantages, including improved SNR, higher image resolution, and increased contrast-to-noise ratio for advanced applications [34]–[36]. However, scanning at high frequencies is also accompanied by several challenges such as B_1^+ field inhomogeneity from the dielectric effect [4]-[5] and increase SAR. The former appears as a central brightening or darkening within the images [39] which degrades image quality and may obscure pathology. The latter puts stricter limits on RF pulse design to avoid excessive RF heating of the patient and potential burns.

1.2.1 Single-channel RF transmission on a conventional MRI scanner

In a typical MRI scanner, RF pulses are transmitted with a single built-in whole-body birdcage coil that is quadrature-driven. However, such a coil cannot generate a uniform B_1^+ field due to the central brightening effect mentioned above, and therefore has limited application towards small FOV excitation. Moreover achieving small FOV requires very long RF pulses, which when using the whole body coil leads to greater SAR and patient safety concerns. The long pulse duration is also impractical on conventional scanners and will degrade the quality of the excitation profile. Finally it should be pointed out that MRI scanners with signal-channel transmit coil tend not to have the high-performance gradient systems needed to achieve small FOV excitation.

1.2.2 Parallel RF transmission on a prototype scanner

There are some prototype research scanners that have parallel transmit capabilities. Parallel transmission technology [40]–[42] has been shown to compensate the B_1^+

inhomogeneity by using multidimensional RF transmission, a method that is known as RF shimming [40], [42], [43]. It also enables shortening parallel transmission pulses, through a technique called Transmit SENSE [44], [45] which will be discussed in detail later in Chapter 4. Another application of parallel transmission, more relevant to this thesis, is small FOV excitation, which enables higher spatial resolution and higher temporal resolution.

To implement parallel transmission, manufacturers have designed and built prototype scanners that presently have eight-channel transmit array systems [42], [46], [47]. These are complex and costly systems because each individual channel requires an independent controller and RF power amplifier. However, the key-benefit of parallel transmission technology is the ability of independent RF transmit channels to provide freedom when manipulating the power amplitude and phase of individual channels to overcome B_1^+ inhomogeneity and to make small FOV excitation possible. Hence, in this thesis, we developed an RF coil which is optimized for an eight-channel transmit array systems for transmitting RF pulses and receiving the MR signal.

1.2.3 Small FOV excitation

The small FOV excitation technique, which excites only a small region-of-interest (ROI) inside the whole imaging plane (see Figure 1.4), is commonly referred to as ZOOM imaging. This imaging technique can suppress motion artifacts and limit the excitation FOV in the phase-encoding direction. It was originally proposed more than three decades ago [48], but it is still not widely used because the hardware of typical scanners was limited. It is often limited by a long multidimensional RF excitation pulse

duration (on the order of tens of milliseconds) and therefore has limited clinical applications because of high specific absorption rate (SAR) and slow scans. A solution is the transmit SENSE technique that reduces the RF pulse duration by reducing sampling points in k-space trajectory. This requires a multi-transmit system. Additionally, this technique offers a possibility of small FOV excitation by reducing the RF pulse duration down to a few milliseconds without negatively affecting the spatial resolution of the desired excitation pattern. In this thesis, we propose an RF pulse design method to improve the performance of small FOV excitation using a multi-transmit system. This could lead to improved spatial and temporal resolutions, which are of particular interest in breast and cardiac MRI.

Figure 1.4 Demonstration of a small FOV excitation. Here the logo of the National Research Council of Canada (NRC) was generated in a water phantom using an eight-channel parallel transmit system.

1.2.4 Breast and cardiac parallel transmit array coil

Nowadays the development of transmit array coils for use with parallel transmission technology is mainly focused on head coil designs [49], [50]. To fully explore the potential advantages of parallel transmission technology in clinical usage, more types of transmit array coils should be designed and evaluated. Note that these transmit array

coils are also used to receive the MRI signals. In this thesis, we focus on optimizing an RF coil design for breast and cardiac MRI. The basic coil element in our RF coil design is a loop-array, which is a common design at 3T because of its high efficiency. Other designs of RF coils such as strip-lines [51] and transversal electro-magnetic (TEM) [52] have advantages at ultra-high field strength. However, whether these designs are suitable for 3T MRI is still open for debate.

1.2.5 Patient safety concerns

As motioned above, the specific absorption rate or SAR is the amount of power deposited in a patient during RF transmission. In particular, SAR is a measurement of the energy deposited by electromagnetic (EM) fields per unit mass of tissue and characterizes the heating of the tissue. SAR management is a fundamental safety concern for the clinical implementation of parallel transmission technology. A number of approaches have been proposed to incorporate SAR constraints into parallel transmission pulse design algorithms, including RF pulse power, global SAR, and multi-constraints on global SAR and the ratio of peak-to-average RF power [53]–[59]. These methods can successfully reduce global SAR and local peak SAR. Currently, the best method for local SAR estimation is based on EM simulations. However, any inaccuracies in simulations of EM fields will introduce significant SAR prediction errors and may lead to misinterpretation of tissue heating [60]. In thesis, we showed that the approach taken by most research does not accurately estimate SAR.

1.3 Goals

As mentioned above, the overall goal of this thesis is to achieve higher spatial resolution and higher temporal resolution for breast and cardiac MRI. Our approach is to design an eight-channel array coil that is both transmit and receive, and could be used for both types of studies. The aim is to optimize the coil for small FOV excitation since this leads to a higher spatial resolution in a small ROI. For example, in breast imaging it is important to see the tumor margin; the signal coming from outside of the breasts is not important and may degrade the image quality. Thus, the FOV could be limited to each breast.

There are two main technical tasks that are addressed in this thesis: 1) the design and optimization of a parallel transmission breast and cardiac array coil and 2) the development of a RF pulse design method for optimizing small FOV excitation. Major emphasis is placed on the theory of transmit array coil design, and hardware development. We design a transmit-and-receive array coil that is optimized to small FOV excitation with a clinical pulse sequence in order to provide higher SNR. The consideration of SAR associated with patient safety is necessary and is investigated *in vitro* as part of the basis for *in vivo* studies in the future.

In this work, we propose a way to tackle the aforementioned clinical challenges associated with cardiac and breast imaging. There are three main outcomes that we achieved in this thesis.

Outcome 1: evaluating and understanding the impact of inductive coupling in RF coil simulations

Outcome 2: reducing excitation artifacts through RF pulse and coil design

Outcome 3: evaluating and understanding the impact of inductive coupling in SAR

The thesis is organized as follows. In Chapter 2 we review the essential principles of MRI and the required electric circuit theory for RF coil construction and simulation. Outcome 1 is solely presented in Chapter 3. The first part of the Outcome 2 is presented in Chapter 4. The second part of the Outcome 2 and Outcome 3 are presented in Chapter 5. Chapter 6 gives the summary of the contribution of this work and suggested future work. And finally in Appendix I we include the report on the EM simulation methods presented in the candidacy exam.

In regard to the three main outcomes of this work, Chapter 3 presents the effect of coupling between elements in an array coil and establishes the proper way to incorporate coupling into the EM simulation model. Also, the feasibility of simulating preamplifier decoupling is investigated. Chapter 4 gives a novel RF pulse design method that reduces excitation artifacts. The concept of negative excitation is illustrated and adapted in the workflow of RF design for small FOV excitation. Chapter 5 shows how inductive coupling affects SAR estimation and predict the estimation error due to shortening the RF pulses. In addition, a method to reduce the excitation artifacts by tilting a coil element is proposed to further improve the performance of small FOV excitation.

Finally, the publications associated with each of chapters are as follows. The work based on Chapter 3 was presented at a conference and the abstract published [61]. The work based on Chapter 4 was presented as a poster at a local workshop. The work

based on Chapter 5 was presented at two conferences and the abstracts were published [60], [62]. We have drafted two papers (Chapters 3 and 5) and plan to submit them to journals soon. Papers based on the results of Chapter 4 and the second part of Chapter 5 are in preparation.

Chapter 2: Magnetic resonance imaging-hardware and principles

2.1 Introduction

An MRI scanner (see Figure 2.1) is composed of three main components: a magnet, a gradient system, and an RF system. In this chapter, the essential principles of MRI [63]–[65] are reviewed. In addition, the fundamental theories for RF coil design [66]–[69] are also covered. This chapter is organized form systems perspective, with a discussion of the associated MRI physics following the introduction of each hardware component.

Figure 2.1 Photo showing a Siemens Trio 3T MRI scanner located in the NRC building.

2.2 The magnet

The magnet could be a permanent, a resistive, or a superconducting magnet with a field strength given in units of Tesla (T). Most of the high field (> 1.5 T) scanners are equipped with a superconducting magnet. The function of this magnet is to produce a homogenous static magnetic field (B_0) to polarize nuclear spins in the sample to be imaged. The signal-to-noise ratio (SNR) of the MR image is a function of magnetic field

strength. Hence the trend is to pursue higher magnetic field strengths. Currently, 7T is the highest magnetic strength used in a clinical MR scanner. The drawbacks of these ultra-high fields are related to RF safety issues and high cost. The cost varies a lot and depends on the installation and the ongoing maintenances service. A rule of thumb is about one million dollars per Tesla for a human size MRI scanner.

2.2.1 Nuclear magnetic resonance in a uniform static field

A nucleus having an odd atomic weight and/or odd atomic number, possesses a fundamental property of intrinsic angular momentum (s), which is often called spin [64], [70]. The corresponding magnetic moment of the nucleus (μ), which is related to the angular momentum, is expressed as

$$\vec{\mu} = \gamma \vec{s} \tag{2.1}$$

where γ is the gyromagnetic ratio (see Table 2.1).

The hydrogen atom is the simplest nuclear spin system, having only one proton. The human body is basically made of water (H_2O) and fat. The single proton (^{1}H) is the dominate atom. There are other atoms, e.g. carbon (^{13}C), phosphorus (^{31}P), and sodium (^{23}Na), found in the human body, but their concentration is very small. The value of gyromagnetic ratio is different for each atom.

Table 2.1 Gyromagnetic ratio vales for different nucleus found in human body.

Nucleus	γ/2π (in unit of MHz/T)
^{1}H	42.58
^{13}C	10.71
^{31}P	17.25
^{23}Na	11.27

In a classical model, the interaction between the external magnetic field B_0 and a magnetic moment μ is shown in Figure 2.2. The spin has its own rotation axis (Figure 2.2 A), which in general can be at angle of θ with respect to B_0. When B_0 exists the spin and hence the magnetic moment experiences a torque (see Figure 2.2 B), which forces the magnetic moment to precess around the axis of B_0, remaining at fixed angle of θ. The equaiton of motion for the magnetic moment experiences the torque is given by

$$\frac{d\vec{\mu}}{dt} = \vec{\mu} \times B_0 \hat{z} \tag{2.2}$$

Here we assume B_0 aligns with the z-axis. The magnitude of the differential change in magnetic moment is expressed as

$$\left|d\vec{\mu}\right| = \gamma \left|\vec{\mu} \times B_0 \hat{z}\right| dt = \gamma \mu B_0 \sin\theta dt \tag{2.3}$$

Note that Figure 2.2 B indicates the differential change in magnetic moment can also be express as

$$\left|d\vec{\mu}\right| = \mu \sin\theta \left|d\varphi\right| \tag{2.4}$$

Comparing and rearranging Equations 2.3 and 2.4 result in the famous Larmor equation

$$\omega_0 = \left|\frac{d\varphi}{dt}\right| = \gamma B_0 \tag{2.5}$$

Here the angular frequency ω_0 is known as Larmor frequency and is proportional to the field strength of the external magnetic field, and the gyromagnetic ratio.

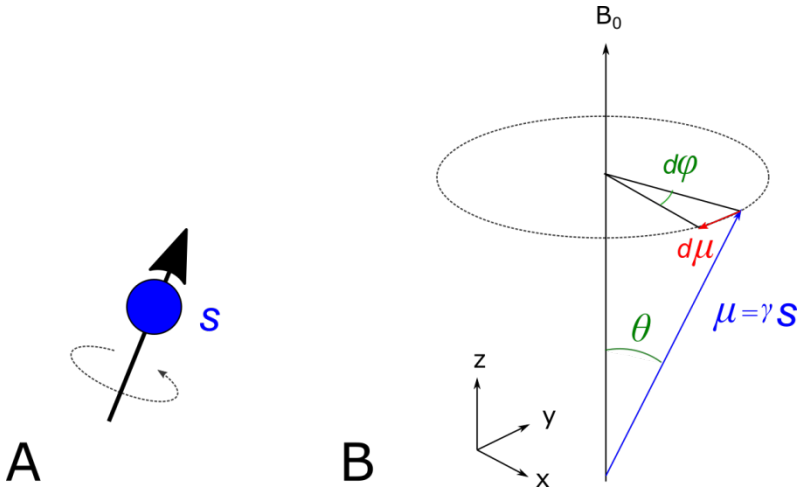

Figure 2.2 Diagrams illustrating (A) nucleus with intrinsic spin angular momentum. (B) The classical precession model. The angle between magnetic moment and external magnetic field is θ, and can range from 0 to π.

In a quantum mechanics model, a magnetic moment has a discretized value of θ. A proton is referred as a spin-1/2 system, and the magnitude of the magnetic moment of a proton is given by

$$\left|\vec{\mu}\right| = \gamma \frac{h}{2\pi}\sqrt{I(I+1)} \tag{2.6}$$

where h is the Planck's constant and I is the nuclear spin quantum number (I = 1/2 in this example). Recall that the external magnetic field aligns with the z-axis. Therefore, only the z-component of magnetic moment can be measured and is expressed as

$$\left|\vec{\mu_z}\right| = \gamma m_I \frac{h}{2\pi} \tag{2.7}$$

where m_I is the magnetic quantum number and $m_I = \pm 1/2$. For this spin-1/2 system, there are (2I+1) values of m_I. Hence, the z-component of the magnetic moment can only take on two possible values, *parallel* ($m_I = +1/2$) corresponding to the lower energy level and *anti-parallel* ($m_I = -1/2$) corresponding to the higher energy level.

The phenomenon of splitting energy levels is known as the Zeeman effect. The energy levels of this spin-1/2 system are defined as

$$E = -\gamma m_I \frac{h}{2\pi} B_0 \tag{2.8}$$

The energy difference between these two energy levels is given by

$$\Delta E = \gamma \frac{h}{2\pi} B_0 = \frac{h}{2\pi} \omega_0 \tag{2.9}$$

Hence, to excite the magnetic moment by an EM field from the lower energy level to the higher energy level, the required energy equals to this energy difference and this EM field is oscillating with Larmor frequency.

2.2.2 Bulk magnetization

From a macroscopic point of view, magnetization (M) is an ensemble of individual spins and their associated magnetic moments. In the absence of the external magnetic field (Figure 2.3 A), magnetic moments are randomly orientated and result in a zero net magnetic moment. When an external field exists, all the magnetic moments would point in either in either parallel or anti parallel direction (Figure 2.3 B). This leads to a non-zero net magnetic moment called the net magnetization (M_0) as shown in Figure 2.3 C.

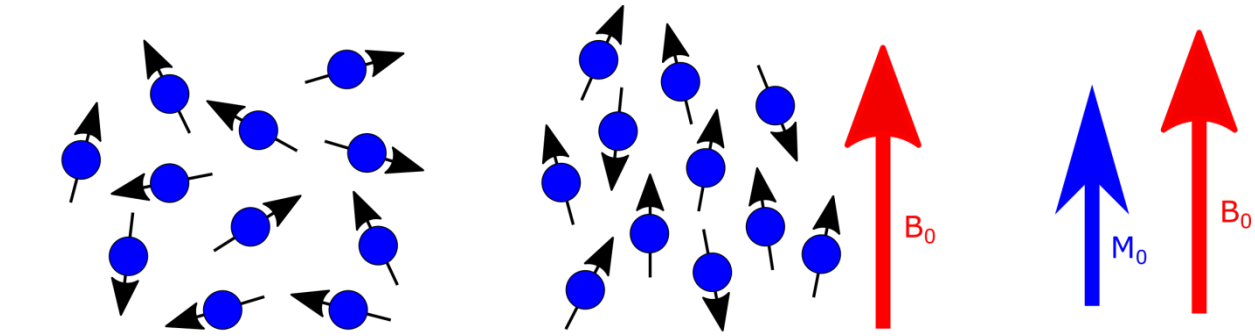

Figure 2.3 Diagrams illustrating nuclear spin orientation (A) without and (B) with the presence of an external magnetic field (B_0). (C) The ensemble of magnetic moments is expressed as the magnetization M_0.

For the spin-1/2 system described in previous section, Figure 2.3 illustrates the system reaches thermal equilibrium. The ratio of the number of magnetic moments at two energy levels is described by Boltzmann distribution and its approximation becomes

$$\frac{n_{parallel}}{n_{anti\text{-}parallel}} = e^{\gamma\frac{h}{2\pi}B_0 / k_B T} \approx 1 + \frac{\gamma\frac{h}{2\pi}B_0}{kT} \tag{2.10}$$

where n is the number of parallel and anti-parallel magnetic moments, h is the Planck's constant, B_0 is the magnetic field strength, T is the temperature in Kelvin (K), and Boltzmann constant, k, is $1.38\text{x}10^{-23}$ J/K. From Equation 2.10 the population difference for the two energy levels is given by

$$(n_{parallel} - n_{anti\text{-}parallel}) \approx \frac{n_{total}}{2}\frac{\gamma\frac{h}{2\pi}B_0}{kT} \tag{2.11}$$

where n_{total} is the totoal number of magnetic moment. The net magentization in thermal equibilum is expressed as

$$M_0 = \frac{\gamma^2(\frac{h}{2\pi})^2 B_0 n_{total}}{4kT} \tag{2.12}$$

The magnitiude of the net magnetization is propotional to temperture and external magentic field strength. As an example, when the room temperture is 300 K and external magnetic field strengs is to 1 T, only three out of a million protons will generate NMR signal. This suggests that MRI is a low-sensitivity technique and the current trend on a MRI scanner is using higher magnetic field strentgh.

2.2.3 Bloch equation

The evolution of the magnetization over time is described by the Bloch equation and is expressed as

$$\frac{d\vec{M}}{dt} = \vec{M} \times \gamma \vec{B}(t) - \frac{M_x \vec{i} + M_y \vec{j}}{T_2} - \frac{(M_z - M_z^0)\vec{k}}{T_1} \tag{2.13}$$

where the first term $\vec{M} \times \gamma \vec{B}$ is the torque on the magnetization due to the net magnetic field, and which is usually sufficient to describe the behavior of the magnetization during RF pulse excitation. The other terms describe the relaxation process of magnetization after the RF excitation. T_1 and T_2 are constants of spin-lattice relaxation and spin-spin relaxation. M_z^0 is the thermal equilibrium value of magnetization before the RF excitation. The z-component of the net magnetization (M_z) is the longitudinal magnetization. The x- and y-components of the magnetization are M_x and M_y, respectively, and the net magnetization in the x-y plane is known as the transverse magnetization $M_{xy} = \sqrt{M_x^2 + M_y^2}$.

2.3 The gradient system

A gradient system consists of three gradient coils and is used to generate magnetic fields that vary along the X, Y, and Z directions. These magnetic fields vary linearly and

the strength of each gradient (G) along the assigned direction is typically given in units of mT/m and expressed as

$$G_i = \frac{dB_z}{di} \text{ and } i = x, y, z \tag{2.14}$$

The function of the gradient is to encode spatial-frequency information. The performance of the gradient system is limited to the maximum gradient strength and slew rate, which is the maximum gradient strength divided by the rise time. Most high-field scanners have maximum gradient strengths and slew rates in range of 30 to 40 mT/m and 100 to 200 mT/m/s, respectively. A higher gradient strength and higher slew rate give better performance.

2.3.1 Selective excitation

When a sample is placed in the main magnet, with np applied gradients all spins inside the sample precess at the same Larmor frequency $\omega_0 = \gamma B_0$. Hence they are not distinguishable. A slice selection gradient generates a linear magnetic field that varies along an axis that is perpendicular to the imaging plan. When a RF pulse is applied simultaneously with the gradient, the bandwidth of the RF pulse matches to the range of frequencies in the selected slice. Using the combination of RF pulses and a slice selection gradient, the frequency of the spins is given by

$$f = \frac{\gamma}{2\pi}(B_0 + zG_z) \tag{2.15}$$

This equation is a function of position. Here we assume the slice selection gradient is along the z-axis (G_z). By taking the derivative of this equation, the relation between the slice thickness (Δz) and bandwidth (Δf) of the RF pulse is expressed as

$$\Delta z = \frac{2\pi}{\gamma}\frac{\Delta f}{G_z} \tag{2.16}$$

Hence, to choose a specific slice of the sample, we can apply the slice selective gradient. The spins whose frequency matches the RF bandwidth will be excited. In addition, the slice thickness is controlled by the gradient strength as shown in Figure 2.4.

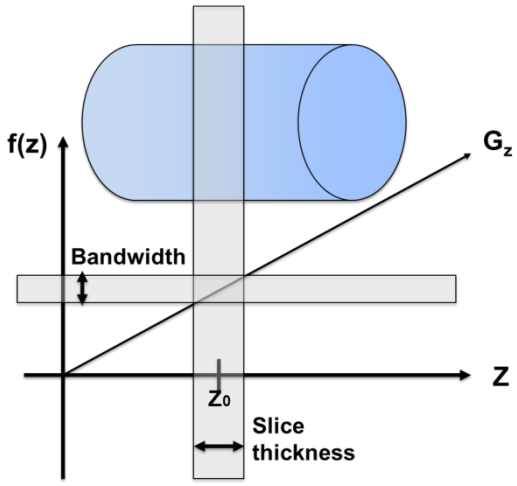

Figure 2.4 Graph showing the function of the RF pulse slice selection gradient. The frequency f is a function of position. Bandwidth of the RF pulse and slice selection gradient determine the thickness of theslice.

2.3.2 MR image encoding

The role of gradients in a MRI pulse sequence is shown in Figure 2.5. Here we use a spin-echo sequence as an example to explain how an MR signal is generated and how an image is encoded. The spin-echo sequence makes use of two RF pulses, the first pulse is applied with the slice-selection gradient. After the imaging slice is selected, the spins in this slice are excited. The external inhomogeneities in the magnetic field cause the spins to dephase and the net magnetization in the transverse plane decreases. The second pulse is applied to rephase the spins in the transverse plane and a signal (known as spin echo) is generated. However, in this slice the MR signal is

indistinguishable without spatial information. To separate the signal in each voxel of the image, frequency and phase gradients are applied to give each voxel a unique resonance frequency and phase shift. This procedure is called image encoding or spatial localization. For a given amplitude of phase-encoding gradient, the resonance frequency is altered as a function of position along the axis of the frequency-encoding gradient. The first row of the image is encoded and then the second row is acquired using different amplitude of phase-encoding gradient. This step repeats until the whole image is encoded. Note that the signal is encoded in frequency domain. The MR image reconstruction can be done by taking the Fourier transform.

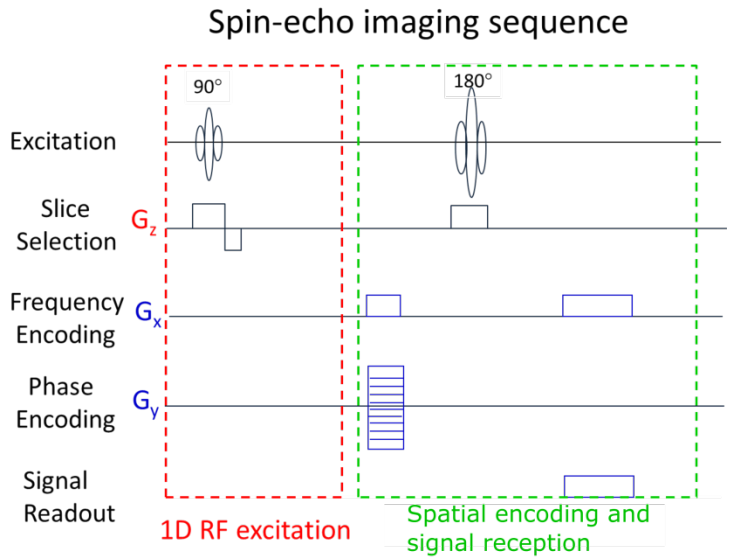

Figure 2.5 Time diagram of a spin echo pulse sequence. In the first part (rea dashed box), a slice of imaged object is selected by applied a 90^o RF pulse while the slice selected gradient is turned on. The transvers magnetization is them generated. Due to the field inhomogeneity, the spins start to dephase. The 180^o RF pulse is applied to rephase the spins and form the MR signal. The frequency and phase encoding gradients are applied to add spatial information to the signal.

2.4 The RF system

An RF system includes a transmit coil and a receive coil. Most MR scanners are equipped with a built-in whole body transmit coil, which usually is a birdcage coil. As mentioned above, the function of the transmit coil is to generate a magnetic field (B_1^+) for spin excitation. A receive coil is used to detect the MR signal from precession of magnetization and convert it to a voltage signal, which is described as Faraday's law of induction.

$$\text{emf}(t) = \frac{\partial \phi}{\partial t} = -\frac{\partial}{\partial t}\iiint_v B_1^-(\vec{r}) \cdot M(\vec{r}, t) dv \tag{2.17}$$

where emf is the electromotive force, Φ is the magnetic flux, B_1^- is the magnetic field of the receive coil per unit current and is also known as the sensitivity profile, r is the position vector for the receive magnetic field, and time-varying magnetization, M. The SNR of the image depends on hardware. The expression of SNR is given by

$$\frac{S}{N} = \frac{-\frac{\partial}{\partial t}\iiint_v B_1^-(\vec{r}) \cdot M(\vec{r}, t) dv}{\sqrt{4\,k\,T\,R\,2BW}} \tag{2.18}$$

The signal part is described in Equation 2.17. The major source of noise is thermal noise in the sample. From the fluctuation theorem, standard deviation of the fluctuation noise voltage is the denominator of the Equation 2.18. Here k is Boltzmann's constant, T is the temperature, R is the effective resistance of the coil loaded by the imaged sample, and BW is the bandwidth of the receive coil. Ideally, the transmit coil should generate a uniform field and a receive coil should have high sensitivity, which leads to high SNR in images.

2.4.1 RF coil construction

The functions of a RF coil are to transmit RF pulses (transmit coil) or to receive signal (receive coil). A RF coil can be used for both functions. Depending on applications (i.e. breast or cardiac imaging), a receive RF coil is customized to achieve high SNR in the region of interest which is beneficial for high resolution imaging. In contrast, a transmit RF coil aims to generate a homogenous B_1^+ field and to obey the SAR regulations for patient safety. Hence the theory of RF coil design covers knowledge of MR physics and electrical engineering. In the following sections, we summarize the fundamental principles which are required for RF coil construction.

2.4.1.1Properties of a single-element RF coil

In general, a surface loop is a basic element of a RF coil. This is composed of lumped elements: resistor (R), inductor (L) and capacitor (C) and hence the surface loop is represented by a RLC circuit. The behavior of this RLC circuit (surface loop) is determined by the total effect of these lumped elements. It is characterized by the complex impedance (Z) which is the ratio of complex voltage (V) and complex current (I) in the circuit and is given by

$$Z = \frac{V}{I} = |Z| e^{j\phi} \tag{2.19}$$

where j is the imaginary unit (square root of -1). |*Z*| is amplitude of the ratio of voltage and current, and Φ is the phase difference between the voltage and the current. The phase difference exists when there are reactive elements in the circuit such as an inductor or a capacitor. The voltage and current will be in phase then the circuit is purely resistive.

When we calculate the impedance of the circuit, it is commonly expressed as a Cartesian form of a complex number:

$$Z = R + jX \tag{2.20}$$

where the real part, R, of the total impedance is the resistance of the circuit. The imaginary part, X, of the total impedance is the reactance of the circuit. The reactance is a summation of an inductive components X_L and a capacitive component X_C, which are expressed as

$$\begin{aligned} X_L &= \omega L \\ X_c &= -\frac{1}{\omega C} \end{aligned} \tag{2.21}$$

where L is inductance with a unit of Henry (H) and C is capacitance with a unit of Farad (F). ω is the angular frequency of the lumped elements. A surface loop can be designed as a series RLC circuit where all lumped elements are in series or a parallel RLC circuit where a resistor is in series with an inductor but in parallel with a capacitor (see Figure 2.6). The impedances of the two circuits are given by

$$\begin{aligned} Z_{series} &= R + j(\omega L - \frac{1}{\omega C}) \\ Z_{parallel} &= \frac{1}{\frac{1}{R + j\omega L} + j\omega C} \end{aligned} \tag{2.22}$$

Hence we can see the frequency response of the impedance for the two circuits is different.

This resonance frequency of the circuit is expressed as

$$\omega = \frac{1}{\sqrt{LC}} \tag{2.23}$$

In the series circuit the resistor dominates at resonance, but in a parallel circuit the analysis is more complicated. For either design, when the loop is tuned and matched, the imaginary part of the impedance is zero looking into the circuit and the real part is made to equal 50 ohms at resonance frequency (123.2 MHz at 3T) to maximize the power transfer to the loop from the 50 ohms output of the preamplifier connected via a 50 ohms cable.

When we build a RF coil, the total inductance of the coil is determined by its geometry and is thus a fixed quantity. By adjusting the required capacitors on the loop, the resonance frequency of the circuit can be made to match the Larmor frequency.

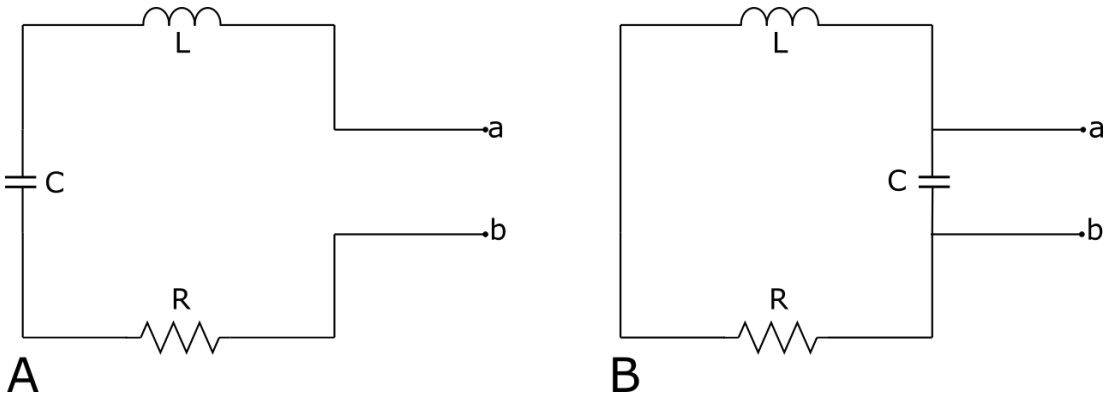

Figure 2.6 Schematic showing (A) series and (B) parallel RLC circuits

2.4.2 RF coil safety

The safety aspects of RF coils need to be well investigated. SAR describes the potential tissue temperature increase caused by RF power absorption in the body. The US Food and Drug Administration (FDA) and the International Electrotechnical Commission (IEC) have published limitations and guidelines for maximum local SAR in

1g and 10g volumes and global SAR averaged over the body or the head to ensure patient safety [71], [72]. The general form of SAR is expressed as:

$$SAR(\vec{r}) = \frac{1}{V}\int_{sample}\frac{P(\vec{r})}{m}dV = \frac{1}{V}\int_{sample}\frac{\sigma(\vec{r})}{2\rho(\vec{r})}\left|E(\vec{r})\right|^2 dV \quad (2.24)$$

where r is the position vector for the receive magnetic field, P is the RF power absorption in the sample. E is the electric-field, σ and ρ are the conductivity and the density of the tissue and the unit of SAR is *W/kg*. For example, the global SAR limit for whole body is 4 *W/kg* (15 minutes exposure averaged) [73]. However, the E-field within a human subject is very difficult to measure experimentally. Numerical methods provide an alternative way to acquire E-fields within different tissues and at different magnetic field strengths of MRI scanners.

2.4.3 RF coil simulation

Using numerical methods is essential to simulate EM fields within an MRI RF coil when evaluating the coil performance relating to the interactions with human tissues (Figure 2.7) [69]. At the initial stage of the design process, various models of RF coil can be simulated without constructing each design. Then, only a few RF coil designs are required to be built for the final optimization. Therefore, using numerical methods for RF coils allows us to significantly speed up the design process [69], [74].

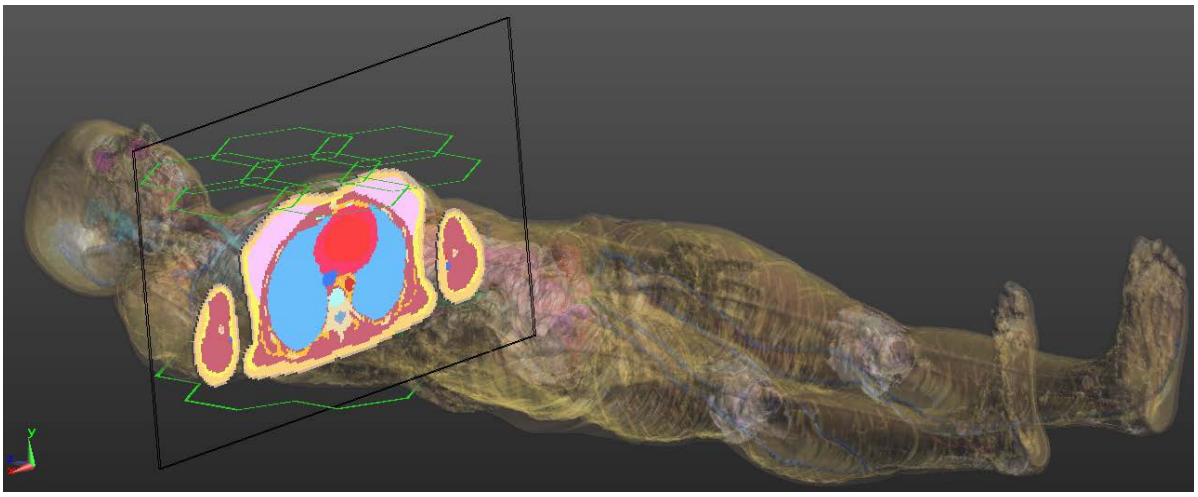

Figure 2.7 Screenshot showing an eight-channel RF coil, which is composed of seven green hexagonal elements in the anterior section and one polygonal element for the posterior section. The coil is loaded with a human tissue model. The cross-section is a selected slice showing the organs such as a heart and breasts inside the human model.

2.4.3.1Finite-difference time domain (FDTD) simulation

All EM simulation software uses Maxwell's equations to calculate magnetic and electric fields in the time or frequency domain. In this section, of particular interest are the two Maxwell's curl equations (Equations 2.25-26). These are the updated functions for the FDTD software that we used for this study. The detail of the fundamental EM theory are discussed further in Appendix I.

$$\nabla \times E = -\frac{\partial B}{\partial t} \quad \text{(Faraday's law-induction)} \tag{2.25}$$

$$\nabla \times H = -\frac{\partial D}{\partial t} + J_{\sigma} + J_{imp} \quad \text{(Maxwell-Ampere law)} \tag{2.26}$$

where

E: electrical field intensity (Volts/meter)

H: magnetic field intensity (Amperes/meter)

B: magnetic flux density (Webers/meter^2)

D: electric flux density or electric displacement field (Coulombs/ meter^2)

J_σ: electric current density at a given material with conductivity σ (Amperes/meter^2)

J_{imp}: impressed current density which can be the current source used to excite a RF coil (Amperes/meter^2)

The FDTD method is a time-domain solver for Maxwell's equations.The FDTD method was first introduced by K. S. Yee in 1966 [75] and is probably the most popular time-domain solver for EM problems. Moreover, FDTD is recommended by the IEC for RF coil design and MRI SAR measurements in human tissue models [69]. The main reason for the success of the FDTD method is because the programming implementation is relatively simple even for three-dimensional problems. Use of FDTD studies is expanding and advanced techniques such as alternating-direction-implicit (ADI) based FDTD are being developed [76]. In the following discussion, only the conventional explicit FDTD technique is described because it is the basic method used for this study.

The FDTD method simulates the behavior of wave propagation in space and time domains. The algorithm by Yee discretizes the differential form of the time-dependant Maxwell's equations and creates a gridded computational domain with a large number of cuboids [77]–[81]. The total time of the wave propagating through the grid is discretized into small time steps (Δt). The transient EM fields are recorded at each time step until the fields reach the steady state. The basic cell of Yee's algorithm is illustrated in Figure 2.8. It shows the E-field components always pointing along the edges of the cell and the H-field components always perpendicular to and centered on each face.

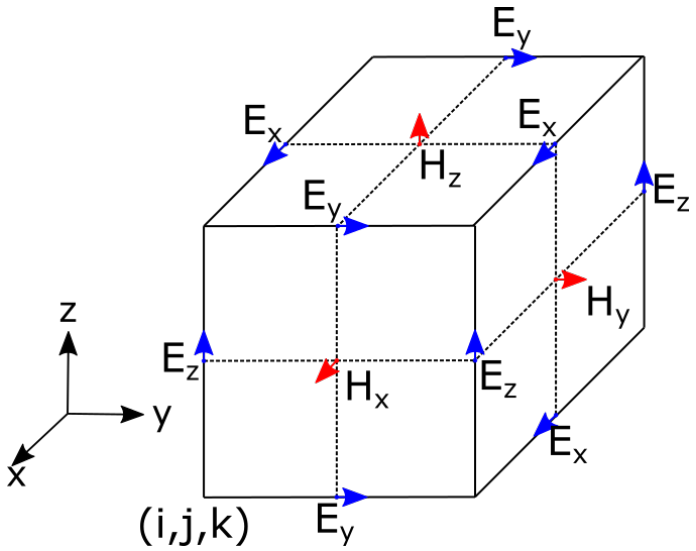

Figure 2.8 Yee's cell in a FDTD grid showing the position of the E- and H-fields components.

For each cell the H- and E-field components must be solved at each time step. The FDTD method is a direct solution of the time-dependent Maxwell's curl equations. It applies central difference approximations to the temporal and spatial derivatives that are contained in Equations 2.25-26 and can be expressed as

$$\frac{\partial f(i,j,k,n)}{\partial x} = \frac{f^n\left(i+\frac{\Delta x}{2},j,k\right) - f^n\left(i-\frac{\Delta x}{2},j,k\right)}{\Delta x} + O[(\Delta x)^2] \tag{2.27}$$

$$\frac{\partial f(i,j,k,n)}{\partial t} = \frac{f^{n+1/2}(i,j,k) - f^{n-1/2}(i,j,k)}{\Delta t} + O[(\Delta t)^2] \tag{2.28}$$

where f is a function of space and time. Here f could be the either the H- or E-field with temporal or spatial offsets. The variables i, j, and k are the indices of the rectangular coordinates of a Yee's cell at the n*th* time step ($x = i\Delta x$, $y = j\Delta y$, $z = k\Delta z$, and $t = n\Delta t$). The terms $O[(\Delta x)^2]$ and $O[(\Delta t)^2]$ are second-order error terms of the central difference approximation. When setting up the grid in a computational domain, the size of each cell should be much smaller than the wavelength in free space or the size of any object. In general, the recommended maximum cell size is 1/20 of the wavelength in free space

[69]. In practice, the cell size is about 1/200 of the wavelength. Applying Equations 2. 27-28 to Maxwell's curl equations, the six equations governing all E- and H-field components can be written as follows:

$$E_x^{n+1}\left(i+\tfrac{1}{2},j,k\right)=\frac{1}{\beta(i+\frac{1}{2},j,k)}\times\left\{\begin{array}{l}\alpha\left(i+\frac{1}{2},j,k\right)E_x^{n}\left(i+\frac{1}{2},j,k\right)\\+\dfrac{1}{\Delta y}\left[H_z^{n+\frac{1}{2}}\left(i+\frac{1}{2},j+\frac{1}{2},k\right)-H_z^{n+\frac{1}{2}}\left(i+\frac{1}{2},j-\frac{1}{2},k\right)\right]\\-\dfrac{1}{\Delta z}\left[H_y^{n+\frac{1}{2}}\left(i+\frac{1}{2},j,k+\frac{1}{2}\right)-H_y^{n+\frac{1}{2}}\left(i+\frac{1}{2},j,k-\frac{1}{2}\right)\right]-J_{imp,x}^{n+\frac{1}{2}}\left(i+\frac{1}{2},j,k\right)\end{array}\right\}$$

(2.29)

$$E_y^{n+1}\left(i,j+\tfrac{1}{2},k\right)=\frac{1}{\beta(i,j+\frac{1}{2},k)}\times\left\{\begin{array}{l}\alpha\left(i,j+\frac{1}{2},k\right)E_y^{n}\left(i,j+\frac{1}{2},k\right)\\+\dfrac{1}{\Delta z}\left[H_x^{n+\frac{1}{2}}\left(i,j+\frac{1}{2},k+\frac{1}{2}\right)-H_x^{n+\frac{1}{2}}\left(i,j+\frac{1}{2},k-\frac{1}{2}\right)\right]\\-\dfrac{1}{\Delta x}\left[H_z^{n+\frac{1}{2}}\left(i+\frac{1}{2},j+\frac{1}{2},k\right)-H_z^{n+\frac{1}{2}}\left(i-\frac{1}{2},j+\frac{1}{2},k\right)\right]-J_{imp,y}^{n+\frac{1}{2}}\left(i,j+\frac{1}{2},k\right)\end{array}\right\}$$

(2.30)

$$E_z^{n+1}\left(i,j,k+\tfrac{1}{2}\right)=\frac{1}{\beta(i,j,k+\frac{1}{2})}\times\left\{\begin{array}{l}\alpha\left(i,j,k+\frac{1}{2}\right)E_z^{n}\left(i,j,k+\frac{1}{2}\right)\\+\dfrac{1}{\Delta x}\left[H_y^{n+\frac{1}{2}}\left(i+\frac{1}{2},j,k+\frac{1}{2}\right)-H_y^{n+\frac{1}{2}}\left(i-\frac{1}{2},j,k+\frac{1}{2}\right)\right]\\-\dfrac{1}{\Delta y}\left[H_x^{n+\frac{1}{2}}\left(i,j+\frac{1}{2},k+\frac{1}{2}\right)-H_x^{n+\frac{1}{2}}\left(i,j-\frac{1}{2},k+\frac{1}{2}\right)\right]-J_{imp,z}^{n+\frac{1}{2}}\left(i,j,k+\frac{1}{2}\right)\end{array}\right\}$$

$$\begin{aligned}H_x^{n+\frac{1}{2}}\left(i,j+\tfrac{1}{2},k+\tfrac{1}{2}\right)=H_x^{n-\frac{1}{2}}\left(i,j+\tfrac{1}{2},k+\tfrac{1}{2}\right)&-\frac{\Delta t}{\mu\Delta y}\left[E_z^{n}\left(i,j+1,k+\tfrac{1}{2}\right)-E_z^{n}\left(i,j,k+\tfrac{1}{2}\right)\right]\\&+\frac{\Delta t}{\mu\Delta z}\left[E_y^{n}\left(i,j+\tfrac{1}{2},k+1\right)-E_y^{n}\left(i,j+\tfrac{1}{2},k\right)\right]\end{aligned}$$

(2.31)

$$H_y^{n+\frac{1}{2}}\left(i+\tfrac{1}{2},j,k+\tfrac{1}{2}\right)=H_y^{n-\frac{1}{2}}\left(i+\tfrac{1}{2},j,k+\tfrac{1}{2}\right)-\frac{\Delta t}{\mu\Delta z}\left[E_x^n\left(i+\tfrac{1}{2},j,k+1\right)-E_x^n\left(i+\tfrac{1}{2},j,k\right)\right] \quad (2.32)$$
$$+\frac{\Delta t}{\mu\Delta x}\left[E_z^n\left(i+1,j,k+\tfrac{1}{2}\right)-E_z^n\left(i,j,k+\tfrac{1}{2}\right)\right]$$

$$H_z^{n+\frac{1}{2}}\left(i+\tfrac{1}{2},j+\tfrac{1}{2},k\right)=H_y^{n-\frac{1}{2}}\left(i+\tfrac{1}{2},j+\tfrac{1}{2},k\right)-\frac{\Delta t}{\mu\Delta x}\left[E_y^n\left(i+1,j+\tfrac{1}{2},k\right)-E_y^n\left(i,j+\tfrac{1}{2},k\right)\right] \quad (2.33)$$
$$+\frac{\Delta t}{\mu\Delta y}\left[E_x^n\left(i+\tfrac{1}{2},j+1,k\right)-E_x^n\left(i+\tfrac{1}{2},j,k\right)\right]$$

where $\alpha = \varepsilon/\Delta t - \sigma/2$ and $\beta = \varepsilon/\Delta t + \sigma/2$ and. The permittivity and permeability of the medium are given by ε and σ respectively. These are the field equations that are updated in time and space.

A simulation is started by assuming the initial fields are zeros and n starts from one. The E-field at $t = n\Delta t$ is used to calculate the H-field at later time $t = (1+1/2)\Delta t$ and this H-field is applied to update the E field at the next time step. The idea is to keep updating the E- and H-fields alternately at each time step, until the fields propagate all through the grid and reach a steady state. This process is called a leap-frog scheme.

A typical FDTD model includes an excitation source which can be a Gaussian pulse, sinusoidal wave or arbitrarily defined by the user. This source generates a wave that propagates through a discretized grid of the object and free space. The field quantities are then recorded at each time step until the whole system reaches a steady state. If frequency-dependent characteristics are of interest, e.g. scattering-parameters, a Fourier transform can be applied to extract the quantities of interest. A major advantage of FDTD is its flexibility. It is capable of modeling time-dependent and broadband EM problems with various types of materials including conductors, dielectrics and lossy media in one simulation. Therefore the FDTD method is the best choice for modeling

RF coils that are loaded with inhomogeneous human tissue models [69]. Another advantage of FDTD is that it is easy to implement with parallel computing techniques [83]. A number of commercial, e.g. SEMCAD X (ZMT, Switzerland) and XFDTD (Remcom, USA), and non-commercial software tools have been developed and applied to all classes of EM problems. We used FDTD method in this work.

While the FDTD method is a very efficient solver, there are some situations in which it is not an ideal choice. These include: 1) an unbounded space that will lead to a large computational domain; 2) a high-Q resonance that suffers from a long wave propagation time before reaching steady state; 3) a complex object with intricate features because the time step is governed by the grid size; and, 4) a curved object where staircase errors occur on the surface since the basic FDTD cell is rectangular [84]. In this work, we use FDTD method to simulate RF coil arrays loaded with a small water bottle or a human model. Hence, the situations mentioned above are not a problem. Although FDTD has its limitations, there is a trend among FDTD researchers to explore the more advanced ADI-FDTD time-marching scheme. If the ADI-FDTD technique can successfully be combined with parallel computation, the application of the FDTD method will likely be expanded [84].

Chapter 3: Evaluating the impact of inductive coupling in RF array simulations

Most modern coils contain multiple elements. To design a transmit-and-receive array coil for parallel transmission, it is important to investigate how inductive coupling between array elements will affect the overall performance of the coil. Inductive coupling has historically been neglected in RF coil simulations. However, in reality it always exists to some degree. In this chapter, we focus on establishing a proper way to incorporate the coupling into the electromagnetic (EM) simulation model. We also investigate the feasibility of simulating preamplifier decoupling.

We are interested in understanding how the array is affected by inductive coupling when it is in transmit mode (induced currents in other elements change total B_1 field) as well as receive mode (noise correlation is different if coupling is included). For example, one can imagine simulating a single Tx coil element that is either in isolation or that is part of an array an coupled to other elements. If the outcome of the simulations are different, then one knows that the B_1^+ field maps (in Tx mode) are affected by coupling, of course, but also by reciprocity that the noise correlation (in Rx mode) is affected too. How to include inductive coupling in the simulation is therefore essential.

The procedures of EM simulation for a transmit coil and a receive coil are essentially the same; the only difference is how we use the simulated EM fields to evaluate the performance of the designed coil. Due to the principle of reciprocity [84], one can use the findings from a transmit coil simulation to determine the behavior of a receive coil. In our simulations, there are two types of models: 1) drive one loop with no other loops present and 2) drive one loop with a neighbouring loop present and varying

amounts and sources of coupling. The first method is used by everyone else and ignore inductive coupling. The second method is the focus in this thesis.

3.1 Introduction

In magnetic resonance imaging, the quality of images depends on coil geometry and thus in clinical practice different body parts require different coils. Consequently, it is necessary to construct a coil for each clinical application and this requires analyzing many potential coil designs. For comparing coil designs, instead of building all possible configurations, simulations are used for convenience and to speed up the design process.

When building a receive coil, for example, the signal-to-noise ratio (SNR) needs to be optimized. In general, the signal depends on the B_1^- field and the noise depends on the E-field. Using simulations, the B- and E-field distributions of each design can be predicted and optimized before a coil is built. Additionally, E-field distributions are very difficult to acquire experimentally and simulations more easily provide this information. However, simulations make assumptions that depend on details of the simulation method. Thus, it is important to verify the simulations with corresponding measurements.

In this chapter, we focus on Rx coil measurements rather than Tx. The reason for this is that one can more easily measure the noise correlation coefficient from images in Rx mode than it is to experimentally measure B_1^+ maps in Tx mode. According to reciprocity theorem, however, if the simulation in Rx mode is validated, then one can trust that the same simulation methods for the Tx mode can also be trusted. A two-channel array coil is the most basic configuration and will be used here for comparison

between simulation and experiment. We remind the reader that as stated above Rx simulations are actually done by driving one the coils (i.e. Tx mode) and making use of reciprocity. This will be discussed in greater detail in Section 3.1.2.

3.1.1 The noise in MR Images

The sources of noise in MR images are mainly from the RF coil and sample being imaged. The noise (or loss) of the coil is represented by an effective resistance (R_{eff}). There are four major types of noise sources: 1) coil conductivity loss, 2) coil radiation loss, 3) sample dielectric loss, and 4) sample inductive loss (R_{sample} is proportional to ω^2). At very high frequencies, most current flows on the surface of the coil and this phenomenon is described as the skin depth effect and results in coil conductivity loss due to higher resistance at higher frequencies. The coil radiation loss is typically negligible because the operation frequency is relatively low. In the following simulations, it is assumed that the sample dielectric and inductive losses are the only sources of noise.

An important design criterion of an RF coil is to achieve a high SNR. Both signal and noise in MR images are related to fundamental properties of the sample and the conductors in the coil. The phenomenon of charges randomly moving inside a conductive sample is described by Brownian motion. These free charges generate a random current flow in the sample and become a source of noise. If a receive loop is placed near the sample, an induced noise voltage due to the Brownian motion of charge in the sample will be detected.

The noise voltage induced in a single loop of an RF coil is also known as thermal noise or Johnson-Nyquist noise. Its variance is expressed as

$$\left\langle V(t)^2 \right\rangle = 4k\,T\,\Delta f\,R_{eff} \tag{3.1}$$

where the brackets indictate the time average of the random variable, k is Boltzmann's constant, T is the absolute temperature, Δf is the bandwidth of the receive coil, and R_{eff} is the effective resistance of the RF coil when loaded with a sample. Here the resistance of the conductors of the RF coil is negligible. Therefore, R_{eff} represents the resistance of the sample only. The fluctuating noise is a random variable, i.e., white noise, and with a zero mean. The thermal noise will generate an induced voltage in a loop of an RF coil. This induced voltage is amplified by a preamplifier. The signal received by an MR scanner is proportional to this voltage. Hence, the noise covariance, $\langle V_i V_j \rangle$, of the voltages between any two coil elements i and j in a multi-loop array coil is a function of the shared resistance R_{ij}. The knowledge of the noise variance is applied for sum-of-square image reconstruction which is the standard reconstruction method used for routine clinical imaging. To obtain the optimum SNR of images, the noise covariance matrix is used to account for different noise levels between each coil elements [85], [86].

3.1.2 Reciprocity theorem

In simulation, it is easy to drive a coil with a voltage source, but it is difficult to mimic Johnson noise in the sample. In contrast, in experimental measurement, it is easy to measure noise correlation from images, but it is difficult to measure EM field directly. Because of reciprocity, EM fields in Tx mode equate to sensitivity maps in Rx mode. Hence, Tx mode simulation can be compared with Rx coil measurements.

The noise source from the sample can be modeled by an ideal current source that is in parallel with a resistor representing the sample. This noise current source can be converted to a noise voltage source by Thevenin's theorem where the resistor is in series with the voltage source. To explain the fundamental difference between simulation and experiment, we make use of the reciprocity theorem in a two-port network as shown in Figure 3.1. This theorem states that if the positions of a voltage source and an ammeter are swapped, the reading of the ammeter remains unchanged. The measurement corresponds to the top pair in Figure 3.1 and the simulation corresponds to the bottom pair. In this example, the right-hand side of each two-port network is the output of the network and the left-hand side is the input.

In the measurement case, the top-left network represents a voltage induced in a receive coil by a current source in the sample. This is how a receive coil detects the signal from the sample. The top-right shows that when the same coil is used as a transmit coil, it is driven by a current source and will induce a voltage in the sample. Simulations are performed using the bottom-right case. Here the coil is driven by a voltage source that will induce a current in the sample. This is how the coil is modeled to represent a transmit coil. Then the EM fields of the receive coil are easily obtained by applying the reciprocity theorem to give the bottom-left network. Notice that the receive coil is modeled with different networks in the simulations and measurements. But the voltage source in the simulation can be converted to a current source by applying Norton's theorem. Then the simulation can represent the measurement case.

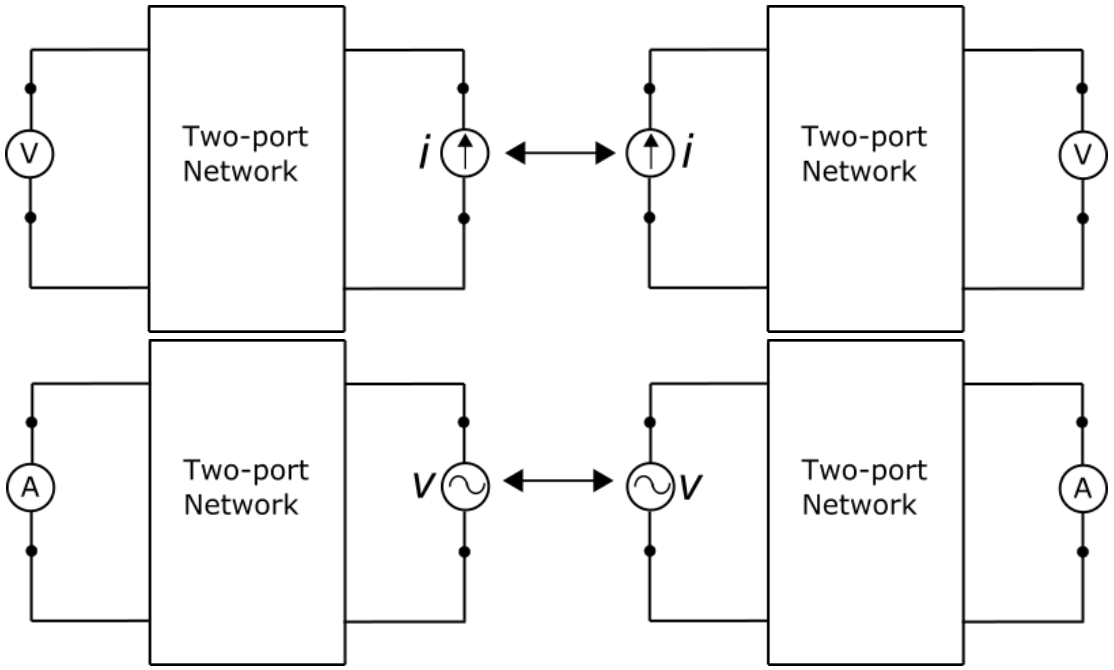

Figure 3.1 Schematic diagrams showing the reciprocity theorem of a two-port network analysis. On the right-hand side of each two-port network is the output and on the left-hand side is the input. (top-left) A current source is placed at the output and a voltmeter is placed at the input. (top-right) The location of the current source and the voltmeter can be swapped and the voltage to current ratio remains the same. (bottom-left) a voltage source is placed at the output and an Ammeter is placed at the input. (bottom-right) The location of the voltage source and the Ammeter can be swapped.

3.1.3 Coil design

To validate the coil simulations, a two-channel saddle coil array was built and is shown in Figure 3.2. It is composed of two surface loops with one loop on an inner acrylic cylinder of 14 cm diameter and 25 cm length. The second loop is mounted on a outer cardboard cylinder with a diameter of 14.4 cm. This design allows the cylinders to be nested such that the outer cardboard cylinder can be rotated around the inner acrylic cylinder. Each coil element was made from 5 mm wide copper tape. Low-input impedance preamps (Hi-Q.A. Inc., MPB-123R20-90) were used to further reduce mutual inductive coupling.

(A)

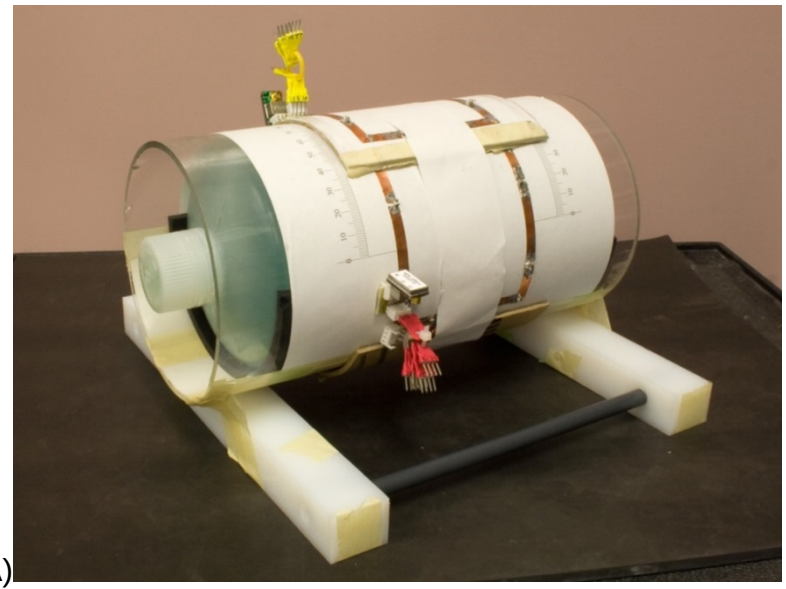

(B)

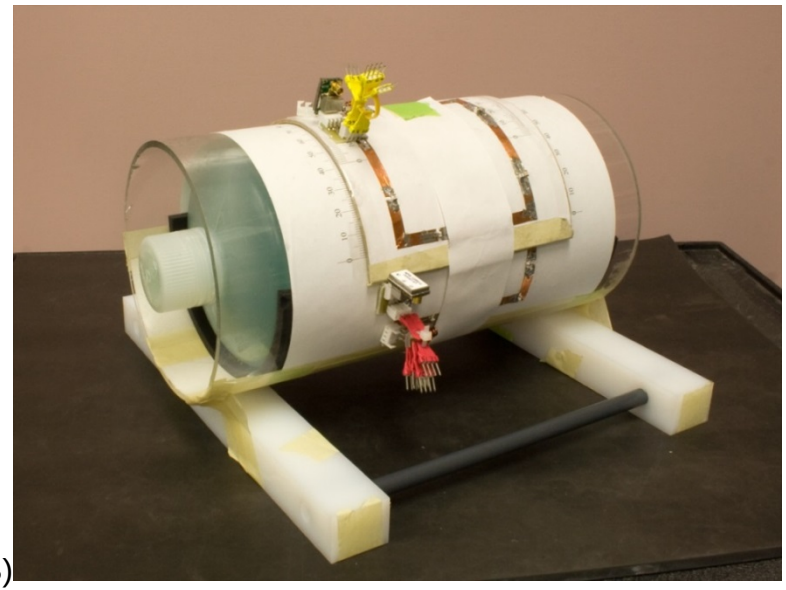

Figure 3.2 Photograph showing the coil used for verifying the simulation. The outer coil element is rotated (A) 90^o and (B) 40^o with respect to the inner coil. Here the bottle phantom is in place.

A schematic diagram of the equivalent circuit for the coil is shown in Figure 3.3. Here two loops represent the two channels of the saddle coil array. For each loop C_t is the tuning capacitor and C_m and L_m are the matching capacitor and inductor. The preamplifiers have input impedances of R_{p1} and R_{p2}. Lastly, R_1 and R_2 represent the resistances of the loops. The two loops are coupled inductively through the loop inductances L_1 and L_2. As a result, mutual inductance M is characterized by an inductive

coupling coefficient k_m multiplied by $\sqrt{L_1 L_2}$. In general, inductive coupling is undesirable because it will lower the coil sensitivity at the resonance frequency. Thus a decoupling method is needed. There are several methods that can be applied to decouple the loops. Here preamplifiers are used to decouple the loops as shown in Figure 3.3. With this method, we make use of low-input-impedance preamplifiers to make the impedance of each loop very high at the resonance frequency. Therefore, the induced current on the neighboring loop is very low.

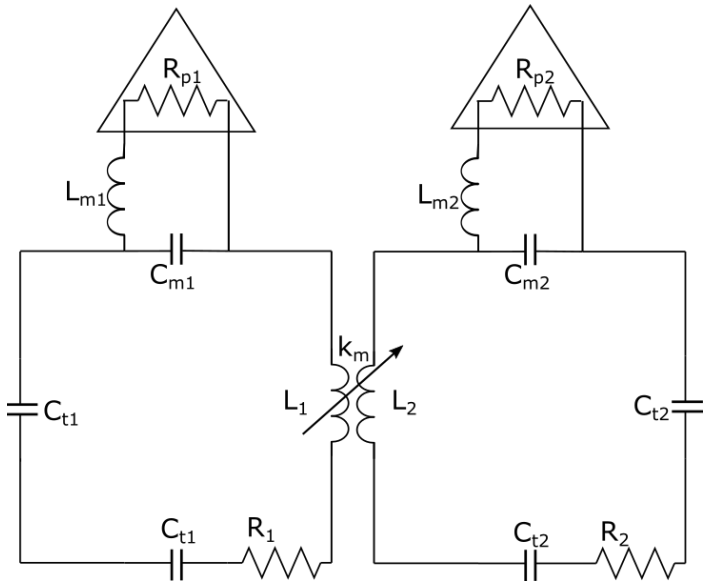

Figure 3.3 Schematic showing the equivalent circuit of the coil shown in Figure 3.2. This design allows the input impedance of each preamplifier to be altered by changing the matching capacitor or resistor.

3.1.4 Preamplifier decoupling

To better explain the preamplifier decoupling method, we make the use of Figure 3.4, which is a simplified version of Figure 3.3. For simplicity, we assume the two loops in Figure 3.4 are identical (i.e., $R_1 = R_2$, $R_{p1} = R_{p2} = R_p$ and $L_1 = L_2 = L$) and resonate at the same frequency ω. Also, only one loop is connected to a preamplifier and matched

to 50 ohms. The impedance looking into port A is expressed by the following equation [85]:

$$Z_A = R_1 + \frac{\omega^2 L^2 k_m^2}{R_1 + (X_{m2}^2 / R_{p2})} \tag{3.2}$$

where $$X_{m2} = 1/\omega C_{m2} \tag{3.3}$$

and the term in brackets is the impedance due to the preamplifier.

If the input impedance R_p of the preamplifier is close to zero then the impedance Z_A is equal to R_1. This means the loop with the preamplifier is invisible to the neighboring loop. Preamplifier decoupling can be achieved by using a preamplifier with very low input impedance R_p. Our hypothesis is that for validating simulations in various coupling conditions, the impedance added to the loop by the preamplifier can be changed by adding resistors or by matching the loop to other than 50 ohms.

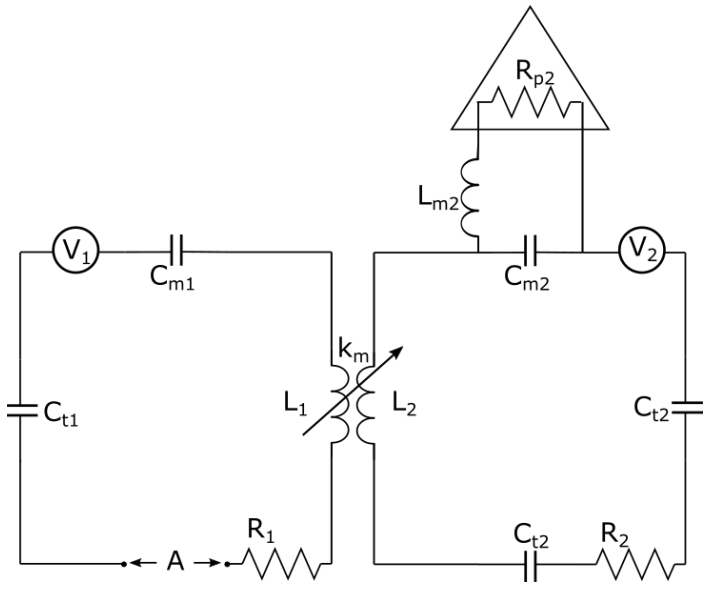

Figure 3.4 Schematic illustrating how the preamplifier is used to decouple the two loops. Port A is shown on the bottom left.

3.1.5 Inductive coupling

In circuit theory analysis, if two identical loops are tuned to the same resonance frequency and placed close to each other (Figure 3.5) then these loops will be inductively coupled through their mutual inductance M. Assume a sinusoidal voltage V_1 is applied to one loop having an impedance Z_1. When the two loops are coupled, a coupled impedance $(\omega M)^2/Z_2$ is added into the circuit of the driven loop by its neighboring loop. Consequently, the current flow in the driven loop is reduced and expressed as $I_{driven} = V_1/[Z_1+(\omega M)^2/Z_2]$. In addition, the current induced in the neighboring loop $I_{induced}$ is proportional to both I_{driven} and the mutual inductance M. Hence an inductive coupling coefficient k_m can be calculated by taking the ratio of the induced current in the neighboring loop to the flowing current in the driven loop. This is usually normalized to give

$$k_m = \frac{\left\{I_{induced}/I_{driven}\right\}_{\phi}}{\left\{I_{induced}/I_{driven}\right\}_{\phi=0^o}} \tag{3.4}$$

where ϕ is the separation angle between two loops. The inductive coupling coefficient k_m is a maximum when the two loops perfectly overlap where $\phi=0^o$ (coaxial coil configuration). However, in practice k_m is usually minimized to get a better SNR.

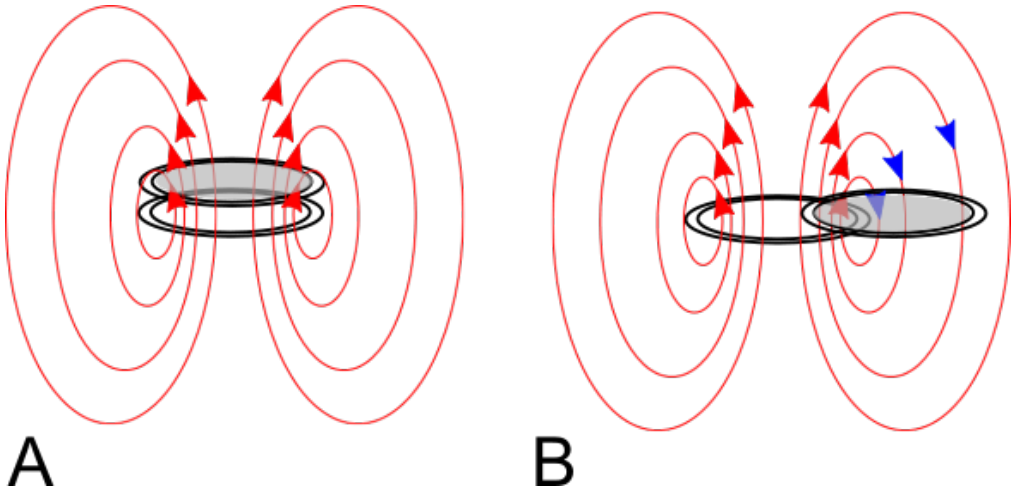

Figure 3.5 Schematic illustrating inductive coupling between two loops. (A) is the condition of the strongest coupling because flux is maximum when one loop is on top of the other one. (B) is minimum coupling because the net flux through the neighboring loop is zero. A non-zero flux through the neighbouring loop will induce a current in that loop.

3.1.6 Electric coupling

In section 3.1.4, we showed the noise originating from the sample for a single loop (Equation 3.1). However when a multi-loop array receive coil is used, the shared resistance must be considered. In analogy to the mutual inductance, the two loops are also electrically coupled through their shared resistance resulting from the sample. In general, when two loops are coupled inductively or electrically or both, they have a mutual inductance (M_{ij}) and a shared resistance (R_{ij}). This is shown as a schematic in Figure 3.6 where Z_1 and Z_2 are the impedances of each loop. The important point is the mutual inductance can be canceled by several methods. However, the shared resistance cannot be easily removed. It will require other resistive network, which leads to more loss in SNR of images.

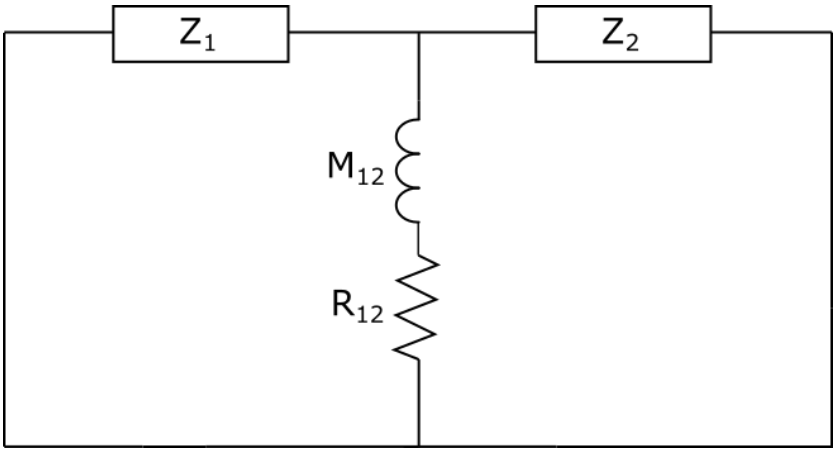

Figure 3.6 Schematic showing the coupled two-channel coil with a loading sample. Here the coil elements have coil impedances Z_1 and Z_2 and are coupled through their mutual inductance M_{12} and shared resistance R_{12}.

As mentioned in section 3.1.4, the source of the noise is from thermal noise in the imaged sample. When a multi-loop array receive coil is used, noise voltages due to Brownian motion will be detected on both loops simultaneously. Thus, both loops detect the same noise and the voltages are consequently correlated. Using a long wavelength approximation, it is assumed that the induced voltages have a phase difference of either 0^0 or 180^0 [87], [88]. Because the shared resistance will affect the SNR of the image, the noise covariance matrix is essential for image reconstruction [89]. The noise covariance function is given by rewriting the Equation (3.1) as

$$\left\langle V_i(t)\, V_j(t) \right\rangle = 4\, k\, T\, \Delta f\, R_{ij} \tag{3.5}$$

In the time domain, the left-hand side of Equation (3.5) can be expressed by

$$\left\langle V_i(t)\, V_j(t) \right\rangle = \frac{1}{\Delta t} \int_{\Delta t} V_i(t)\, V_j(t)\, dt \tag{3.6}$$

which means the noise covariance can be obtained by sampling the voltage values from each loop at each time point for a long time and then taking the time average. Here Δt is the time length for measuring the voltage. Although this method is straightforward, it is

not capable of distinguishing the sources of the voltages, whether they are from the sample noise or the MR signal. In practice, it is possible to use MR images as the source of the measurements.

The advantage of using images is that the sample and the background are easy to determine. The noise covariance information can be obtained by simultaneously acquiring MR images with the multiple loops of the array. The measured voltage on each coil is related to the MR images by applying Parseval's theorem. Hence, the voltage covariance between the loops is equal to the covariance of the MR images intensities in the background region acquired by each loop. Mathematically, this can be expressed as

$$\left\langle V_i(t)\, V_j(t) \right\rangle = \left\langle S_i(r)\, S_j(r) \right\rangle \tag{3.7}$$

where S_i is the intensity of an MR image for one loop and S_j is for the other loop. Both images will depend on the sensitivity maps of their respective loops.

The induced voltages and their associated sensitivity maps will cause an electric power (P) loss in the sample [90] due to the shared resistance. This can be expressed as

$$P_{ij} = \int_v \frac{\sigma}{2}(\vec{r}) E_i(\vec{r}) \cdot E_j(\vec{r})\, dv \tag{3.8}$$

Here E(r) is the electric field and r is the position vector for the electric field. We assume the resistances of the conductors of the RF coil are ignored. Applying a power equation, $P = I^2R$, the shared resistance can be expressed as

$$R_{ij} = \frac{\int_v \frac{\sigma}{2}(\vec{r})E_i(\vec{r}) \cdot E_j(\vec{r})\,dv}{I_i I_j} \tag{3.9}$$

This shared resistance, R_{ij}, is a function of the conductivity of the sample and the E-field maps of each loop. The sample has a conductivity of σ, and in many cases σ is assumed to be a constant. Here the E-fields are induced in the sample by driving a unit current either in loop i in isolation or in loop j in isolation. These E-fields are difficult to measure inside a sample but can be simulated and usually are complex fields in a full-wave EM simulation. It is important that the fields are only acquired after simulations reach a steady-state. Then an n-by-n noise covariance matrix for an n-loop receive array coil can be established. The diagonal terms of this matrix represent the absorbing power due to the coil self-resistance and the off-diagonal terms are equivalent to the shared resistances. In addition, an electric coupling coefficient (k_e) is defined by [85], [87] which is represented by the normalized noise correlation coefficient determined from images. Note that only when the inductive coupling is zero, k_e equals to normalized noise correlation coefficient.

$$k_e = \frac{R_{ij}}{\sqrt{R_{ii} R_{jj}}} \tag{3.10}$$

3.1.7 Aim

A goal of this thesis is to design a transmit/receive array coil. Most coil simulations assume no inductive coupling between loops [85], [91]. Hence, loops are simulated in isolation. This is a simple and fast way to simulate RF coils. However, this assumption is not always true. In particular, this approach is not suitable for designing a transmit array coil as opposed to designing a receive array coil. The normalized noise correlation

coefficient is defined with an assumption of zero mutual inductance. However, in the multi-loop array coil case this assumption might not always be true. Therefore, the simulation might not be accurate. If there is inductive coupling it adds an imaginary part to Equation 3.10 and should change the electric coupling coefficient. To our knowledge, how inductive coupling affects the electric coupling coefficient has not been investigated yet. Hence, the aim of this study is to investigate the impact of the inductive coupling on the noise covariance matrix from which the electric coupling coefficient is calculated.

3.2 Materials and methods

3.2.1 Full-wave EM simulation

Simulations of the coil were performed using a finite-difference time-domain (FDTD) method (SEMCAD X v14.8, ZMT, Zurich, Switzland). This software implements a three-dimensional full-wave simulation. The RF coil configuration in Figure 3.7 was modeled based on the constructed coil (Figure 3.2) which has loop dimensions of 9.8 cm by 9 cm. A model of this two-channel saddle coil array was loaded with a homogenous phantom having a conductivity of 0.73 S/m. The inner loop was kept at a fixed position but the outer loop was rotated around the inner loop to a variety of overlapping positions. A minimum mesh size of 3 million cells was used to discretize the computational space. Although the free space region was meshed with a much coarser grid, which leads to less sensitivity to field variations in the free space region, the overall accuracy in the region of interest was retained and the computation time could be significantly reduced. The copper traces of the loops of the RF coil model were discretized using a thin resistive sheet approximation because the thicknesses of the copper traces were much smaller than both the cell sizes and the operating wavelength. This approximation is

important to avoid a consequential high computational load. Because it is impractical to process an infinite amount of data, the size of the computational domain was confined by applying a boundary condition to truncate the computational domain. An absorbing boundary condition (ABC), which was a default setting in the software, was chosen in the simulations. This is an ideal boundary condition that absorbed the outgoing numerical wave and only allowed a small amount of reflecting wave (~1%) that otherwise may have distorted the fields of interest when the parameters of the ABC is properly setup.

Each loop had eight capacitors for tuning to 123.2 MHz: an edge source was placed in parallel with one of these capacitors for matching. The edge source was a voltage source with an internal impedance of 50 ohms and it generated a Gaussian pulse (shown in Figure 3.8) for broadband simulations. The pulse length was set to 40 cycles to ensure the pulse was long enough to dissipate the source power in the defined bandwidth. For an initial value, the matching capacitor for each loop was determined from a bench measurement of the physical coil. Tuning and matching procedures were performed with each simulated loop in isolation. It was necessary to repeat these procedures several times until the loop was perfectly tuned and matched. To obtain a receive field, we applied the concept of reciprocity to the simulations. An EM field in the sample was induced by driving one loop while both loops were connected to preamplifier circuits for decoupling. Because of reciprocity the transmit field also represented the receive field. Therefore, the EM fields of two sequentially simulated loops were obtained. Current sensors were placed, in software, on each leg of each loop to monitor the current distributions. The resulting current amplitudes were applied

to Equation 3.4 to obtained inductive coupling analysis. To reduce the data storage requirements, a volume field sensor was added to extract EM fields from the defined space only at resonance frequency. The resulting E-fields were used for noise covariance analysis (Equation 3.10) to estimate the electric coupling. Hence, we simulated both coupling coefficients to characterize the coil.

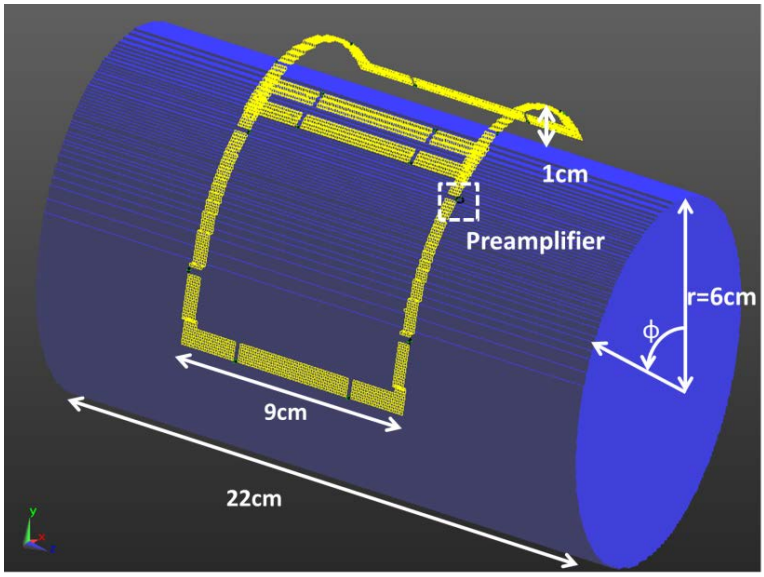

Figure 3.7 Schematic showing the two-loop coil as used in the simulations. The angle (ϕ) between the two loops could be varied.

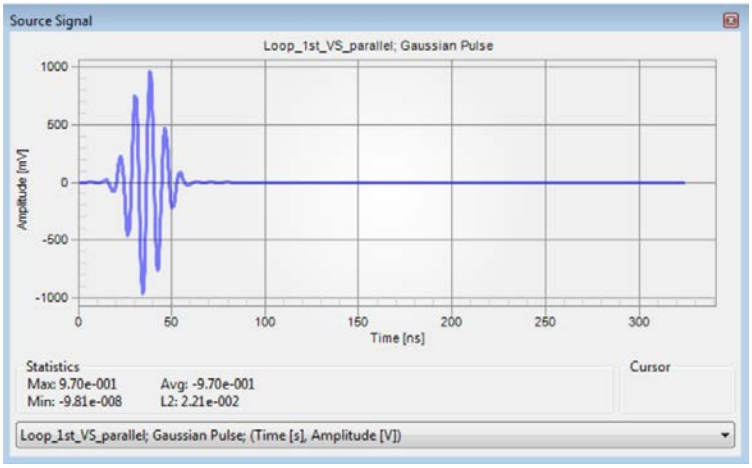

Figure 3.8 Diagram showing a Gaussian pulse generated by a voltage source that drives loops in broadband simulations.

3.2.2 Preamplifier circuit simulation

The overlap decoupling method can only minimize the mutual inductance between neighboring loops. For coils with more than two loops, a small amount of mutual inductance usually exists in the coil array. The other decoupling method, i.e., low input impedance preamplifier isolation, is also widely used for mutual inductance cancellation. To show that the simulations of coil design properly incorporated inductive coupling into the noise covariance matrix, a preamplifier circuit was added to each coil loop. The preamplifier was tuned by connecting an inductor in series with the matching capacitor to transform a high blocking impedance at the resonance frequency and hence significantly reduce the induced current in the neighbouring loop. The tuning and matching of each loop at different coil separation angles was initially determined in isolation, i.e., we simulated one loop at a time. To ensure each loop was properly matched, the reflection coefficient (S_{11}) for each coil element was kept smaller than -25 dB. By adjusting the input impedance of the preamplifier, the amount of induced current in the neighboring loop was altered and hence the induced EM field, containing coupling information, was also altered. Since the coupling information was expected to be present in the noise covariance matrix, we applied noise covariance analysis to characterize the simulations.

To model a receive field, we applied the concept of reciprocity to the simulations. An EM field in the sample was induced by driving one loop while either one or both loops were connected to preamplifier circuits for decoupling. The resulting E- field was used for noise correlation coefficient analysis. Therefore, the E-fields of two sequentially simulated loops were obtained for further noise correlation analysis.

It has been shown that even if the mutual inductance between two loops can be canceled with a preamplifier decoupling circuit, a shared resistance results from coupling through the conductive sample [85]. To investigate the coupling due to the mutual inductance and shared resistance, we simulated the coil with different preamplifiers connected to it. There are two ways to alter the blocking impedance (Z_p) due to the preamplifiers. Method (I): varying the input impedance (R_p) of a preamplifier (see Equation 3.2) where the matching impedance (Z_m) of the loop is 50 ohms and is fixed. Thus the blocking impedance is inversely proportional to the input impedance of each preamplifier (i.e., $Z_p = X_m^2 / R_p$ and $X_m^2 = 50$). The mutual inductance between the loops is a function of their overlap and is easily varied. Several preamplifier input impedances in the range of 0 to 50 ohms were simulated with different coil separation angles (phi = 60^o, 63^o, 63.5^o, 64^o, 64.5^o, 65^o, 65.5^o, 65^o, 66^o, 69^o, 75^o, and 85^o). Method (II): varying the matching impedance (Z_m) of the loop would change the reactance (X_m) (see Equation 3.3). Thus, the blocking impedance was proportional to the matching impedance (i.e., $Z_p = R_{sample}/R_p \bullet Z_m$). We simulated several matching impedances (Z_m = 12.5, 24, 36, 50, 100, and 200 ohms) with overlapping positions having the same angles as the first method.

3.2.3 Measurements of constructed coil

Each of the two loops was tuned and matched to 50 ohms separately with a bottle phantom (Siemens 1900 ml, length = 22 cm, diameter = 12 cm with chemical ingredients of $NiSO_4$, NaCl, and H_2O) in place. There was a 1 cm gap between the inner loop and the bottle phantom. Bench measurements were made using a calibrated network analyzer (Agilent E5601A). Data were transferred either by a screenshot or by

a local area network connection to a computer running acquisition software (LabView, National instruments). Measurements of scattering parameters (S-parameters), i.e., S_{11} and S_{21}, (e.g. Figure 3.9) were performed for tuning and matching of the loops. In addition, measurements were made of the isolation between the two loops, preamplifier detuning, cable trap resonance and Q-factors.

The mutual inductance between the nearest neighboring loops was minimized by finding the overlapping position where S_{21} was minimum in an unloaded condition. To further improve the decoupling of the coil, a preamplifier decoupling network was added and measurements were made with various coil separation angles.

Image acquisition was conducted on a 3T MRI scanner (Siemens, Tim Trio). Imaging parameters were as follows: FOV = 300 mm; TR = 25 ms; TE = 10 ms; slice thickness = 3 mm; matrix size = 256 x 512. Pure noise maps were acquired by setting the RF transmit power to zero. For comparison, an alternative to acquiring noise maps was to select an ROI from the background of images of the sample (with the RF power on). These noise maps were used to calculate a noise correlation matrix using Musaik (ZMT, Zurich, Switzerland). The selected ROI for the noise correlation calculation needed to be sufficiently large to get a good estimate of the sample standard deviation while avoiding the edges of the sample. Thus, we used an ROI that contained at least 38,750 sample points. In addition, SNR maps were calculated by dividing the signal generated from the bottle phantom by the standard deviation of the noise in the background. The systematic error of the measurements was estimated by moving out the table of the MR scanner and moving the table back to the iso-center and the RF coil was realigned to the separation angle of zero inductive coupling. This procedure was

repeated six times and the noise correlation coefficients were measured each time. The random error was made by applying a sequential six measurements without moving the table and coil.

3.3 Results

To verify the tuning and matching of each loop, the network analyzer was used to measure the S-parameters. Figure 3.9 (top right) shows the transmission coefficient (S_{12}) plotted as a function of frequency. There is a peak at a frequency of 123.2 MHz, which corresponded to the Larmor frequency and the Smith chart showed the coil was matched to 51.6 ohms. This is very close to the source impedance of the network analyzer, i.e., 50 ohms. The reflection coefficient plotted as a function of frequency had a single dip of -35 dB at the resonance frequency. This is expected because the loop was closely matched to 50 ohms. Figure 3.10 shows the transmission coefficient with the preamplifier in place. The dip (loss) at resonance frequency is due to the high impedance of the preamplifier circuit, and was tuned to the resonance frequency with either a capacitor or an inductor to transform each blocking impedance.

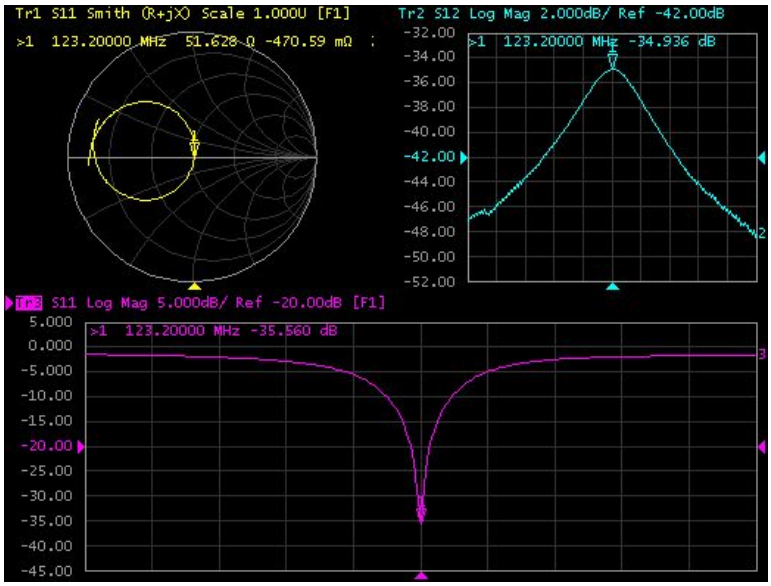

Figure 3.9 Graphs showing the measurements of scatter parameters of the inner loop. The loop was properly tuned to 123.2 MHz and matched to 50 ohms.

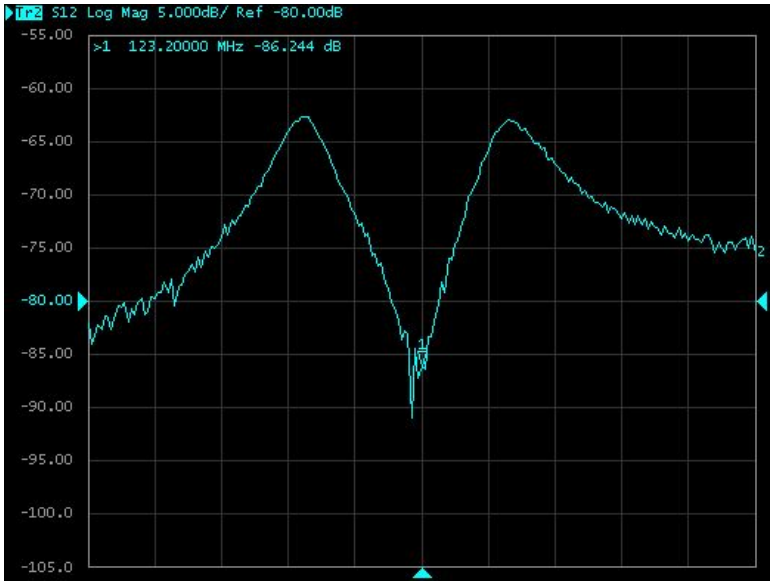

Figure 3.10 Graph showing the transmission coefficient plotted as function of frequency when the preamplifier was in place. Decoupling presents a large impedance at the resonance frequency.

In order to find the angular position corresponding to zero mutual inductance, the ratio of currents (log magnitude) of the two loops were measured and are plotted in Figure 3.11 as a function of the coil separation angle. It can be seen there is a minimum coupling near 64.5^{o}. The Q-factor was also measured and is shown in Figure 3.12 as a

function of the coil separation angle. Here the loaded Q-factor was measured with the 3-dB method [92] from the inner loop, which was also driven. It can be seen that the Q-factor is a complicated function of coil separation angle. There is a subtle local maximum near 64.5^{o}. This might be expected because the mutual inductance is minimized at this angle [93].

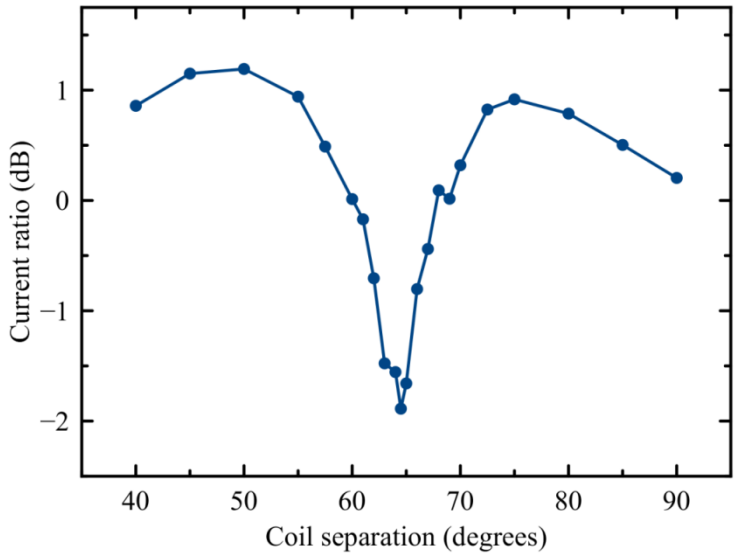

Figure 3.11 Graph showing the ratio of currents in two coil elements plotted as a function of the coil separation angle. There is a minimum coupling at 64.5^{o}.

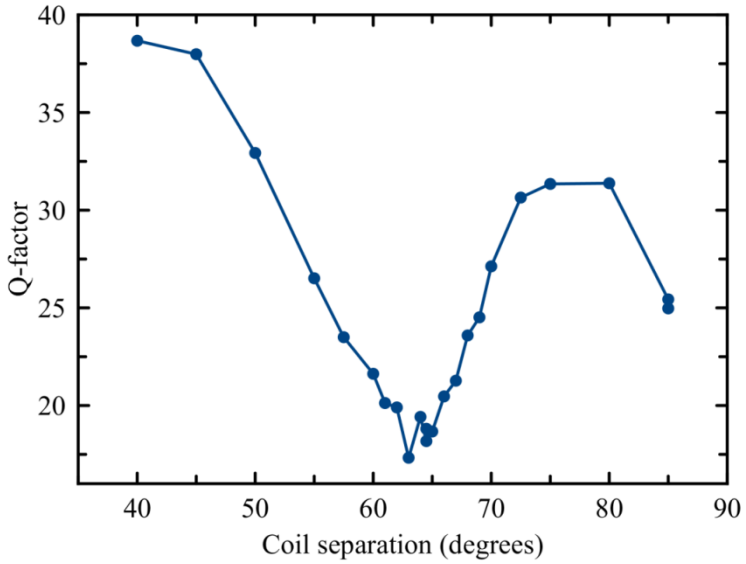

Figure 3.12 Graph showing the Q-factor of the driven coil element plotted as a function of the coil separation angle. There is a subtle local maximum Q-factor near 64.5^{o}.

3.3.1 k_m and k_e curves

As a general verification of the simulations, we measured k_m of the corresponding unloaded coil with a network analyzer. In addition, the inductive coupling coefficient k_m and electric coupling coefficient k_e were determined from simulations using Equations 3.4 and 3.10. These are plotted in Figure 3.13 as a function of the coil separation angle. It can be seen that k_m is zero when the coil separation angle is 64.5^{o} for both simulation and measurement. In addition, k_e is zero at about 85^{o}. This is expected since although there is zero mutual inductance at 64.5^{o}, the E-fields are still coupled. This is typical of a real coil and the general shapes of the k_m and k_e plots are consistent with the predictions shown in the literature [85], [91].

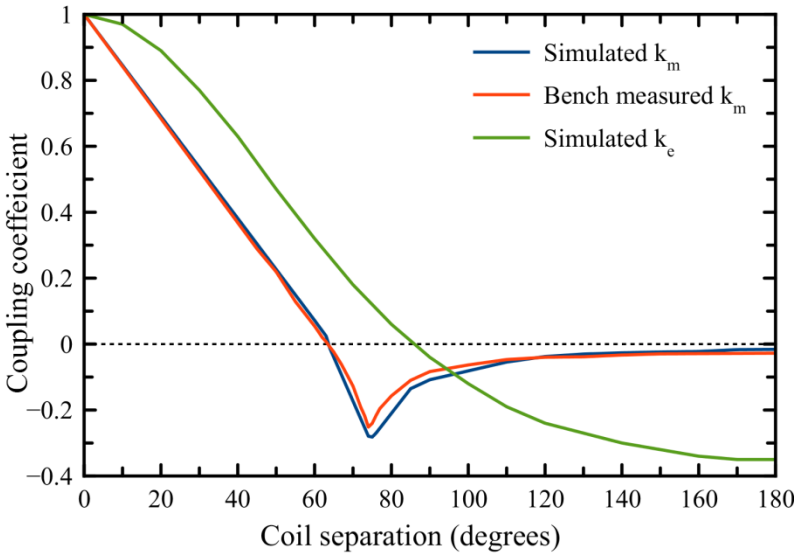

Figure 3.13 Plots showing the simulated (blue) and measured (red) inductive coupling coefficient k_m and electric coupling coefficient k_e (green) as a function of the coil separation angles. Zero k_m is at 64.5^o in both simulation and measurement. However, zero k_e is at about 85^o.

3.3.2 Small-loop pair

Ideally, if the inductive coupling is zero, its noise correlation coefficient will be independent of preamplifier decoupling. However, the coil separation angle (64.5^o) corresponding to zero coupling will vary with the input impedance of the preamplifier (R_p). This suggests that the inductive coupling at phi of 64.5^o is small but not zero. To find the noise correlation coefficients at true zero inductive coupling, a pair of small loops representing shared inductors was added to the overlapping legs (see Figure 3.14). These small loops will increase or decrease the coupling depending on their diameter and how they are connected to the overlapping legs. The idea is to vary these small loops until zero inductive coupling is found. The noise correlation coefficients for various small loops are plotted in Figure 3.15 as a function of input impedance of the preamplifier. The ideal case of true zero inductive coupling is illustrated by the dashed line. For the case of no small loops (dark blue line) it can be seen that the noise

correlation coefficients decreased as a function of the input impedance of the preamplifier. Adding a small loop pair in parallel (red line) increased the inductive coupling and thus the plot of noise correlation coefficients decreased faster than the case of no small loops. In contrast, adding antiparallel small loop pairs decreased the inductive coupling. It can be seen that as an area of the antiparallel small loops increases, the plots of the noise correlation coefficients show a reversed trend. This means a true zero inductive coupling exists and can be found when a proper size of small loop pair is used. Although we can remove all inductive coupling in principle, it is not practical to add a small loop pair to every simulation because of a greatly increased computational load. Hence, in all following simulations a small loop pair was not used.

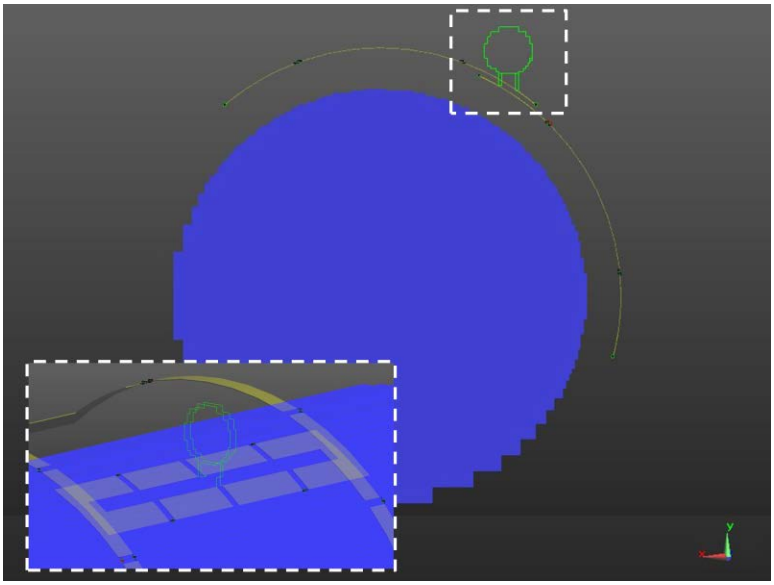

Figure 3.14 Diagram showing the small loop pair used to alter inductive coupling between the coil loops.

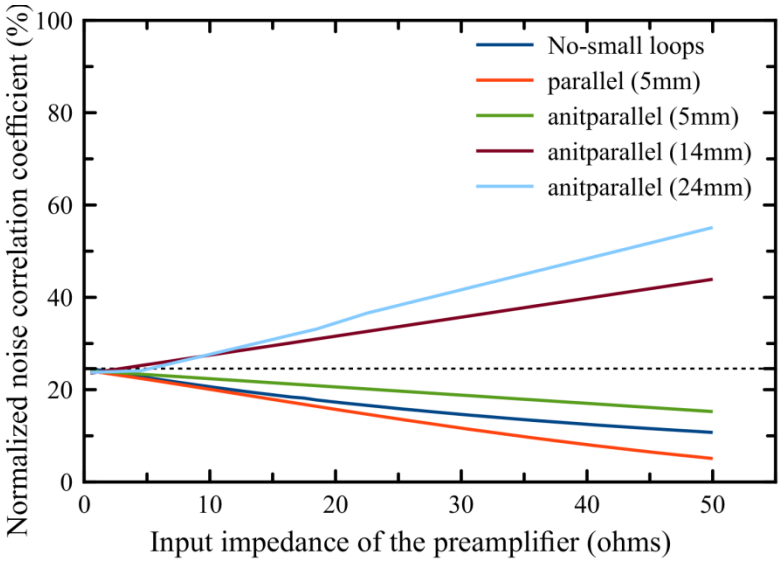

Figure 3.15 Plots showing the simulated normalized noise correlation coefficients plotted as a function of input impedance of the preamplifier. Here the small loop pair shown in Figure 3.14 was added to the model.

3.3.3 Varying coil separation angle

To establish a baseline of the measured noise correlation coefficients when a combination of preamplifier and overlapping decoupling were used, the normalized noise correlation coefficients are plotted as a function of the coil separation angles in Figure 3.16. Here a preamplifier was connected to each loop. We did not alter the performance of the preamplifier by varying the matching impedance of the loop. In the range of phi = 60^{o} to 75^{o}, the measured noise correlation coefficients (blue circles) showed a descending trend which agrees qualitatively with the simulated k_e plotted in Figure 3.13. However, there is an increase in the coefficients above 75^{o}. Hence, we can deduce there is a coil separation angle where the noise correlation coefficient is zero. Interestingly, the measured noise correlation coefficient is zero at phi = 68^{o}. It is not surprising that this angle disagrees with the prediction made by simulations (red diamonds), which had a minimum k_e at 85^{o} (determined in isolation). But this prediction assumed zero inductive coupling. In order to incorporate inductive coupling to the noise

correlation coefficient, we created a *Mode*, i.e. a new set of field maps of a single channel. This process combines multiple data sets of a single-channel simulation into a new channel with different weightings of amplitude and respective phase. If the loops are coupled, the field maps will be different from that of a single channel due to inductive coupling. Hence, we can create a *Mode* to represent realistic fields of the transmitting loop by superposing the fields of a single-channel simulation of the transmitting loop added to the induced fields in the coupled loop with proper weighting of amplitude and phase. Here the induced field is represented by the fields of a single-channel simulation from the neighboring loop. According to Faraday's law of induction and Lenz's law, a voltage induced in the coupled loop has a 90^o phase delay with respected to the driving current in the transmitting loop. Hence the induced magnetic field has an initial phase of 90^o, and its associated induced electric field has a phase of 180^o. To show the accuracy of the simulations, we found weighting of amplitudes, which equals to its corresponding k_m values for five coil separation angles with respect to the transmitting loop to mimic the induced field. The new simulated noise correlation coefficients (Figure 3.16 A, green squares) are much closer to the measured data. Their images also have a good agreement as shown in Figure 3.17. Both measured and simulated phase of the noise correlation coefficient (Figure 3.16) show a 180^o phase difference before and after phi = 68^o where the noise correlation coefficient is almost zero. This is expected since the noise correlation coefficient changes a sign before and after phi = 68^o.

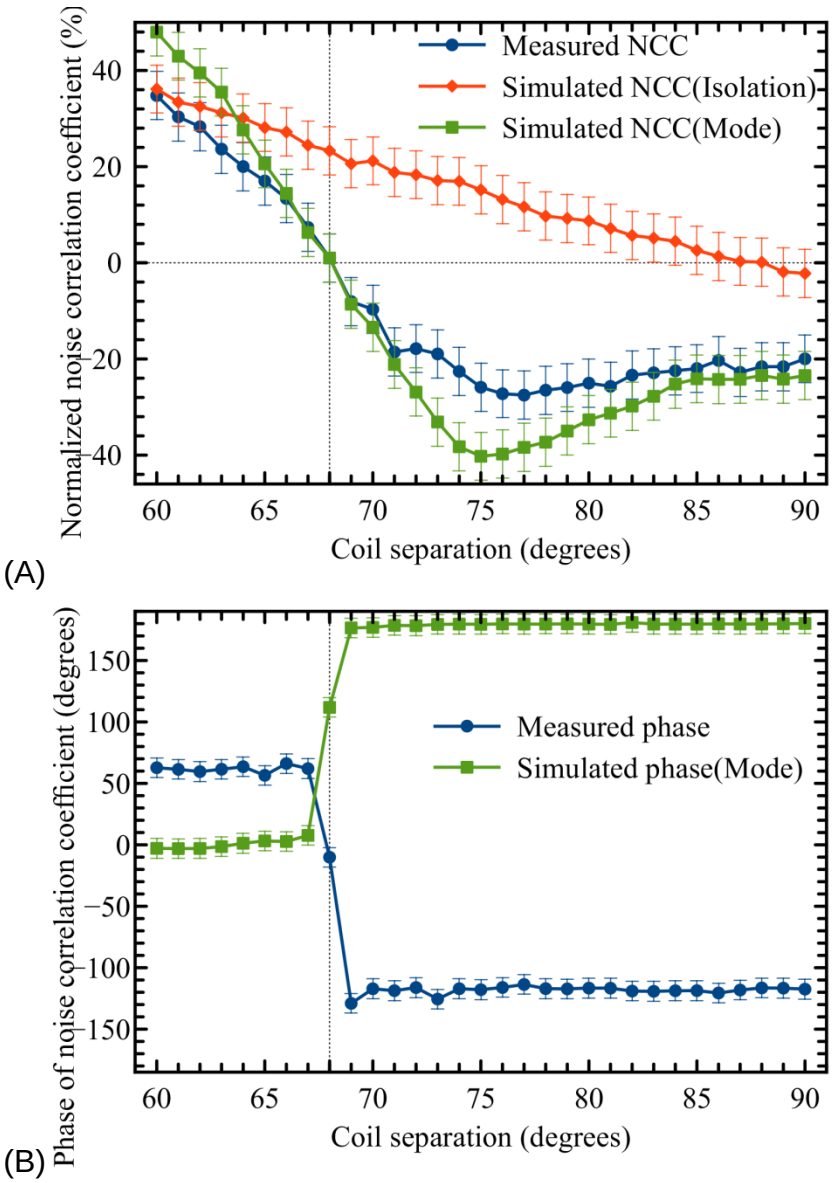

Figure 3.16 Plot illustrating the (A) magnitude and (B) phase of noise correlation coefficients from measurements of images as a function of coil separation angle. A preamplifier was connected to each loop (Z_m = 50 ohms) with built-in input impedance of 1.5 ohms.

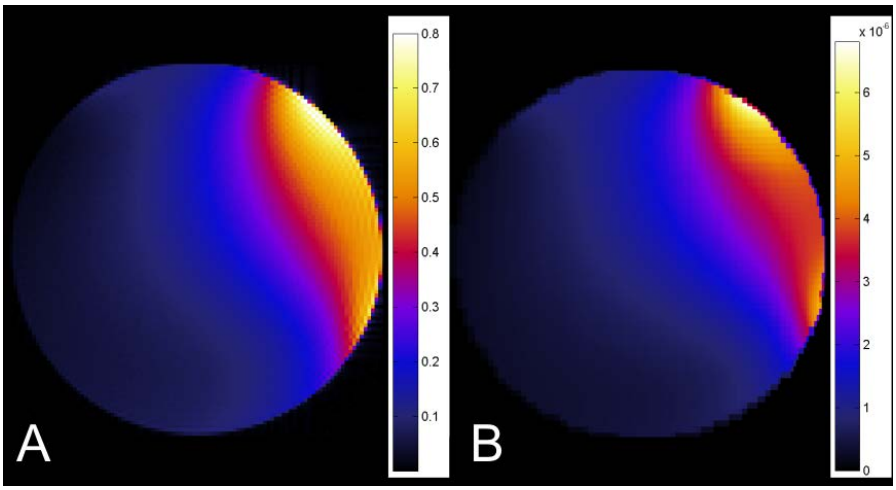

Figure 3.17 Images showing the SNR maps produced by the inner loop of the coil for (A) measurement and (B) simulation. A preamplifier was connected to each loop (Z_m = 50 ohms) with built-in input impedance of 1.5 ohms.

3.3.4 Method I: Varying input impedances of a preamplifier

3.3.4.1 Large coil separation angle

To validate the simulations, normalized noise correlation coefficients were calculated from simulated field maps obtained with various input impedances (R_p) of the preamplifier. These normalized noise correlation coefficients are plotted as a function of the input impedance of the preamplifier in Figure 3.18. Both simulated and measured normalized noise correlation coefficients are shown in Figure 3.18 for three coil separation angles. These angles, 64.5^o, 85^o and 75^o represent zero mutual inductance, zero shared resistance and the mix of the two respectively. In Figure 3.18 A, all three plotted lines show a descending trend at low input impedances. However, plots of 75^o and 85^o show an ascending trend after 10.5 and 4.5 ohms respectively. The difference in their slopes near 3.5 ohms might due to their strong inductive coupling coefficients (shown in Figure 3.13), such that the simulated preamplifier circuit becomes dysfunctional. In addition, the plot of 75^o has the largest negative k_m which might be

related to the steepest slope. Shown in Figure 3.18 B are the corresponding measured noise correlation coefficients. It can be seen that only the measured plot for 64.5^{o} shows agreement between the simulation and the measurement. Both of these plots descend as the input impedance increases and the normalized noise correlation coefficients are roughly similar (25% and 16%). The plots of 75^{o} and 85^{o} show an opposite trend between the measurement and the simulation. This might be due to the preamplifiers on the constructed coil not being capable of decoupling the loops while the simulated preamplifier circuit performed perfectly.

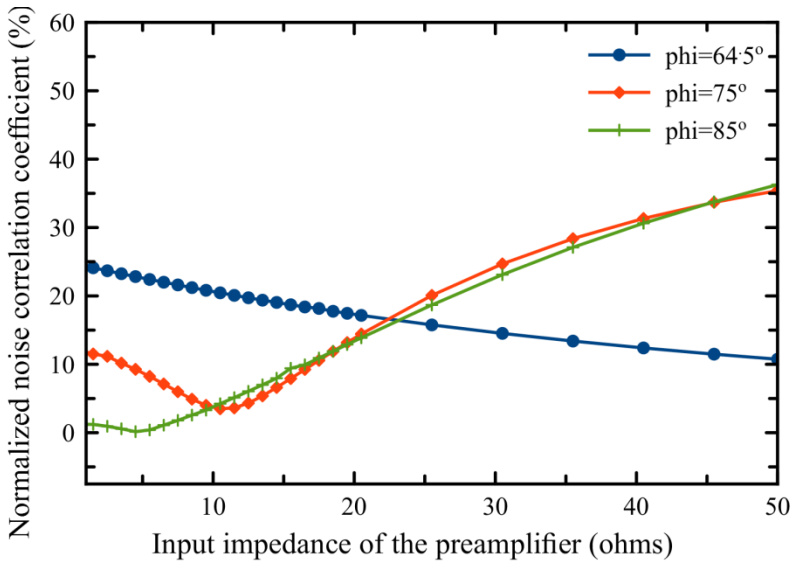

(A)

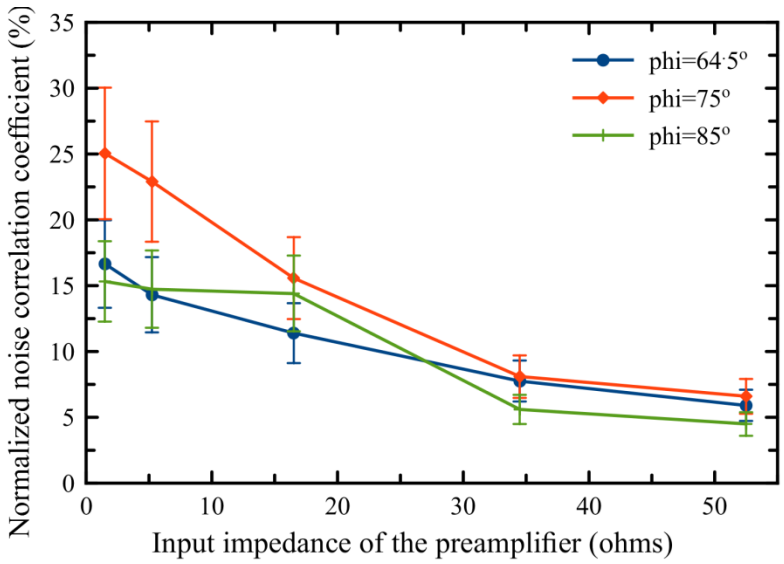

(B)

Figure 3.18 Plots showing the noise correlation coefficients obtained from (A) the simulations and (B) the experiments for three coil separation angles. The angles 75° and 85° were large deviations from the perfectly overlapped decoupled angle.

3.3.4.2 Small coil separation angle

The large coil separation angles of 75° and 85° may have resulted in overly strong inductive coupling and lead to the poor performance of the preamplifier decoupling. To further investigate this idea, the range of coil separation angles was narrowed down to 64.5° ± 4.5° for both simulations and measurements. The results are shown in Figure

3.19, and it can be seen that the simulation and measurements have roughly the same appearance. For completeness, the noise variance and covariance for the measurements are shown in Figure 3.20. All plots have a descending trend as the input impedance of the preamplifier is increased. In addition, the behavior as a function of angle has similar ordering. At the perfect overlap decoupling angle (phi = 64.5^{o}), the noise correlation coefficients show a good agreement between the simulation and the measurement (24% versus 21% at 3.5 ohms). However, the measurements made at larger coil separation angles (60^{o} and 69^{o}) disagree with simulations.

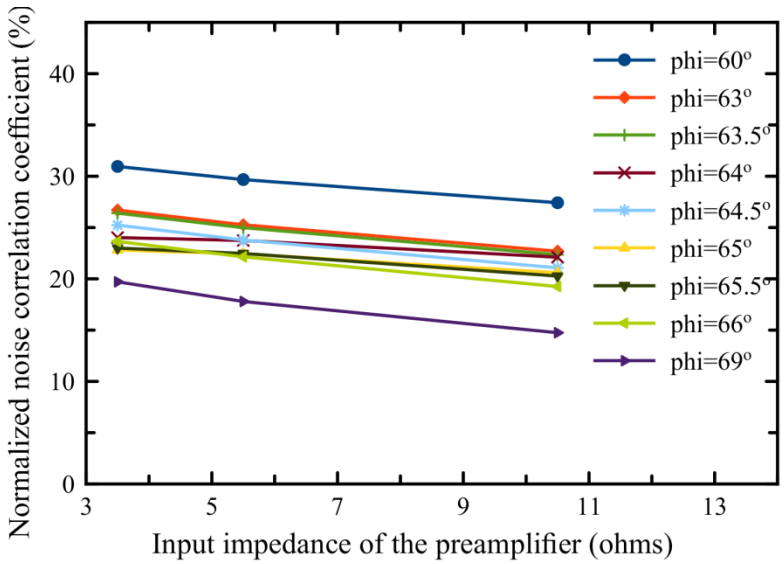

(A)

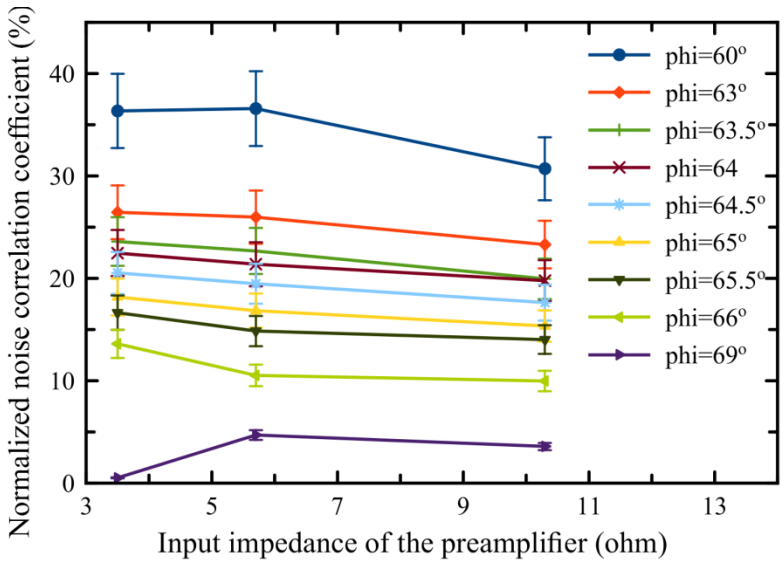

(B)

Figure 3.19 Plots illustrating the noise correlation coefficient from (A) the simulations and (B) the experiments for small coil separation angles.

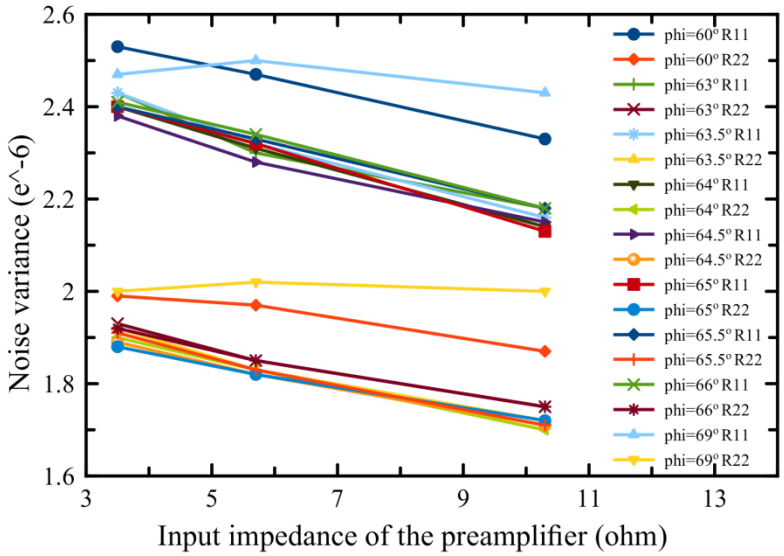

(A)

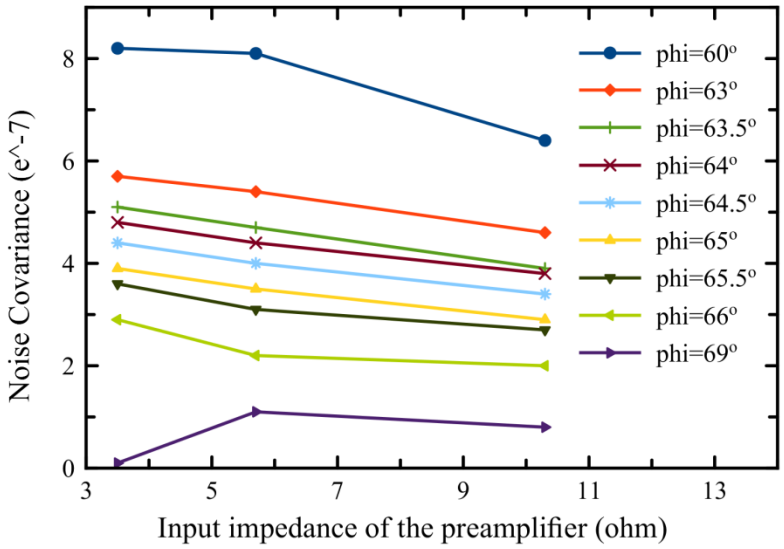

(B)

Figure 3.20 Plots showing the measured (A) noise variance for the inner loop (R11) and outer loop (R22) and (B) noise covariance for eight coil separation angles plotted as a function of input impedance of the preamplifier.

3.3.5 Method II: Varying the matching impedance of the loop

3.3.5.1 Scatter parameters simulation

Since the results of varying the input impedance of the preamplifier (Method I) led to poor agreement between the measurements and simulations for large angles, we altered the blocking impedance of the preamplifier by varying the matching impedance

of the loop (Method II). To show the feasibility of Method (II) in simulations, we obtained transmission coefficients (S_{21}) of the inner loop from simulations where both loops were present. These are plotted as a function of resonance frequency in Figure 3.21. Here, the S_{21} coefficients were obtained for the inner loop, which was both the driven and receiving loop. Dips at 123.2 MHz are observed in all plots and these are due to the blocking impedance of the preamplifier. In general, a higher matching impedance leads to a higher blocking impedance. Therefore, the S_{21} coefficient for Z_m = 200 ohms is much smaller than for the Z_m = 12.5 ohms case. To show that preamplifier decoupling was functioning properly for the non-driving loop, S_{21} coefficients are plotted verses frequency in Figure 3.22. It can be seen the dips have moved off resonance. Here S_{21} coefficients were measured from the outer loop when the inner loop was driven. It can be seen that for each Z_m the difference between the maximum peak S_{21} coefficient and the value at 123.2 MHz is about 18 dB. In addition, the plot for the Z_m = 200 ohms case has the largest difference in S_{21} coefficient, which is related to the higher blocking impedance added to the loop. This difference means only a small amount of power is transmitted to the outer loop from the inner loop as designed. Although the loops need to be retuned, all plots show good preamplifier decoupling at 123.2 MHz. A real coil would always have a preamplifier connected to each loop. To confirm the preamplifier circuit performed properly, simulations were performed with a preamplifier on the outer loop. For one set of the simulations this preamplifier was deactivated by using a large input impedance (R_p). There was no preamplifier on the driving loop, but this is not expected to affect the trend. The transmission coefficients (S_{21}) measured from outer loop are shown in Figure 3.23 as a function of resonance frequency. It can be seen that

the S_{21} coefficient for the activated-preamplifier cases (solid lines) dips at the resonance frequency. As the matching impedance of the outer loop was increased, the corresponding S_{21} coefficient also increased. Here the solid lines are similar to those shown in Figure 3.22 which is expected. For the dashed line cases the preamplifier was deactivated which means the preamplifier was not decoupling the loops. Thus S_{21} coefficient is big at the resonance frequency. The difference in S_{21} coefficient for the cases of preamplifier and no preamplifier depends on the performance of the preamplifier (matching impedance of loop). Hence, the Z_m = 200 ohms case has the largest decoupling effect.

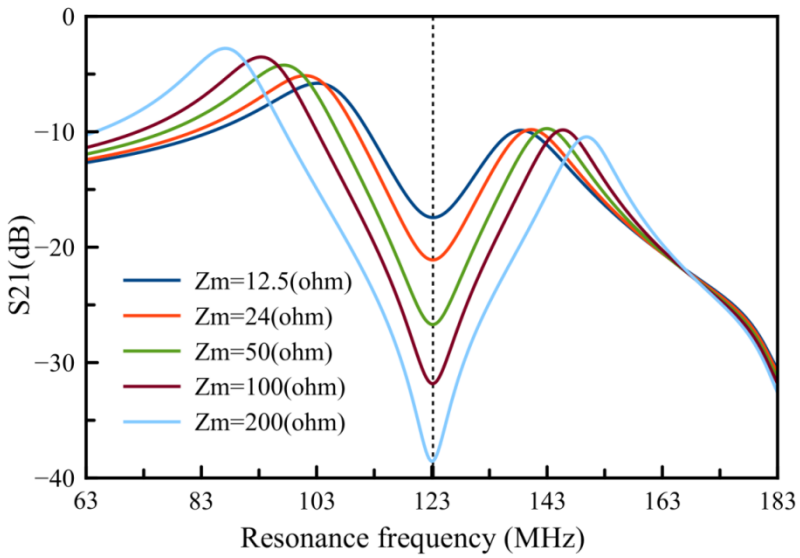

Figure 3.21 Plots showing the transmission coefficients of the inner loop plotted as a function of resonance frequency (from simulation). For all six matching impedances the preamplifier was tuned to 123.2 MHz (dashed line) while the inner loop was in isolation.

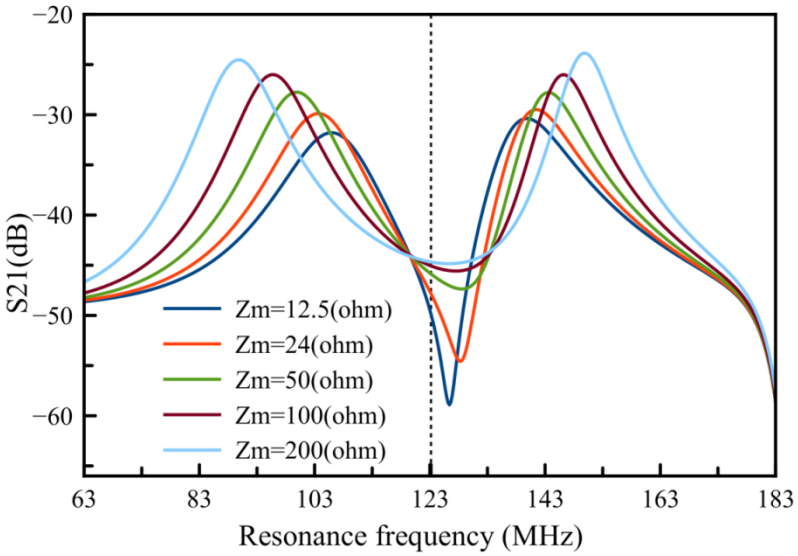

Figure 3.22 Plots showing the transmission coefficients plotted as a function of resonance frequency (from simulation). Both loops were connected to a preamplifier. The voltage source is transmitted on the inner loop and the voltage measured on the outer loop. The dip of the plot drifts away from the resonance frequency when the matching impedance was increased.

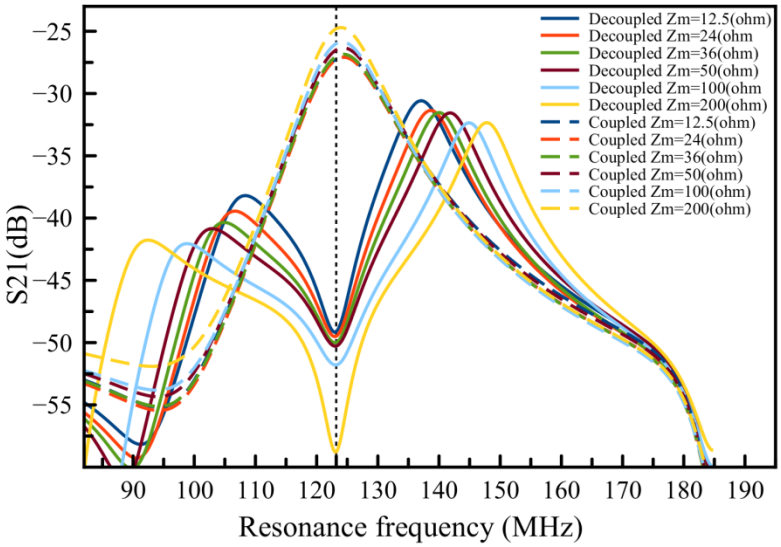

Figure 3.23 Plots showing the transmission coefficients plotted as a function of resonance frequency (from simulation). The voltage source was transmitted on the inner loop and received on the outer loop. Here the solid lines correspond to the cases where only the outer loop was connected to a preamplifier. The dashed line cases correspond to de-activated preamplifiers.

3.3.5.2 J-field simulation with and without a preamplifier circuit

The noise correlation analysis required E-field maps from the two loops. The E-field is represented by the J-field maps divided by the conductivity of the phantom. To determine if the model of the preamplifier circuit was working properly, we compared simulations of the J-field maps with and without the preamplifier circuit in place. Two sets of field maps were simulated: (1) a single-loop configuration where the outer loop was in place and no preamplifier was used (Figures 3.24 A, C, E and G); and, (2) a two-loop configuration where each loop was connected to a preamplifier (Figures 3.24 B, D, F and H). Ideally, when loops are decoupled by preamplifiers, the field maps of a two-loop simulation should be identical to a single-loop simulation. However, in Figure 3.24 it can be seen that the left-hand column of maps are obviously different from right-hand column. This is due to an asymmetry resulting from the location of the preamplifier. A perfect preamplifier will introduce a high blocking impedance in one location of the loop and cause a voltage drop at that spot. Then, the driving loop behaves as a transmitting antenna, which generates a non-uniform J-field. Here we chose an extreme case where the input impedance of the preamplifier was 0.1 ohms so that it makes the asymmetry pronounced. In addition, the field maps in the right-hand column have lower amplitude compared to the left column. This is expected because adding the high blocking impedance on the driving loop limited the current flowing in it (see Figure 3.21) and hence induced a weaker field in the phantom. To better show the fields, we rescaled Figures 3.24 E and F and show these in Figures 3.24 G and H. Here, the asymmetry is more easily visualized. This result suggests that a preamplifier circuit should not be connected to the driving loop in simulations.

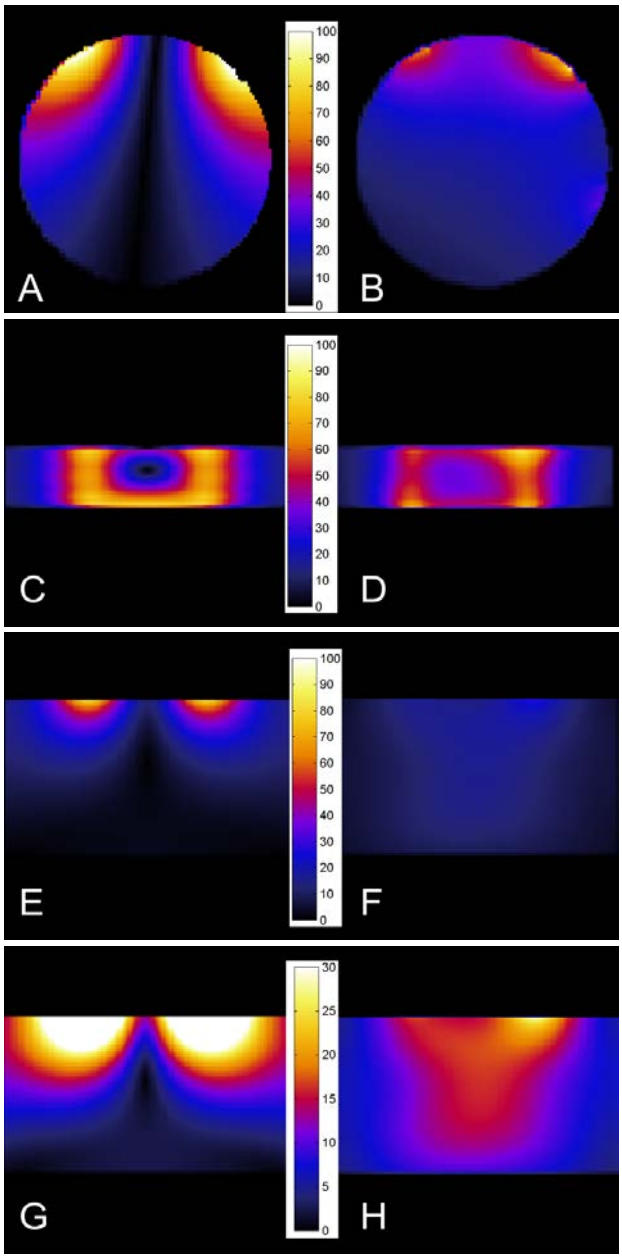

Figure 3.24 Simulated J-field maps for the outer loop obtained from within the phantom. The first row (A and B) is an axial view, the second row (C and D) is a coronal view, and third row is a sagittal view. The field maps G and H are the same as E and F but rescaled to better show the pattern of the field distribution. The left column (A, C, E and G) was simulated with only the outer loop in place and no preamplifier. The right column (B, D, F and H) had the inner and outer loop in place with a preamplifier connected to each loop. Colour bar represents the amplitude of the J-field with a unit of A/m^2.

3.3.5.3 Experimental measurement: Noise covariance

The experiment corresponding to Method (II) characterised the noise correlation coefficients and associated SNR maps when varying both loops' matching impedances. First, a single-loop experiment was conducted. The outer loop was removed from the coil and the matching impedance of the inner loop was varied to show various blocking impedances. Noise correlation analysis was applied to obtain a noise variance from each measured noise map. In addition, the noise level measured on the MR scanner console reflects the standard deviation of the sample points in a selected ROI. By taking the square of the value of the noise level, we can obtain the noise variance. To simplify comparisons, each noise variance measurement was normalized to the variance for the 200 ohms case and plotted in Figure 3.25 as a function of the loop's matching impedance (Z_m). As expected, two plots show good agreement for each value of matching impedance. For the two-loop experiment we expect to see a similar trend and this will be shown later in Figure 3.28 A.

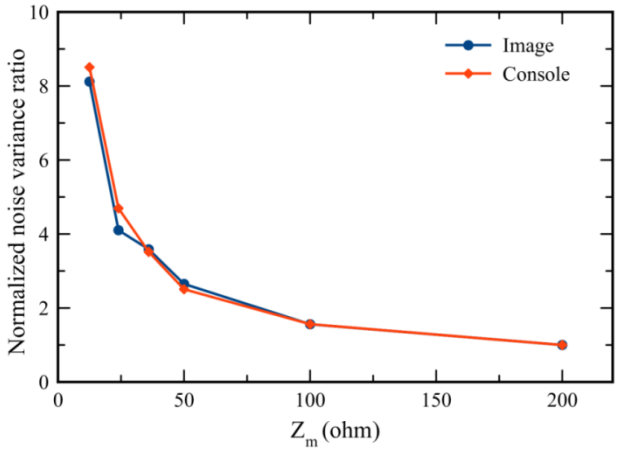

Figure 3.25 Plot showing the measured noise variance for the inner loop calculated offline and on the MR console. The values are normalized to the variance for 200 ohms and plotted as a function of matching impedance.

3.3.5.4 Experimental measurement: SNR map

Figure 3.16 showed the experimental measured results of noise correlation coefficients for the Z_m = 50 ohms case and a wide range of coil separation angles. In addition to changing the separation angle, one can vary inductive coupling by adjusting the performance of a preamplifier as shown by the simulation results in Figure 3.23. Now we experimentally evaluate the effect of using different matching impedances on SNR maps with the coil separation angle fixed to 64.5^o. Maps of a bottle phantom were obtained from the inner loop and are shown in Figure 3.26 for three matching impedances. It can be seen that the SNR is lower for regions closer to the inner loop and gradually decays as a function of distance as is expected for a surface loop. These three maps show similar field distributions but have different signal levels. This is because the high blocking impedance added to each loop causes damping of the field intensity. In order to show that preamplifier decoupling is altered by matching the loop to other values, SNR maps (normalized to the Z_m = 50 ohms case) for two extreme cases, A) Z_m = 200 ohms and B) Z_m = 12.5 ohms are shown in Figure 3.27. A region of noticeable difference is highlighted with dashed circles and this corresponds to the position of the outer loop. This difference is more noticeable in the Z_m = 12.5 ohms case. In addition, for the Z_m = 200 ohms case, the overall ratio is less than 1, which means there was less current flow than for the Z_m = 50 ohms case. Both of these observations might be due to the preamplifier having a noise figure optimized for 50 ohms, and poor noise figure for Z_m = 200 ohms case.

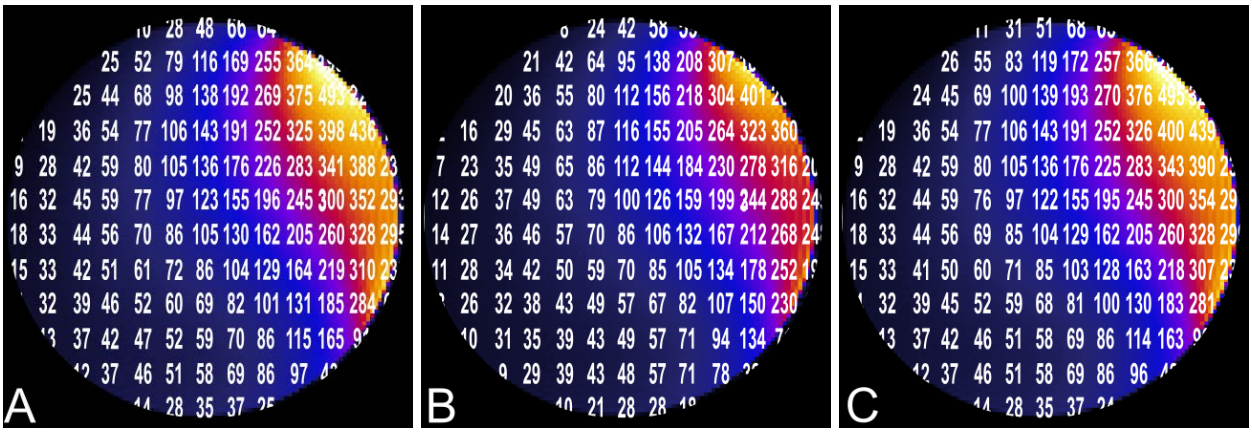

Figure 3.26 Single channel SNR maps for the inner loop obtained from images of a bottle phantom using matching impedances of (A) 50 ohms, (B) 200 ohms, and (C) 12.5 ohms. The inner loop is located on the right-hand side of each image.

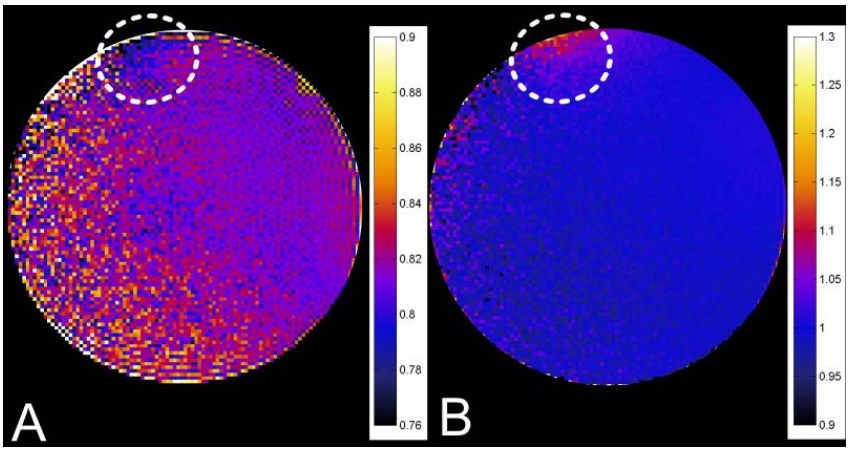

Figure 3.27 Images showing the normalized SNR maps corresponding to (A) 200 ohms, and (B) 12.5 ohms. Both were divided by the map for 50 ohms. The dashed circles indicate the region of major signal change. Note that the color scales are different for the two images.

The two-loop measurements were conducted after the single-loop experiments were done. Here the matching impedances of both loops were altered and kept the same. The noise variance, covariance, and correlation coefficients were measured at three coil separation angles, 63^{o}, 64.5^{o} and 66^{o}. The measured results are shown in Figures 3.28 and 3.29. The variance of each individual loop is given by the diagonal

terms of the noise covariance matrix. It can be seen (Figure 3.28 A) that the variance for each matching impedance has the same degree of change for all separation angles. The noise covariance (Figure 3.28 B) shows a similar trend as the noise variance. However, the vertical offsets are due to the different degrees of inductive coupling. When we compare the normalized noise correlation coefficients (Figure 3.29), the results are not biased by the variance values. All three plots show increased normalized noise correlation coefficients as Z_m decreases. The plot of phi = 63^o shows the largest normalized noise correlation coefficient for each value of matching impedance. However, the plot of phi = 66^o shows a more slowly increasing noise correlation coefficient. We expect to see this decreasing trend of normalized noise correlation coefficients with matching impedance because this is dominated by the noise covariance.

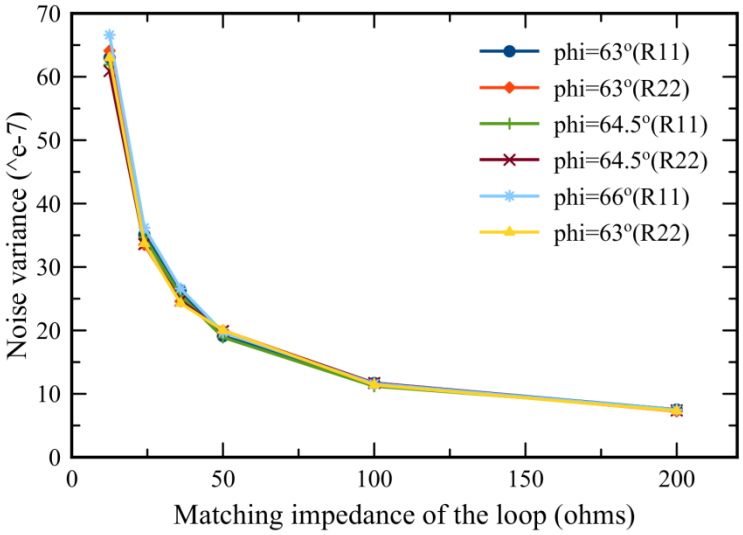

(A)

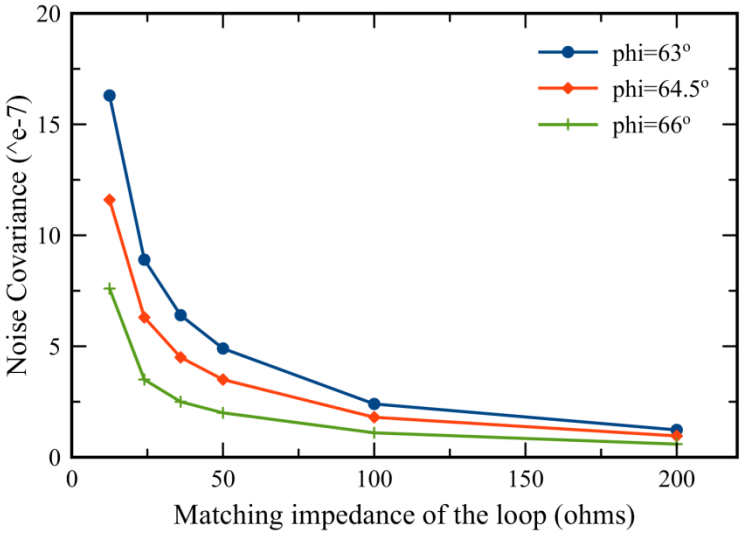

(B)

Figure 3.28 Plots showing the (A) measured noise variance for the inner loop (R11) and outer loop (R22) and (B) noise covariance for three coil separation angles plotted as a function of matching impedance of the loop.

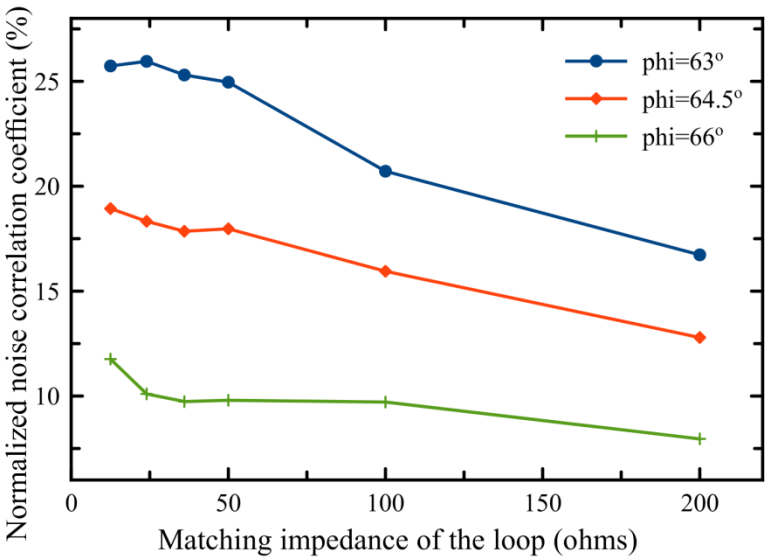

Figure 3.29 Plots showing the measured noise correlation coefficients for three coil separation angles plotted as a function of matching impedances of the loops.

3.3.5.5 Experimental measurement: Error estimation

To show the differences of the two acquisition methods for the noise maps and the measurement errors, we repeated the experiment of Method (II), but with RF on and ROI in the background. Results are shown in Figure 3.32 and these can be compared directly with Figure 3.29. It can be seen that the plots for the three coil separation angles show a similar trend for both methods. But, the data (Figure 3.30) in the range of low matching impedance values are very noisy and show an increasing trend for the plots corresponding to phi of 63^{o} and 66^{o}. The mean and standard deviation of the noise correlation coefficients was 19.1 ± 1.4 % where 1.4% is an estimated systematic error. In terms of the random error, standard deviation was 19.4 ± 2.3 % where 2.3% is an estimated random error.

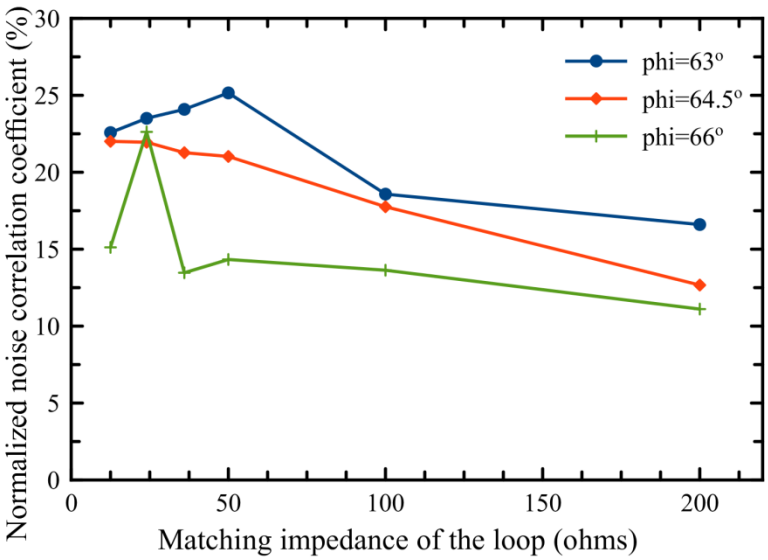

Figure 3.30 Plots showing the measured noise correlation coefficients for three coil separation angles plotted as a function of matching impedance of the loop for the experiment of varying two preamplifiers.

3.3.5.6 Comparison of simulation and experimental measurement

To compare measurements shown in Figures 3.28 and 3.29 with simulations, their corresponding simulated results of variance, covariance and normalized noise correlation coefficients as a function of matching impedance are shown in Figures 3.31 and 3.32. It can be seen that simulated variances show a similar trend to the measured plots shown in Figure 3.28. The simulated variance decays faster and covariance decays slower than the measured results, and are less distinguishable between the three coil separation angles. Hence, as we calculate the normalized noise correlation coefficients, the trend is opposite to the measured one.

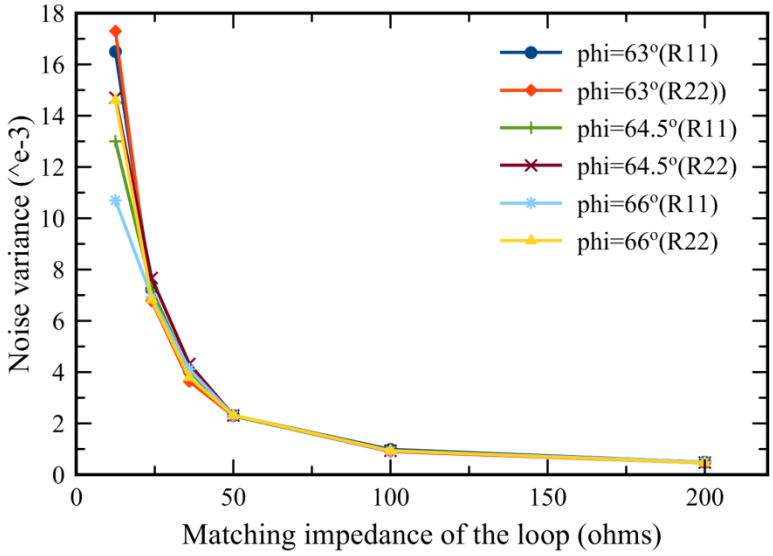

(A)

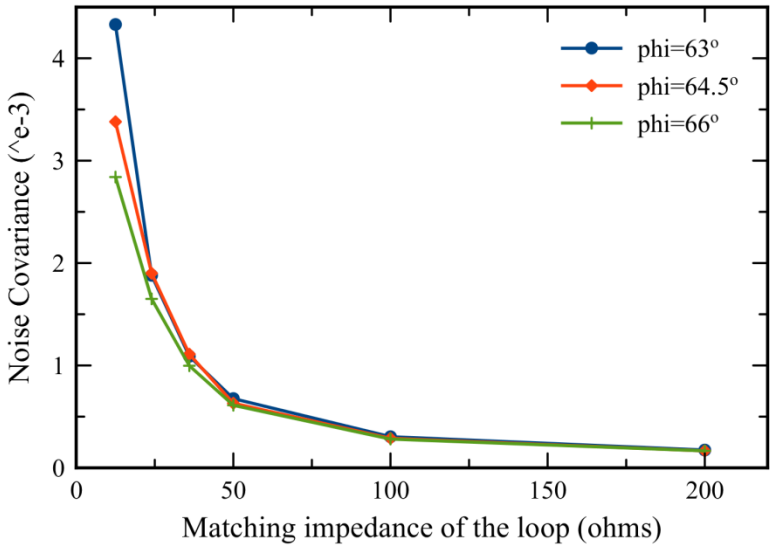

(B)

Figure 3.31 Plots showing the simulated (A) noise variance for the inner loop (R11) and outer loop (R22) and (B) noise covariance for three coil separation angles plotted as a function of matching impedance of the loop.

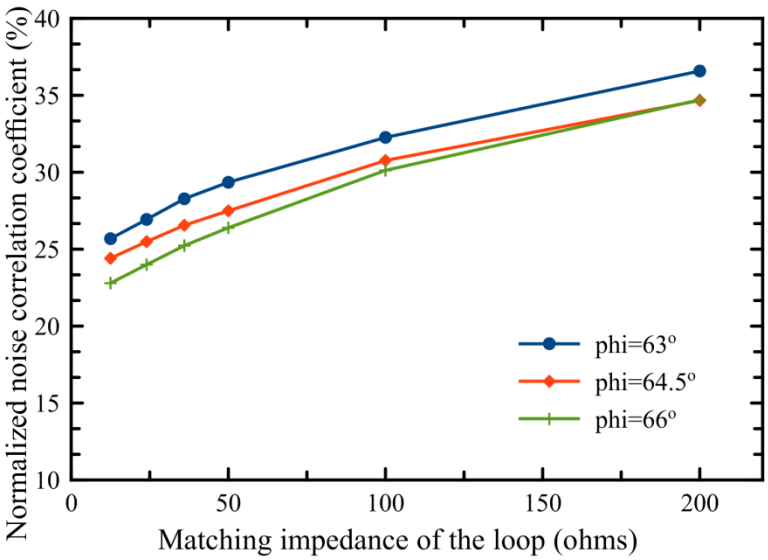

Figure 3.32 Plots showing the simulated noise correlation coefficients for three coil separation angles plotted as a function of matching impedances of the loops.

3.4 Discussion and conclusions

Techniques for verifying simulations have been described in sections 3.1 and 3.2. We have described the theory of coupling along with various decoupling methods. Our approach was to validate coil simulations by building a two-channel saddle coil array. Simulations of this coil were then compared to measurements. Based on our experience of building many other receive coils, the measurements agreed with theoretical expectations. However, only some of the simulations agreed with measurements.

3.4.1 Varying coil separation angle

We have built a two-channel saddle coil array that allowed its two loops to be rotated with respect to each other in order to vary the coupling. Using this coil we showed the effect of varying coupling on S-parameter measurements. The Q-factor plot (Figure 3.12) showed a subtle local maximum at phi = 64.5^{o}, which is the minimum inductive coupling angle. This is known as the overlap decoupling method and is

commonly used in RF coil design. The measurement of noise correlation coefficient as a function of coil separation angle is assumed to incorporate inductive coupling information. However, the local minimum observed at zero in Figure 3.16 did not agree with the measurements of S-parameter or Q-factor, i.e., the minimum was at 68^{o} instead of 64.5^{o}. This discrepancy may be due to the measurement of S-parameter only suggests the separation angle of minimum mutual inductance. However, the measured noise correlation coefficients reflect a mix effect of inductive and electric coupling. Additionally, when the inductive coupling increases, the measurements of Q-factor using 3-dB method are no longer accurate because of a double-peaked frequency response.

3.4.2 Method I: Noise correlation coefficient at small coil separation angle comparison of simulation and experiment

For comparison, we simulated the two-channel saddle coil array using the FDTD method. We characterized the coupling between the loops and the results for k_m agreed closely with measurement (Figure 3.13). The general shapes of the k_m and k_e plots also agreed with those in the literature [85], [91]. In contrast, Figure 3.18 shows a discrepancy between the simulations and measurements of the noise correlation coefficient as a function of various blocking impedances. Only the plot for 64.5^{o} has a decreasing trend common to simulation and measurement. For the coil separation angles that have strong inductive coupling, simulations and measurements strongly disagree. The preamplifier model in simulations is oversimplified and cannot decouple the loops for large inductive coupling. Hence, throughout the rest of this chapter we only compared the simulations and measurements over a small range of coil separation

angles. The results shown in Figure 3.19 cover a small range of angles and the simulations and measurements show a similar decreasing trend. However, we expected an increasing trend because the higher input impedance of the preamplifier transforms to smaller blocking impedance which means the loops should be more strongly coupled. The field maps shown in Figure 3.24 reflect the decision whether a preamplifier should be connected to the driving loop or not. The results suggest we should not add the preamplifier to the driving loop because the field maps without are more symmetric. However, the results of noise variance and covariance suggest that the preamplifier is required on the driving loop.

3.4.3 Method II: SNR map comparison of simulation and experiment

The built two-channel saddle coil was designed to evaluate simulations. We also used the coil to verify a simulation method of preamplifier decoupling. This simulation mimicked a more realistic EM field distribution by incorporating a certain amount inductive coupling into the field maps. The preamplifier decoupling transforms a high blocking impedance at the resonance frequency 123.2 MHz, hence the transmission coefficient should be a minimum at this frequency. This was predicted by the simulation (Figure 3.21) and confirmed by an S-parameter measurement. The coil was also used to measure the SNR maps for different blocking impedances (Figures 3.26 and 27). The high blocking impedance case of Z_m = 200 ohms reduced the current flowing in the loop and hence the SNR map was higher than for the Z_m = 50 ohms case. This showed that a high blocking impedance reduced inductive coupling and is preferred. However, the noise figure of the preamplifier was optimized to the Z_m = 50 ohms case, which might have reduced the SNR for the case of Z_m = 200 ohms.

3.4.4 Method II: Noise correlation coefficient at small coil separation angle comparison of simulation and experiment

Noise correlation analysis was used here because it is related to inductive and electric coupling. We expected the noise correlation coefficients to change when the inductive coupling between the loops was varied. Ideally, the behavior of the measurements and simulations would be the same. A premise of this work is that signal and noise cross-talk inductive coupling was altered by connecting a low input impedance preamplifier to each loop. Hence, we could control the amount of cross-talk by altering the performance of each preamplifier. A blocking impedance due to the preamplifier was altered using two methods: (I) varying the input impedance of the preamplifier or by (II) varying the matching impedance of the loop. For the first method, Figure 3.19 showed that the simulation and measurement had a similar trend but the values of the noise correlations coefficients differed by more than we would like. For the second method, Figures 3.29 and 3.32 show opposite trends. This is an unexpected problem and possible reasons are discussed below.

3.4.5 Error estimation of preamplifier circuit simulation: driving method

Simulating a preamplifier is very sensitive to the details of the procedure used. The first detail to consider is how to drive and tune a loop. As well as the method described in section 3.2.1 we also tried several other methods to drive the loop, e.g. an in-series current source method and a search probe method. However, it was not clear how to determine the resonance frequency for each method. Every lumped element in the simulation had a built-in sensor that recorded the voltage and current passing through it. Theoretically the resonance frequency of the loop would have been given by the peak of

the frequency spectrum of the coil's current. However, the resonance frequency recorded by each current sensor was slightly different. We observed variations in resonance frequency within one loop of 2 MHz. Because the preamplifier decoupling had to be tuned to the resonance frequency of each loop, this variation led to very large uncertainties.

3.4.6 Method II: Error estimation of preamplifier circuit simulation in tuning and matching

In section 3.2.1 a voltage source was used. A current source was tried but took a much longer time to reach steady state than using the voltage source. The other limitation of the current source was that the matching impedance of the loop could not be shown. It was important to measure the matching impedance especially for Method (II). If the loops did not match to 50 ohms in all conditions, their resulting field maps would have been hard to compare. The search probe method had the same two problems as the current source method. Hence, driving a loop using a current source method or a search probe method might have added uncertainties. Therefore, we decided to drive the loop with a voltage source in parallel with a matching capacitor and tune and match the loop according to the S-parameters recorded by the sensor located in the source. The tuning and matching procedures were done in an isolation condition (we simulated one loop at a time). We assumed the resonance frequency determined in a single-loop simulation remained the same when a coupled loop was added. This led to a second issue. It has been shown in Figure 3.22, both loops are detuned in the two-loop simulations. This led to the low blocking impedance case (Z_m = 12.5 ohms) having a better decoupling performance than the high blocking impedance case (Z_m = 200

ohms). However, this behavior is contrary to the theory of preamplifier decoupling (see Equation 3.10). If the loops are not retuned, the resulting field maps might not reflect the experiment design and might cause a wrong interpretation of the results of noise correlation analysis.

3.4.7 Method I: Error estimation of preamplifier circuit simulation

The experimental results using Method I (see Figures 3.18) showed a gradual decrease in noise correlation coefficient as the input impedance of the preamplifier was increased. This is the opposite result of what we expected. The measured noise variance and covariance (Figure 3.20) also followed the same problematic trend. The decreasing trend in variance was due to an additional circuit (a resistor in series with a preamplifier) that we designed to increase the input impedance of the preamplifier. In general, the signal received by the preamplifier was proportional to the current flowing in the loop and inversely proportional to the input impedance of the preamplifier [85], [94]. Our additional circuit was supposed to increase the signal by increasing the amount of current flowing in the loop. However, the experimental results showed the additional circuit reduced the current flowing in the loop. Hence this circuit decreased the inductive coupling between the loops, which was contrary to our experiment design. That is, we wanted to make the inductive coupling larger to observe its effect on the noise correlation coefficient. Instead, the inductive coupling was reduced by this circuit. It is likely we simplified the circuit too much, and the blocking impedance did not follow Equation 3.10. An alternative approach would be to design other preamplifiers having various input impedances and optimized noise figures. However, this is a very complicated task.

For both of the simulated and measured noise correlation coefficients shown in Figure 3.19, the values at an input impedance of 3.5 ohms corresponded to the case of where no extra resistance was added to the circuit. Here the preamplifier was not modified and corresponding data at the angle phi = 64.5^{o} should be a reference point to evaluate consistency. For example, the noise correlation coefficients of the simulation in Figure 3.19 showed a substantial deviation (~5%) from the measurement. However, the variation between the experiments is not negligible and is on the order of 10%. Hence, Roemer et al. [85] also found significant deviations between simulation and measurement.

3.4.8 Error estimation in experimental measurement

The accuracy of the measurements was compromised by the acquisition method for the noise maps (with the RF off) and other measurement errors. The method where RF power is on is less accurate than the method where the RF power is off. This finding agrees with that of Constantinides et al. [95]. The case where RF power is on is worse because the noise pixels can be contaminated by signal leaking from the sample. Other reasons why Figures 3.29 and 3.30 are different include systematic and random errors. It is important to realize that these errors are absolute values. Hence, these errors in the measurements are not negligible. This is a likely reason for some of the discrepancy, but not the difference in trend.

In summary, we built a two-channel rotating receive coil and used a model of this coil to characterize the impact of inductive coupling when estimating electric coupling. The values of k_e were calculated by using Equations 3.10 and were equivalent to the

noise correlation coefficients. However, the inductive coupling should alter the E-field distribution, the noise correlation coefficient no longer equals to k_e. But, we found that by creating a *Mode* for each loop element, the new values of k_e showed a good agreement to the measured noise correlation coefficients when inductive coupling is not too strong. The results of using preamplifier model throughout this chapter showed discrepancies between simulations and experiments of this two-channel saddle coil array. Although we have improved the simulation procedures to more accurately predict the coil, the results only partially validated the concept of including inductive coupling in the simulation. Hence, these results suggest that the simulation cannot perfectly model a real RF coil if the preamplifier model is overly simplified. In spite of this, the simulation was able to roughly characterize the performance of the coil and consequently it is useful in the initial phase of a design process.

Chapter 4: Improvement of transmit SENSE RF pulse design for small FOV excitation

Due to an under-sampled k-space for transmit SENSE RF pulse design, excitation artifacts can appear outside of the region-of-interest (ROI) which would degrade the image quality. In Chapter 4, we propose a novel RF pulse design method that reduces excitation artifacts. We illustrate and adapt the concept of negative excitation in the workflow of RF design for small field-of-view (FOV) excitation. The proposed method was tested with two different phantoms. Through the improvement of the RF pulse design, we expect the small FOV applications will have better image quality.

4.1 Introduction

Using a well-designed RF pulse, one can excite a smaller region e.g. cylinder or rectangular box, inside a patient. This is known as small FOV RF pulse design. In general, the length of the RF pulse needed to excite a multidimensional region with a typical MR scanner is too long (~20 ms) and inefficient for routine clinical imaging. Transmit SENSE (Tx-SENSE) is a technique used to shorten the RF pulse. A major concern when using Tx-SENSE during multidimensional excitation is the production of local SAR hot spots associated with excitation artifacts. These excitation artifacts are related to the asymmetry of B_1^+ field maps of individual coil elements. In Chapter 5 we show these artifacts can be reduced by optimizing the transmit-array coil design. These excitation artifacts also depend on the RF pulse design strategy. Hence the excitation artifacts may be minimized with a better RF pulse design method.

In this chapter we developed a method to minimize excitation artifacts with the aim of improving Tx-SENSE performance. Our method optimizes RF pulse design by iteratively using Bloch-simulations to update the design.

4.1.1 Hypothesis

Our hypothesis is; when the Bloch simulation predicts the calculated RF pulse will generate excitation artifacts, we can design a *negative* excitation pattern containing the same artifacts, and thus cancel the artifacts.

To reduce the excitation artifacts, we propose a method based on Bloch-simulations. The workflow of our proposed method is shown in Figure 4.1. Starting from a RF pulse design method, i.e. a conjugate-gradient method in our case, we determined the first set of RF pulses for the desired target pattern. Then, we used a Bloch simulation to estimate the resulting excitation pattern of the initial RF pulses. We subtracted the resulting pattern from the designed pattern to find a residual pattern, which was a complex matrix. The root-mean square error of the residual was calculated to determine if this error reached a stopping criteria. If not, in the next iteration, we took the negative of the residual pattern and combined it with the original target pattern to form a new target pattern. The updated RF pulses were calculated and used in the next Bloch simulation. The iteration repeated until the root-mean square error of the residual pattern was small enough to reach the stopping criteria. A range of stopping criteria values was tested and the one which gave a minimum Euclidean norm of the residual was picked.

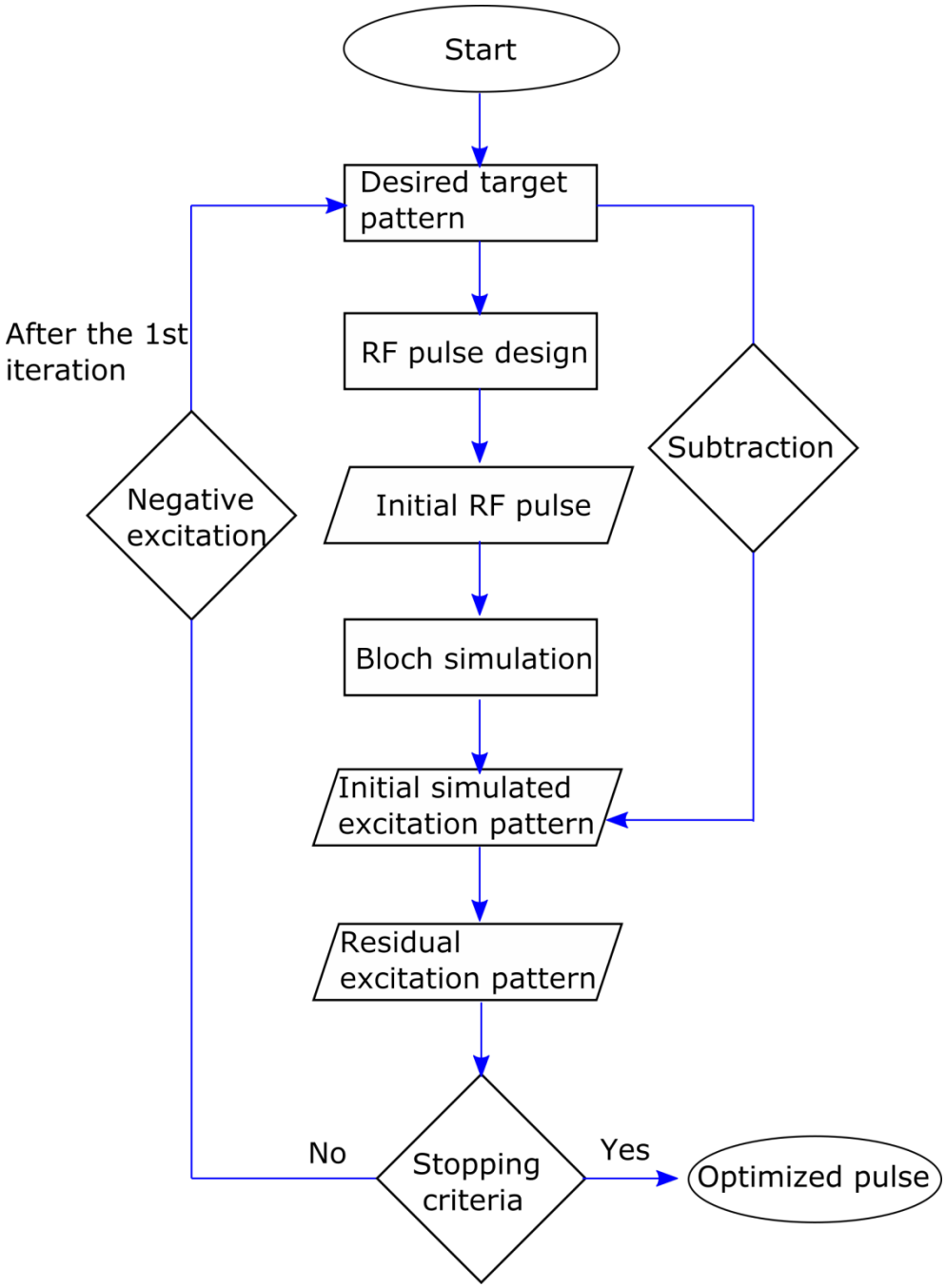

Figure 4.1 Diagram showing the workflow of optimizing RF pulses by using Bloch simulations in the iterative manner.

4.1.2 RF pulse design theory of transmit SENSE

Tx-SENSE allows shorter transmit pulses in an analogous manner to which SENSE enables faster receive sequences [89], [96], [97]. In signal reception, coil elements will

simultaneously obtain a spatially encoded portion of information. A priori knowledge of the sensitivity profile (B_1^+ map) for each coil element is used to reconstruct a full FOV image from a set of aliased images acquired from under-sampled k-space data. In a parallel transmission, the RF pulse duration is reduced by shortening the k-space trajectory. The sparse k-space trajectory corresponds to an aliased excitation pattern. With spatially inhomogeneous B_1^+ sensitivity maps and a specific RF waveform on each transmit element, Tx-SENSE in the spatial domain decomposes the two-dimensional excitation pattern into several smaller regions mainly excited by the nearest elements of a transmit array. In other words, the Tx-SENSE approach excites less of k-space. Thus, it breaks a long RF pulse into several short sub-pulses, each on its own channel. This generates an arbitrary excitation pattern by superimposing individual small excitation regions.

There are several methods used to design RF pulses for multidimensional excitation. To solve for the initial RF pulse we used a method proposed by Grissom et al. [45]. This method provided good flexibility for choosing both a k-space trajectory and a desired target pattern in the spatial domain. In the small-tip angle regime, the transverse magnetization after multichannel excitation was the summation of individual excitation patterns, which were weighted by their corresponding transmit sensitivity maps. The transverse magnetization was expressed as

$$m(\vec{x}) = i\gamma m_0 \sum_{r=1}^{R} S_r(\vec{x}) \int_0^T b_r(t) e^{i\vec{x}\cdot\vec{k}(t)} dt \qquad (4.1)$$

where

m: transverse magnetization after excitation

γ: gyromagnetic ratio

m_0: magnitude of equilibrium magnetization

S: complex transmit sensitivity map of each channel

b: RF waveform for the r-th channel

x: spatial position

k: excitation k-space trajectory

R: number of transmit channels

T: length of RF pulse

In order to calculate the RF pulses, we first discretize Equation 4.1 in both time and space and rewrite it as

$$\begin{aligned} m(\vec{x}_p) &= i\gamma m_0 \sum_{r=1}^{R} S_r(\vec{x}_p) \sum_{q}^{Q} b_r(q\Delta t) e^{i\vec{x}_p \cdot \vec{k}(q\Delta t)} \Delta t \\ &= \sum_{r=1}^{R} S_r(\vec{x}_p) \sum_{q}^{Q} [i\gamma m_0 e^{i\vec{x}_p \cdot \vec{k}(q\Delta t)} \Delta t][b_r(q\Delta t)] \end{aligned} \tag{4.2}$$

where X_p is a spatial grid indexed with p (p = 1, 2, … , P), and Δt is a sampling time interval indexed with q (q = 1, 2, … , Q). Then, we express Equation 4.2 in matrix form

$$\begin{aligned} [M] &= \sum_{r=1}^{R} [S_r][A][b_r] \\ &= [\mathrm{diag}(S_1) \cdot A \,|\, \mathrm{diag}(S_2) \cdot A \,|\, \ldots \,|\, \mathrm{diag}(S_R) \cdot A] \begin{bmatrix} b_1 \\ b_2 \\ \vdots \\ b_R \end{bmatrix} \\ &= [A_{full}][b_{full}] \end{aligned} \tag{4.3}$$

Here [M] is a P-by-1 vector of discretized spatial points; [S] is a P-by-P diagonal matrix of individual transmit sensitivity map. [A] is a P-by-Q matrix where each element, $a_{pq} = i\gamma m_0 e^{i\vec{x}_p \cdot \vec{k}(q\Delta t)} \Delta t$. $[b_r]$ is a Q-by-1 vector of discretized time points of RF waveform for an individual channel. Hence, calculating the RF pulses that excite the design target pattern becomes a regularized least-square problem expressed, $[M] = [A_{full}][b_{full}]$, as follows

$$\hat{b}_{full} = \text{argmin}_{b_{full}} \left\{ || A_{full} b_{full} - m_{des} ||_w^2 + R(b_{full}) \right\} \quad (4.4)$$

where

A_{full}: system of linear equations

b_{full}: optimal RF pulse

m_{des}: desired target pattern

$R(b_{full})$: Tikhonov regularization term

w: spatial weighting matrix

Equation 4.4 can be solved via direct methods, e.g. brute force matrix inversion, which is straight forward to implement. The Tikhonov regularization term, $R(b_{full}) = \lambda b_{full}' b_{full}$, may be used to control the RF Power. However, if Equation 4.3 has a large number of variables, A_{full} becomes a large and sparse matrix. Using matrix inversion methods to solve a problem containing a sparse matrix requires extensive computing since the computation of A_{full}^{-1} takes a lot of memory. Hence, in some cases the exact solution might not be found, even when using a high performance computer. An iterative-based conjugate gradient method is another common way to solve least-square problems. This method is more efficient than the matrix inversion method. Our proposed method, illustrated in Figure 4.1, has an improvement based on the conjugate gradient method, i.e. negative excitation.

In principle, to evaluate the resulting excitation pattern of the calculated RF pulses, we could take the Fourier transform of the RF pulse of each channel. This would give the transverse magnetization of each channel for a small-tip angle regime. The total excitation pattern is the summation of excitation patterns from the individual channels. Theoretically, the result of this Fourier transform approach is the desired target pattern. It is important to note that the Fourier transform approach is an idealised case and omits

some physics. A Bloch simulation is more comprehensive and we used this to estimate the resulting excitation pattern. According to our experience, the measured images are always worse than the result predicted by the Fourier transform approach, and show different degrees of excitation artifacts which appear outside the desired target pattern. However, the measured images are similar to the prediction of a Bloch simulation. Hence, we used Bloch simulations instead of a Fourier transform approach to improve the algorithm for RF design.

4.2 Material and methods

4.2.1 RF coil simulation

To verify if our proposed method was affected by the coil configuration, we simulated two eight-channel transmit array coils for comparison. These coils were modeled in a finite difference time-domain (FDTD)-based electromagnetic (EM) software (SEMCAD X v14.8, SPEAG, Zurich, Switzerland). We first simulated a symmetric RF coil shown in Figure 4.2, which is used to represent a head coil. A uniform cylindrical phantom with a diameter of 20 cm and a length of 30 cm was inside the simulated coil. This phantom was based on a commercially-supplied phantom (bottle 1.9 liters Siemens) that we often use for quality control. Its conductivity was 0.97 S/m and its relative permittivity was 82.12. This head coil consisted of eight 4 cm-by-10 cm coil elements that were azimuthally distributed at 45^{o} increments around the phantom. Four capacitors (30 pF) were used in each coil element to tune the element to 123.2 MHz.

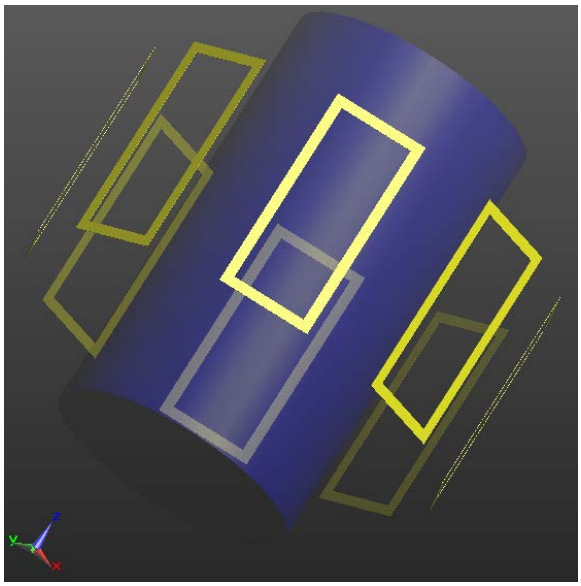

Figure 4.2 Diagram showing the eight-channel transmit array coil used in the simulations to represent a head coil.

For RF pulse design, we require knowledge of the individual transmit sensitivity maps for each element of the eight-channel transmit array. These B_1^+ field maps were simulated and are shown in Figure 4.3. As expected, it can be seen that the magnitude of each sensitivity map decays for locations far away from the coil element.

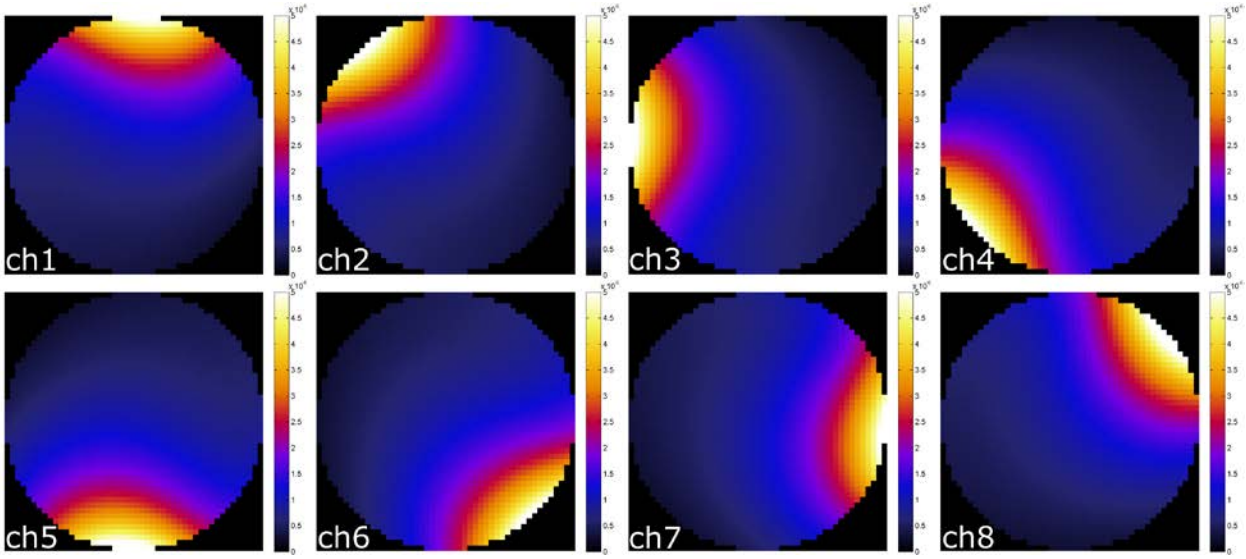

Figure 4.3 Images showing the individual B_1^+ field maps from an eight-channel transmit array. Colour bar represents the amplitude of the B_1^+ field with a unit of Tesla.

Most MR scanners are equipped with one RF transmission channel. In this case, a birdcage volume coil is the most commonly used transmit coil. Depending on the design of the birdcage coil, several resonance modes can be formed. However, only one (homogenous) mode is used to transmit RF pulses. This mode is a circular polarized transmit field which has a very homogenous field at the iso-center of the main magnet. To compare the performance of multi-channel excitation with single-channel excitation, we applied Eigen-mode analysis to the eight-channel transmit array to form the homogenous mode. This allowed us to mimic the homogenous mode of a birdcage coil that used a single excitation channel. Eight Eigen-mode fields were created by using the equation expressed as

$$\hat{S} = \sum_{r=1}^{r=8} S_r e^{im(r-1)\pi/4} \tag{4.5}$$

and varying m. Here S is a transmit sensitivity map from each coil element (shown in Figure 4.3), r is the number of the coil element and m is the quadrature and anti-quadrature birdcage resonance mode. Each Eigen-mode has an incremental phase of $m\pi/4$ delivered to each coil element. The total azimuthal phase variation is $m2\pi$. The transmit fields of eight Eigen-modes are shown in Figure 4.4. Here the m = +1 mode represents the homogenous mode of a birdcage coil.

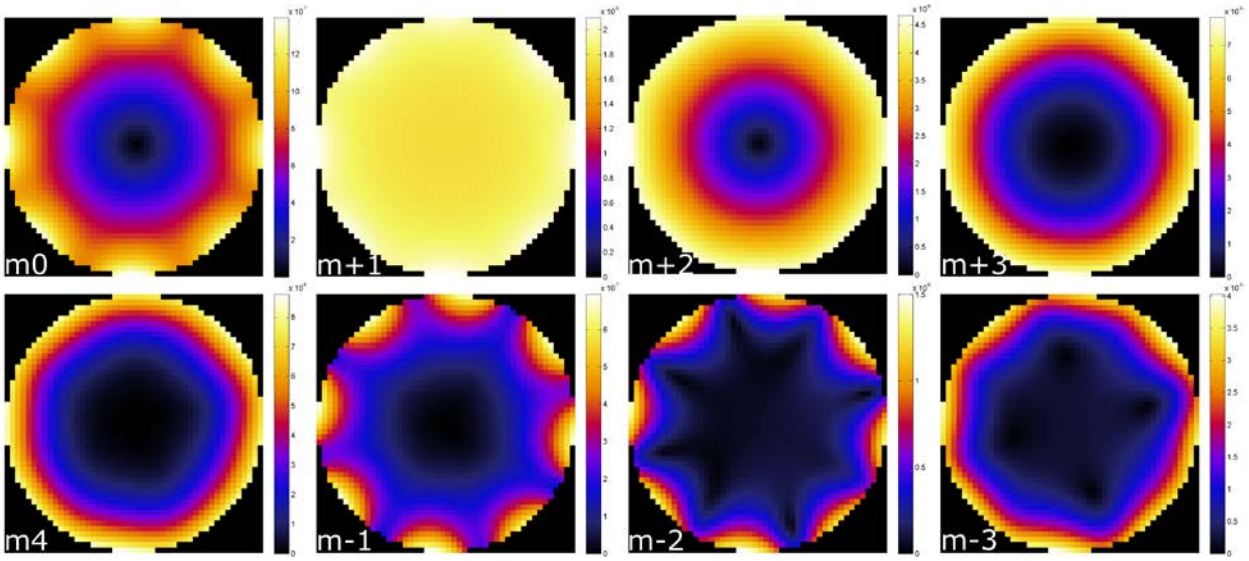

Figure 4.4 Images showing the B_1^+ field maps for eight Eigen-modes (quadrature and anti-quadrature modes) of the eight-channel transmit coil. Each Eigen-mode is labeled in the bottom left of each image. These maps were constructed using the individual fields shown in Figure 4.5. Mode m=+1 is the standard transmit field used in MR scanners.

To examine if the RF pulse design method would be affected by the configuration of the RF coil, we also simulated the planar coil design shown in Figure 4.5. Note that this is the same coil configuration that will be evaluated in Chapter 5, see Figure 5.2 B. This transmit array coil comprises seven hexagonal coil elements (length of each side is 12 cm) in the anterior section and one polygonal coil element in the posterior section. For this planar coil, we simulated an anthropomorphic phantom called “Ella”, which is from the Virtual Family Human Model [98]. These human models include the organs inside a human body along with their respective EM properties. The EM interactions between the transmit fields and the phantom are complicated. Additionally, in the planar coil configuration each coil element is a surface coil where the penetration depth of the EM field depends on the size of the coil element. Hence, we expected that the EM field

distribution inside the phantom would be heterogeneous and asymmetric compared with the head coil.

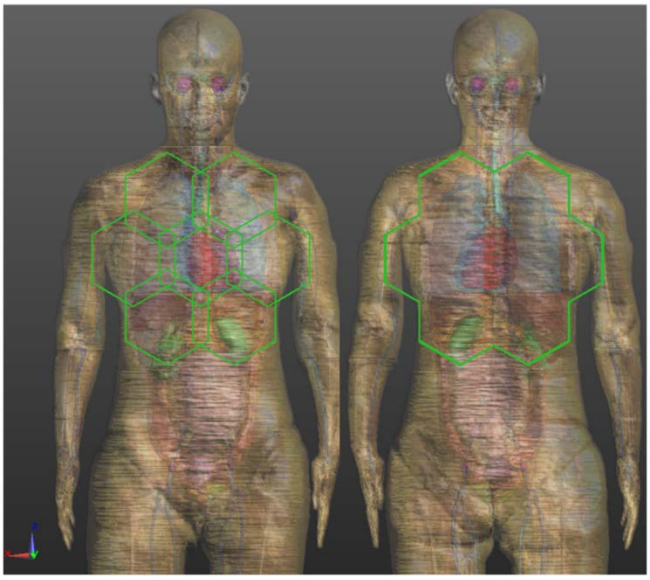

Figure 4.5 Diagram showing the planar model of the eight-channel transmit array coil used in the simulations. The EM field distribution inside the phantom is more asymmetric but concentrated close to the torso surface.

4.2.2 RF pulse design

To determine the RF pulse for the desired target pattern, we implemented Equation 4.4 within the RF coil design software (Musaik Tx-array Beta version, ZMT, Zurich, Switzerland). Our proposed algorithm consisted of several plugins for this software. The first plugin was for designing a multi-region target pattern, which was optionally smoothed with a Gaussian filter. The second plugin was an implementation of a conjugate gradient algorithm for solving the least-squares problem of Equation 4.4. The Bloch simulator was embedded in the plugin along with the conjugate gradient algorithm to predict the resulting excitation. A new desired target pattern was updated

automatically in iteration. In addition, to reduce excitation artifacts, we constructed a spatial weighting matrix to give a higher priority to regions outside the excitation pattern.

For reference, the GUI of Musaik: Tx-array is shown in Figure 4.6. In this software, we can design arbitrary target patterns and chose a variety of k-space trajectories, e.g. variable density trajectory, and use different algorithms to calculate the RF pulses. The resulting excitation pattern can be displayed as a Fourier transform approximation or a Bloch simulation. As an example, we designed an “MR”-shaped logo as a target pattern and transmit the RF pulses with two Eigen-mode channels, m = ±1 modes. Here the corresponding k-space trajectory, gradient waveforms and calculated RF pulses are shown in Figure 4.7. This software provided flexibility by allowing the user to use their own k-space trajectories and solvers in the Tx-SENSE algorithm, which was very useful.

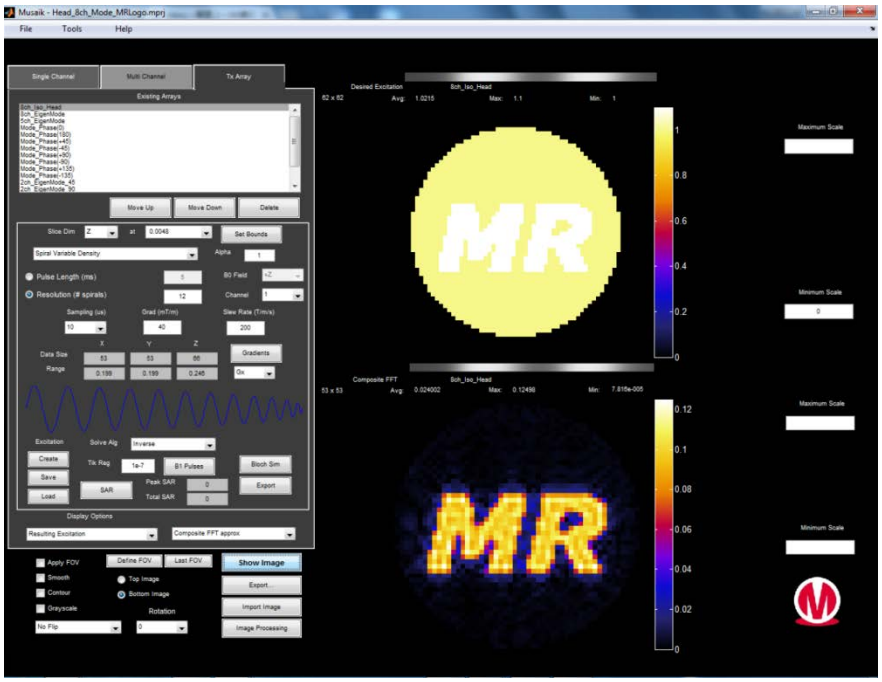

Figure 4.6 Image showing the graphical user interface (GUI) of Musaik for RF pulse design.

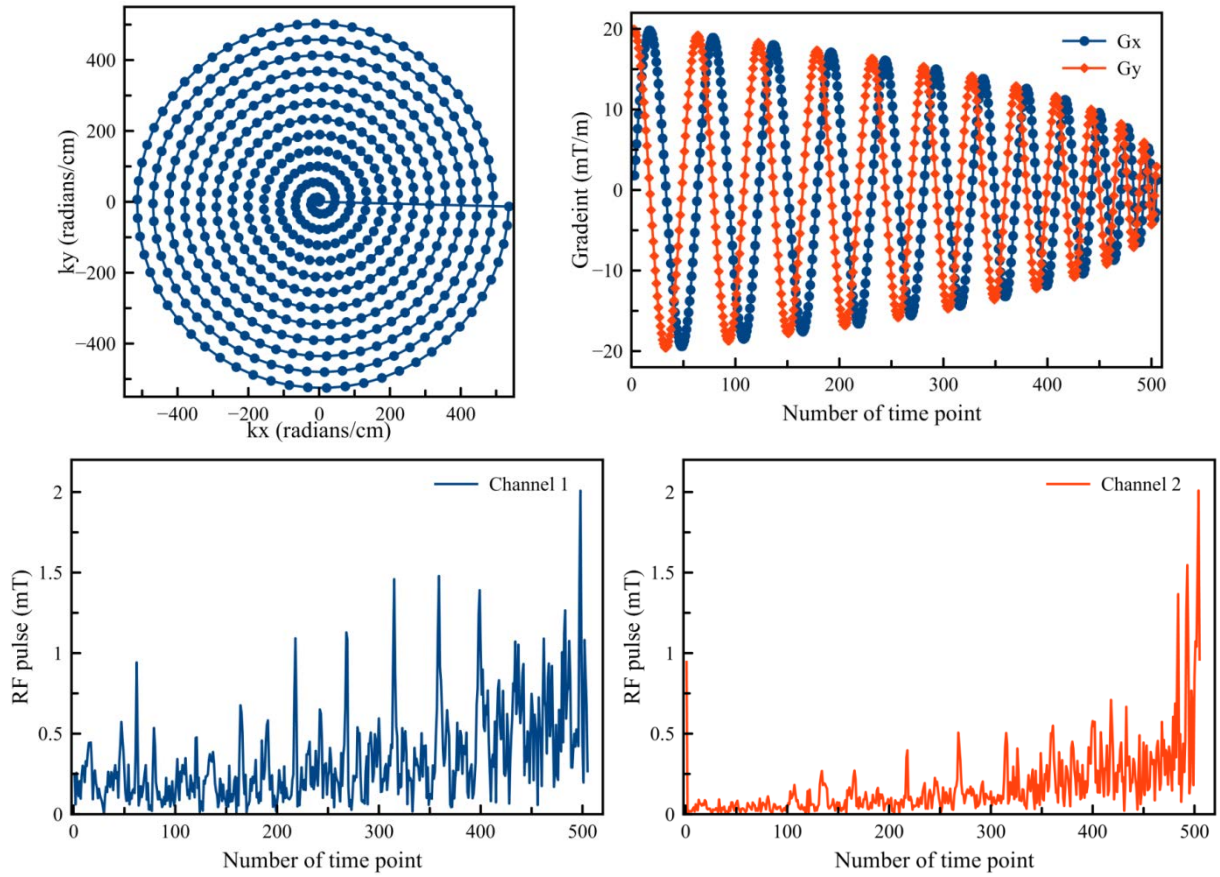

Figure 4.7 Plots showing (top-left) an example of k-space trajectory, (top-right) gradient waveforms, and (bottom) RF pulses to excite a target pattern of “MR”: using two transmit channels.

To determine how the proposed method could reduce excitation artifacts, we compared simulation results of the proposed method (minimizing excitation artifacts outside the target pattern) with a benchmark result for two coil configurations. For the benchmark, we choose the RF pulses calculated in the first iteration of the proposed method. This is how a RF pulse would normally be calculated, i.e. without using our proposed method. The parameters used in the RF pulse calculations follow. For the symmetric coil configuration (see Figure 4.2), FOV = 12.3 cm x 12.3 cm and object matrix size = 50 x 50. For the planar coil configuration (see Figure 4.5), FOV = 52 cm x 20.9 cm and object matrix size = 174 x 71.

Spiral k-space trajectory is a fast and relatively common imaging technique. The length of a RF pulse is related to the number of spiral turns of the k-space trajectory. Here all RF pulses were designed using a variable density trajectory. To show how the excitation accuracy was affected by the length of RF pulse, we designed spiral k-space trajectories with various lengths of RF pulses for the symmetric configuration (see Table 4.1). A fully Nyquist-sampled k-space would require 25 spiral turns and a corresponding pulse length of 19.3 ms. However, to speed excitation we used a variable density k-space trajectory, which had less sampling points in the high frequency region. RF pulses with different length were applied for various purposes. As an example, the shortest pulse length was used for testing the limits of the proposed method. The RF pulse length was reduced by about one-half, corresponding to a 12-turn k-space trajectory and was further reduced until the pulse length was about 1 ms. The length of RF pulse that we designed for the planar configuration was 1.3 ms, which also corresponded to a 6-turn spiral k-space trajectory.

The design of the gradient waveform and k-space trajectory was limited by the MR scanner's gradient performance. Hence the following parameters used for RF pulse calculation are fixed: sampling time interval (Δt) = 5 μs, maximum gradient amplitude = 40 mT/m and slew rate = 200 T/m/s. The two target patterns used were shown in Figure 4.8. The MR logo was chosen to demonstrate the performance of the multi-channel excitation for an arbitrary target pattern. A more realistic target pattern (i.e. two rectangles) is shown within the Ella phantom in Figure 4.8 B. This target pattern mimics the scenario of exciting small regions in the breasts. The desired transverse

magnetization corresponded to a flip angle of 5.7^{o} in the excitation pattern, and thus the small-tip angle regime was sustained.

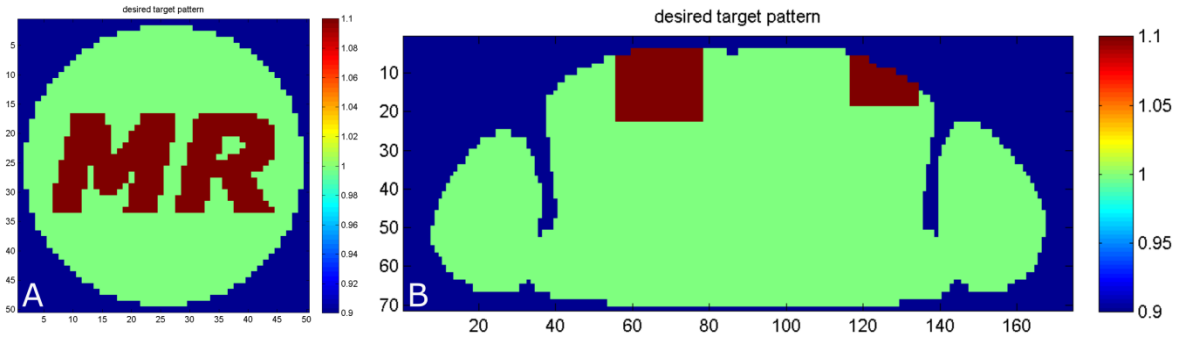

Figure 4.8 diagrams showing desired target patterns on the two phantoms for (A) symmetrical and (B) planar configurations. The colour bar indicates the normalized magnetization.

Table 4.1 Number of spiral turns of k-space trajectory and corresponding RF pulse length for the symmetric coil configuration.

Number of spiral turns	25	12	8	6	4
RF pulse length (ms)	19.3	6.4	3.5	2.3	1.2

4.3 Results

In general, the performance of multi-channel excitation should be better than single channel excitation. To demonstrate this we started by calculating two RF pulses for single-channel excitation. These two RF pulses corresponded to Eigen-mode channels, m = ± 1 (Figure 4.4), which were the circular polarized (homogenous mode) and anti-circular polarized (CP) mode. Using Fourier transforms of the calculated RF pulses, the resulting excitations, i.e. transverse magnetizations, were generated. The amplitude maps of the resulting excitations are shown in Figures 4.9 A and B. For both excitations, significant artifacts are observed. This is an anticipated result. Moreover, in the anti-circular polarized mode (Figure 4.9 B), the designed RF pulses cannot properly excite

the pattern in the central region. This is because the transverse magnetization is weighted by a transmit sensitivity map, which has extremely low sensitivity in this region (see Figure 4.4, m = -1). From the phase maps shown in Figures 4.9 C and D, it can be seen that the phase values in the desired target pattern are mostly zero and the excitation artifacts have non-zero phase values, which is an expected result.

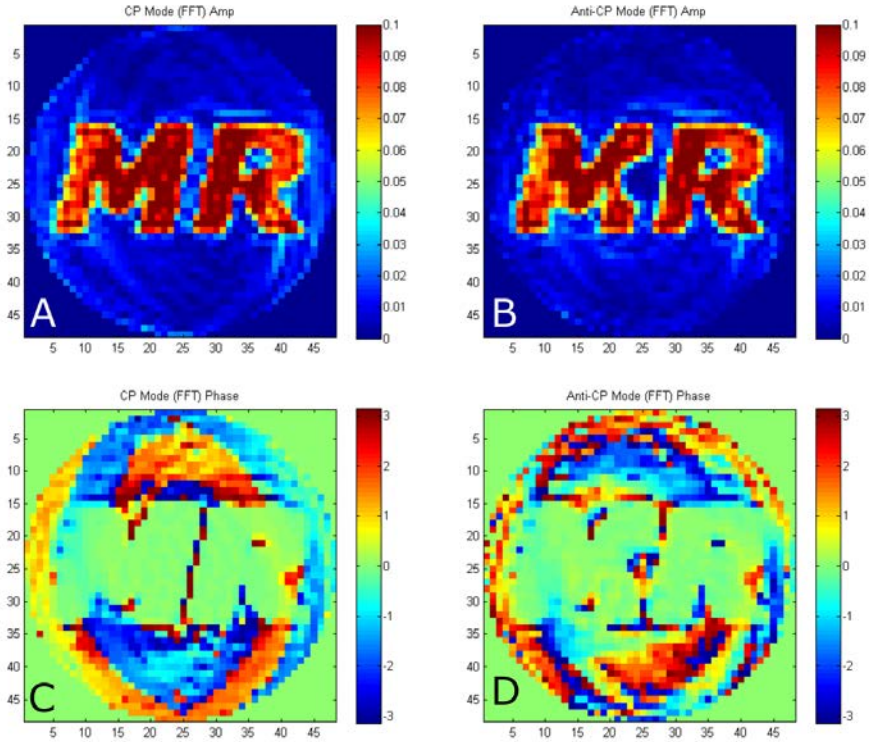

Figure 4.9 Images showing the excitation and phase maps generated using the Fourier transform approximation. The results are for a single channel of either circular polarized mode (A and C) or anti-circular polarized mode (B and D). The RF pulse length corresponds to a 12-turn k-space trajectory. For (A) and (B) the colour bar indicates the normalized magnetization. For (C) and (D) the colour bar indicates the phase in radians.

We have shown using single-channel excitation would generate obvious excitation artifacts. To demonstrate the advantage of using multi-channel excitation, we simultaneously transmitted two RF pulses to generate the MR logo. For this

transmission, we used the both CP and anti-CP (m = ± 1) modes of the Eigen-mode channels. Here the resulting excitations were found using the Fourier transform approximation. The amplitude maps of both channels and their composite (i.e. their summation) are shown in Figures 4.10 A to C. It can be seen that the anti-CP mode channel (Figure 4.10 A) only generated excitation artifacts. In contrast, the CP mode channel (Figure 4.10 B) excited the desired target pattern. However, the CP mode channel also generated identical excitation artifacts as the anti-CP mode. When we combined the two channels (Figure 4.10 C), most of the excitation artifacts were canceled and only the desired target pattern remained. The composite phase map (Figure 4.10 F) is in-phase in the target region and has a random phase distribution outside the target pattern. However, the phase difference (Figure 4.10 G) between the two channels is 180^{o} out of phase in the region where both channels generated identical excitation artifacts. This is evidence that with our proposed method we can design a negative excitation to pre-compensate the artifacts. In this case, we can see that only channel 2 excites the target pattern, but channel 1 only generates artifacts. Therefore, by shifting the phase of the artifact patterns by 180^{o}, we can remove the artifacts and not alter the original target pattern.

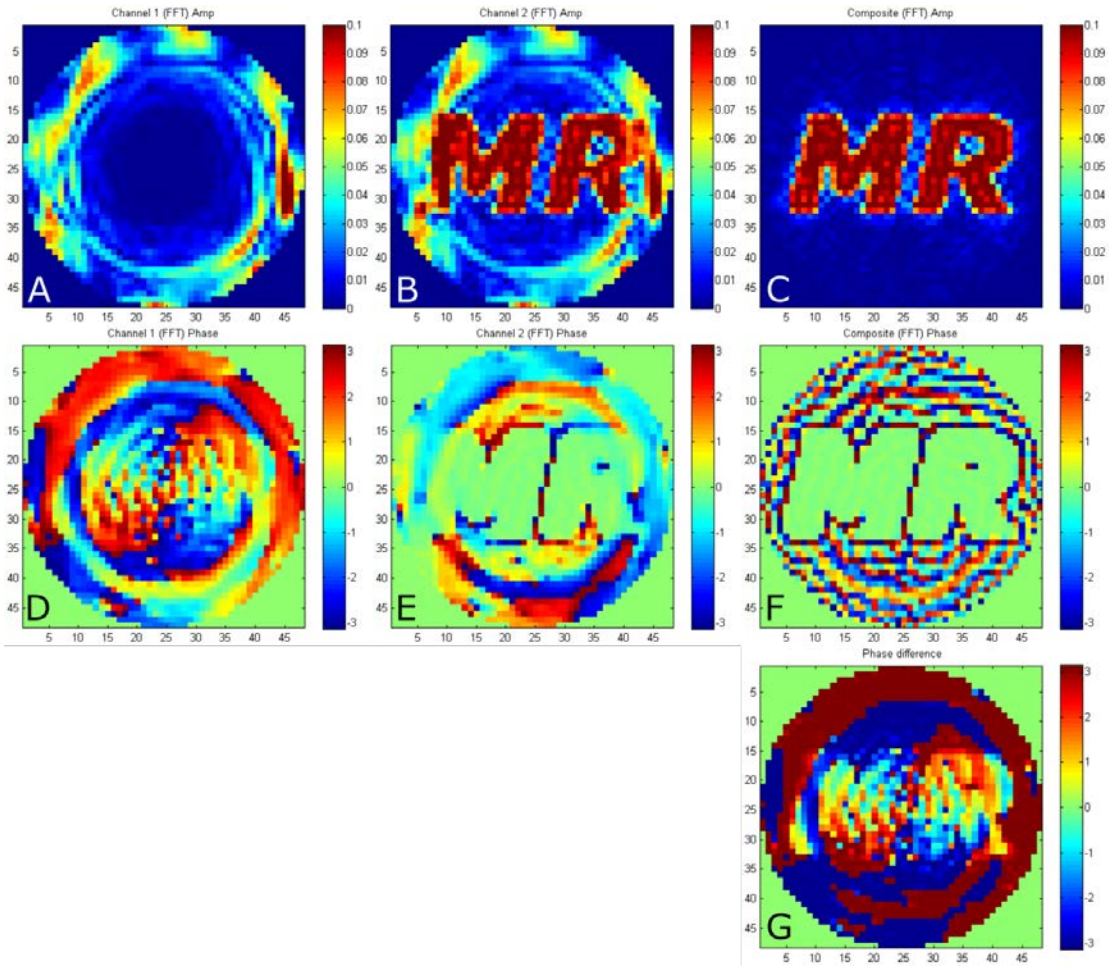

Figure 4.10 Images showing the excitation and phase maps generated using the Fourier transform approximation. The results are for two-channel excitation with a CP mode channel and an anti-CP mode channel. The first row shows the amplitude of the excitation for (A and B) individual channel results and the (C) composite result. The second row shows the phase maps corresponding to A to C. The third row (G) is the phase difference between (D) and (E). The RF pulse length corresponded to a 12-turn k-space trajectory. For (A) to (C) the colour bar indicates the normalized magnetization. For (D) to (G) the colour bar indicates the phase in radians.

To illustrate the differences between a Fourier transform approximation and a Bloch simulation, the corresponding excitations are shown in Figure 4.11. For both methods, identical RF pulses were used to excite a MR-shape logo with the eight-channel head coil. It can be seen that the resulting excitations of the target pattern show agreement

between both methods. However, the Bloch simulation showed there will be some strip-like excitation artifacts and its corresponding phase map has a similar pattern alternating by 180^{o}. In contrast, the Fourier transform approximation showed less artifacts and the phase outside the target pattern region appears more as background noise. The Fourier transform approximation has an advantage of easy implementation. However, it is a simple theoretical approach and does not show artifacts (i.e. susceptibility artifact) due to the magnetic field inhomogeneity. Hence, this method is useful when a theoretical result is interesting and excitation artifacts are not a concern. Therefore, when comparing the excitation of arbitrary RF pulses, the result can be affected by the choice of method. From our experience, a Bloch simulation provides a better prediction of an excitation than a Fourier transform approximation. Hence, we incorporated the results of Bloch simulations into the proposed method.

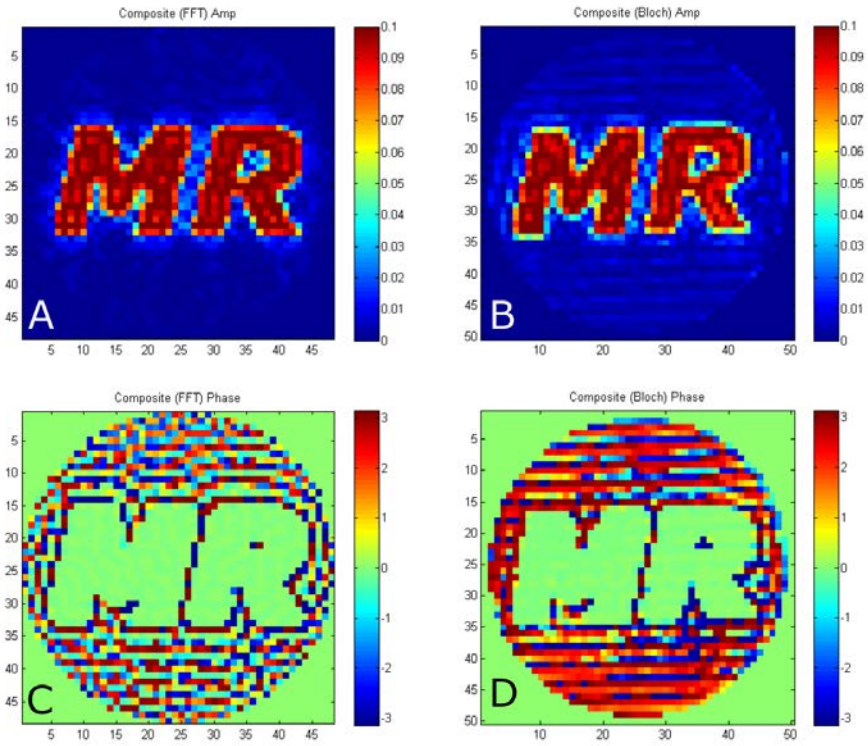

Figure 4.11 Images showing excitations and phase maps using a Fourier transform approximation (A and C) and a Bloch simulation (B and D). The excitation was generated using the eight-channel transmit coil array shown in Figure 4.2. The RF pulse length corresponded to a 12-turn k-space trajectory. For (A) and (B) the colour bar indicates the normalized magnetization. For (C) and (D) the colour bar indicates the phase in radians.

The initial RF pulses in the proposed method (see Figure 4.1) had to be carefully chosen, otherwise any comparison between the optimized RF pulses and the initial RF pulses could be biased. Recall that the initial pulse is designed with a conjugate gradient (CG) algorithm. This algorithm makes use of a user-chosen error tolerance (ε). This tolerance is a stopping criteria, which is the Euclidean norm of the residual used to terminate the conjugate gradient algorithm. We first evaluated the effect of using different values of the error tolerance in the conjugate gradient algorithm. The resulting excitations with various error tolerance values are shown Figure 4.12. It can be seen

that the excitation is significantly affected by the choice of error tolerance. In the case of using a very small error tolerance of $1e^{-9}$ (shown in Figure 4.12 A), the algorithm could not determine a solution to properly excite the target pattern. In the other extreme case (shown in Figure 4.12 J) using a very large error tolerance of 1, the resulting excitation could not sufficiently generate transverse magnetization of 0.1 inside the target region. We found the resulting excitation (shown in Figure 4.12 E), using an error tolerance of 10^{-4}, had minimum excitation artifacts. To quantify these excitation artifacts, the Euclidean norm of the residual of the excitation for each error tolerance was calculated and these are shown in Table 4.2. The minimum Euclidean norm was found when an error tolerance of 10^{-4} was used. Hence, the initial RF pulses were determined using the error tolerance that induced minimum excitation artifact, i.e. 10^{-4}. This value was also used in each consecutive iteration of the proposed algorithm.

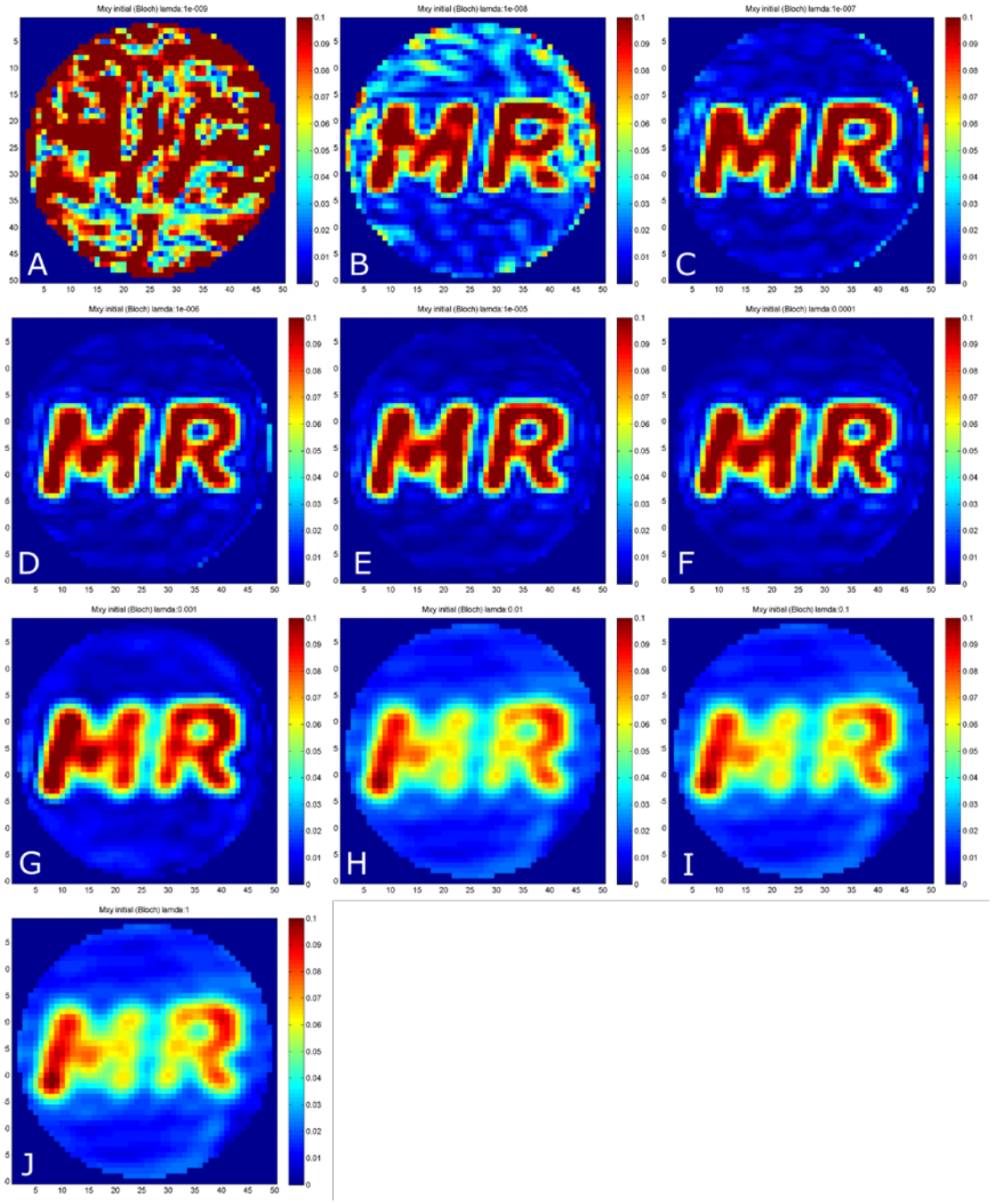

Figure 4.12 Images showing the excitation results of a Bloch simulation using eight-channel RF coil. The RF pulses were calculated using all of the individual B_1^+ field maps shown in Figure 4.3 along with different error tolerance (ε) values. For each subsequent image, the value of ε was increased by a factor of 10 from (A) 10^{-9} to (J) 1. The colour bar represents the transverse magnetization. The RF pulse length corresponded to a 6-turn k-space trajectory.

Table 4.2 Euclidean norm of residual, (‖ Ab-M_{des} ‖), calculated from the results shown in Figure 4.12. The error tolerance (ε) that generated the minimum residual was used.

ε	10^{-9}	10^{-8}	10^{-7}	10^{-6}	10^{-5}	10^{-4}	10^{-3}	10^{-2}	10^{-1}	1
‖ Residual ‖	5.824	1.556	1.021	0.959	0.963	0.955	1.007	1.249	1.249	1.249

To speed up the k-space trajectory for faster imaging, RF pulses can have fewer sampling points, i.e. fewer spiral turns in k-space. However, the image resolution will become worse and the excitation artifacts increase. To test the limit of the proposed method, we designed a set of very short RF pulses, which corresponded to a 4-turn k-space trajectory. To characterize if our proposed method can reduce excitation artifacts, we compared the resulting excitation using the benchmark RF pulses (Figure 4.13 A) with using the optimized RF pulses (Figure 4.13 B) from the proposed method. In the benchmark (i.e. the first iteration), significant excitation artifacts are observed and hot spots appear on the periphery of the cylindrical phantom. We found optimal RF pulses at the 89th iteration that reduced the intensity of these hot spots and also reduced the excitation artifacts at the center of the image as shown in Figure 4.13 B. To quantify how much the excitation artifacts are improved, normalized root-mean square (RMS) errors were calculated in the target pattern region and outside the region for each iteration. These results are plotted in Figure 4.14 as a function of iteration number. In the target region, the RMS errors are seen to oscillate for small iterations but reach steady-state after the third iteration. For the region outside the target pattern, the RMS error is a maximum at the first iteration and decreases as the iteration number is increased. The minimum RMS error is at the 89th iteration, which is about 17% less than the RMS error at the first iteration. A linear fit of the errors for iterations 21 to 100

confirm the slop is negligible. However, the RMS error appears to reach steady-state after about the 20th iteration. The transverse magnetization of a hot spot on the periphery of the cylindrical phantom was monitored and the values are plotted in Figure 4.15 as a function of iteration number. As we expect, the maximum value appears at the first iteration. However, the minimum value appears in the 8th iteration instead of the 89th iteration which has the minimum normalized RMS error. A histogram of the excitation artifacts for both methods is shown in Figure 4.16. Here, we plot the value of transverse magnetization over a range of 0 to 0.1, however there were a few higher values. In general, both methods have a tail extending towards the right-hand side. Considering the Rose criterion [99], the SNR of the image is required to be at least five to identify objects. Hence, any resulting excitation artifacts values less than 0.01 were considered as insignificant. Importantly, the proposed method has fewer pixels with values in the range of 0.02 to 0.1 than the benchmark method.

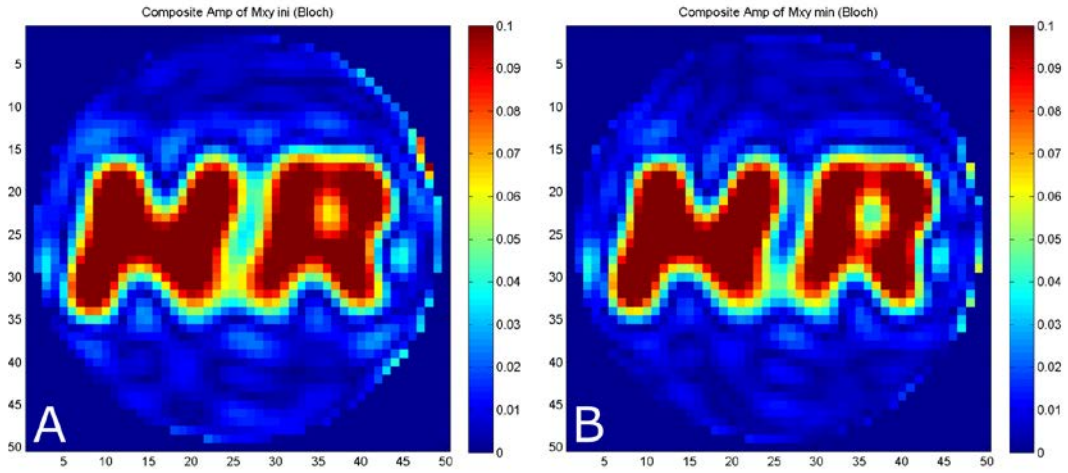

Figure 4.13 Images showing the resulting excitations of Bloch simulations using very short RF pulses that were calculated using (A) benchmark and (B) proposed methods. The RF pulse length corresponded to a 4-turn k-space trajectory.

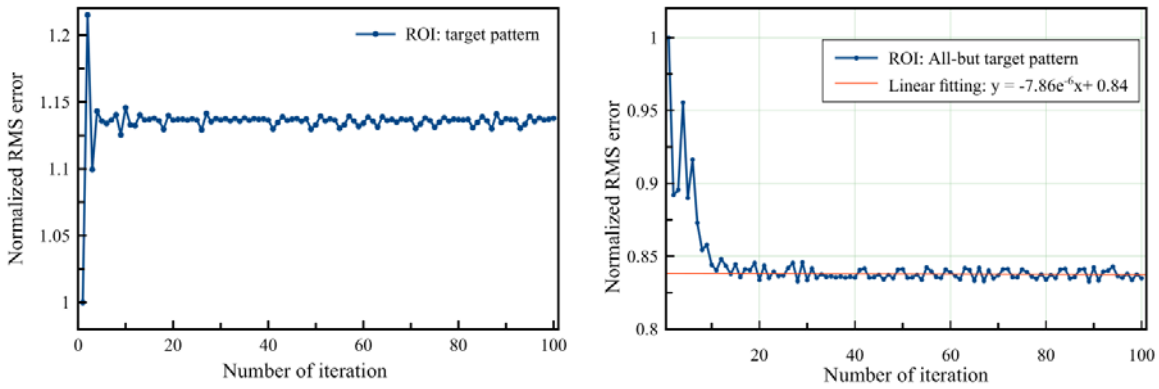

Figure 4.14 Plots showing the normalized RMS errors of the resulting excitation inside the cylinder phantom for the proposed method. The RMS errors were calculated in two ROIs: (left) target pattern “MR” and (right) all-but target pattern.

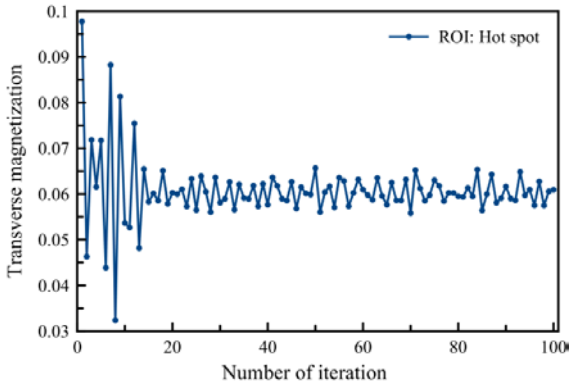

Figure 4.15 Plot showing the transverse magnetization corresponding to the location of the worst-case excitation artifact. That is, the artifact with the maximum value.

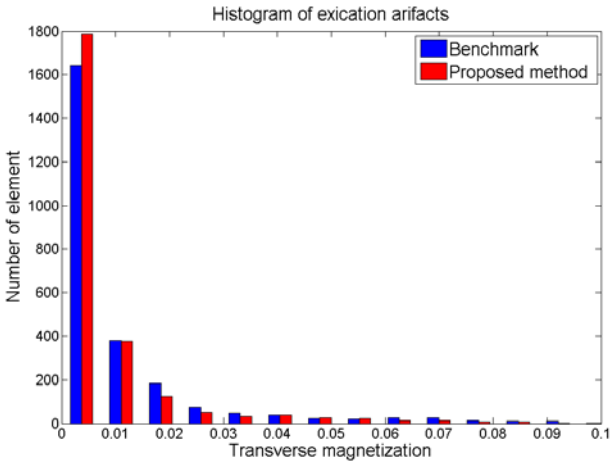

(A)

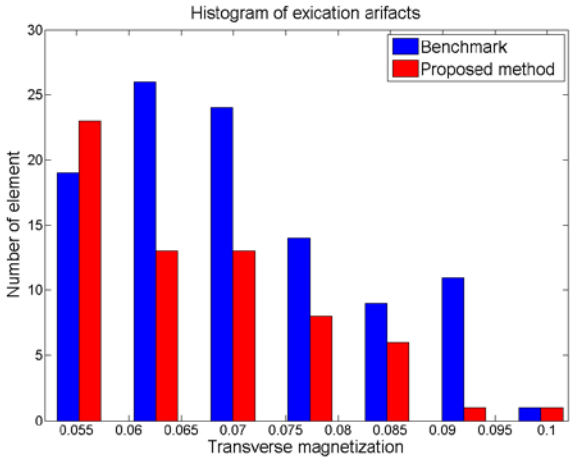

(B)

Figure 4.16 Histogram of the excitation artifacts inside the cylinder phantom but outside the target pattern for the proposed method. The values of transverse magnetization in range of (A) 0-0.1 and (B) 0.05-0.1

To determine if our proposed method can also reduce excitation artifacts in a heterogeneous phantom, we repeated the previous analysis using the phantom and the target pattern shown in Figure 4.8 B. We compared the resulting excitation using the benchmark RF pulses (Figure 4.17 A) with the result of using optimized RF pulses (Figure 4.17 B). Here, the transmitted RF pulses were very short corresponded to a 4-turn k-space trajectory. Using the benchmark RF pulses, the excitation artifacts are visible mostly between the two excitation regions and nearer the margin of the small pattern. In comparison, using the optimal RF pulses reduced these excitation artifacts.

Normalized RMS errors were calculated in the target pattern regions and outside the regions for each iteration. These results are plotted in Figure 4.18 as a function of iteration number. Results are similar to that of using the homogenous phantom. In the target region, the normalized RMS errors reach steady-state after the third iteration. Outside the target pattern, the RMS error is a maximum at the first iteration and quickly converges as the iteration number is increase. The minimum RMS error is at the 54^{th} iteration, which is about 21% less than the RMS error at the first iteration. A linear fit for data between iterations 21 to 100 to confirm there is no gradual decrease. Since there are no obvious excitation artifacts on the periphery of the phantom (e.g. transverse magnetization higher than 0.1), we monitored the artifacts in one pixel located between the two excitation regions. The resulting values of the transverse magnetization are plotted as a function of iteration number in Figure 4.19. There is no obvious trend. Unlike the result using the homogenous phantom, here both the maximum and the minimum values appear at a higher iteration number. Neither of these iteration numbers corresponds to the minimum normalized RMS error. A histogram analysis of the excitation artifacts for both methods is shown in Figure 4.20. Here, we plot the value of transverse magnetization over a range of 0 to 0.1, however there were a few higher values. In general, both methods have a tail on the right hand side. In addition, most of the excitation artifacts have values less than 0.01, which can be considered as insignificant. Furthermore, because these two methods have similar distributions of excitation artifacts, it is not obvious if the proposed method has fewer excitation artifacts.

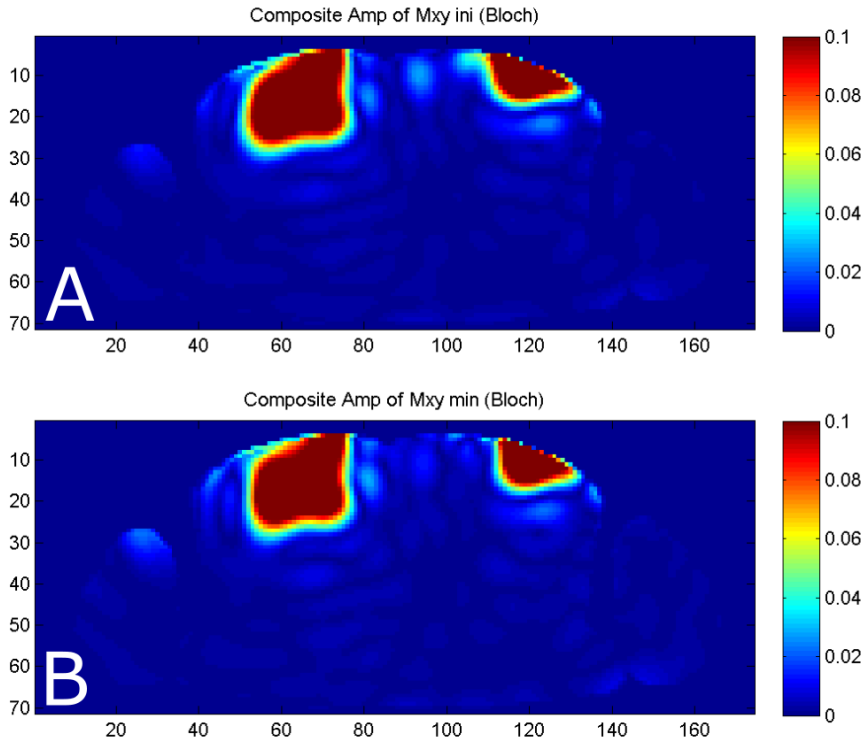

Figure 4.17 Images showing the resulting excitations of Bloch simulations using very short RF pulses that were calculated using (A) benchmark and (B) proposed methods. The RF pulse length corresponded to a 4-turn k-space trajectory. The colour bar indicates the normalized magnetization.

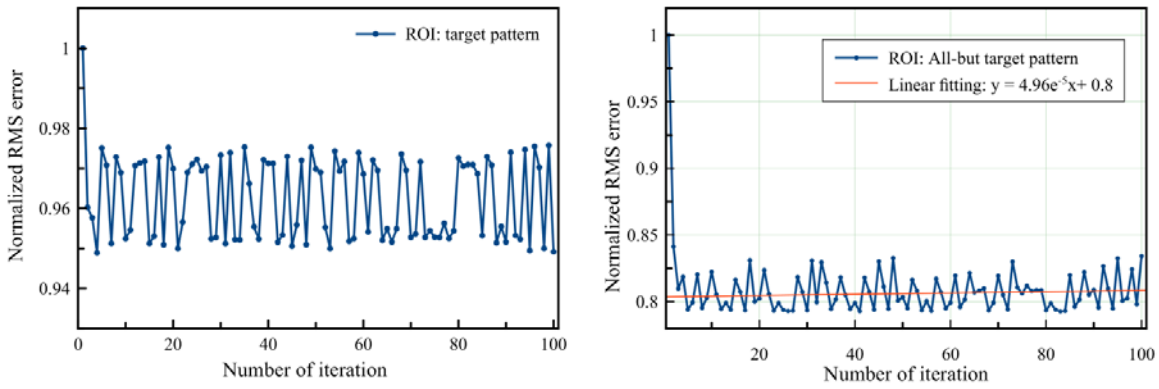

Figure 4.18 Plots showing the normalized RMS errors of the resulting excitation inside the Ella phantom for the proposed method. The RMS errors were calculated in two ROIs: (left) target pattern and (right) all-but target pattern

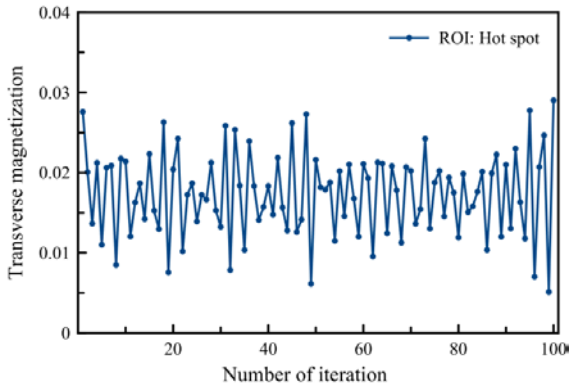

Figure 4.19 Plot showing the transverse magnetization corresponding to the location between the two excitation regions.

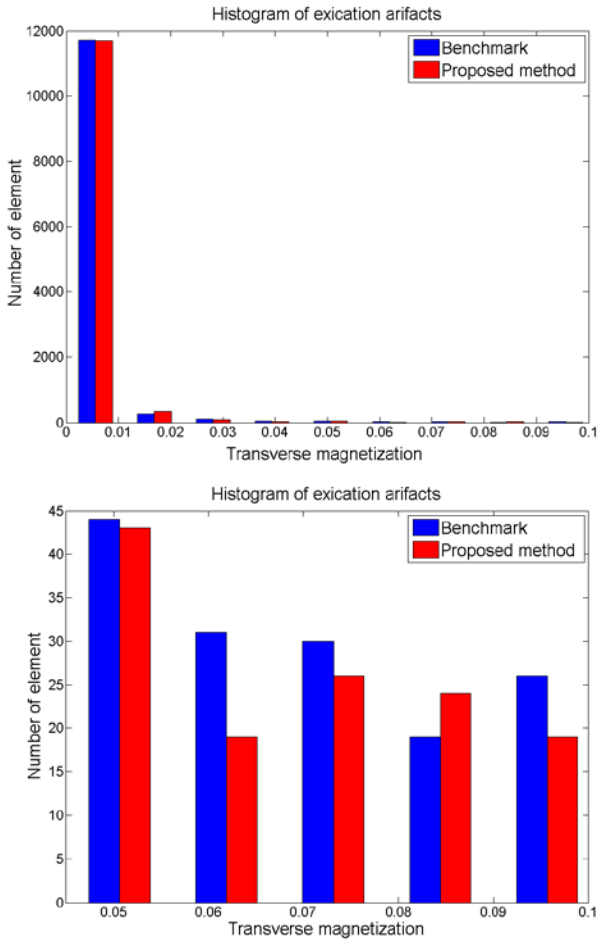

Figure 4.20 Histogram of the excitation artifacts in Ella phantom for the proposed method. The values of transverse magnetization in range of (A) 0-0.1 and (B) 0.05-0.1

4.4 Discussion and conclusions

We have proposed a method incorporated Bloch simulations into an iterative algorithm to update the desired target pattern in iteration. The theory of negative excitations and the workflow for reducing excitation artifacts have been described. We have shown how to generate a negative excitation with two transmit channels and implemented the CG algorithm to calculate RF pulses. We also showed how biases result from using different error tolerances in a CG algorithm. Small FOV excitations (i.e. MR-shape logo) with an eight-channel transmit coil array were made in both homogenous and heterogamous phantoms. We quantified excitation errors inside and outside the target pattern, and found optimized RF pulses that had minimum RMS error. Results of simulations were found to have less excitation artifacts while using the optimized RF pulses.

There are three major theories for RF pulse design applied to small FOV excitation. Katscher et al. [40] first used the term *Transmit SENSE* for parallel excitation. This is analogous to the *SENSE* technique in parallel (receive) imaging. Compared to image-domain methods, their method is frequency-domain based and is more complicated. Hence their method is not as widely used as image-domain methods. At the same time, Zhu [41] proposed a method where RF pulses are designed in both image and frequency domains. This method is also known as the removal-of-aliasing method, which is used to suppress the aliasing in a specific direction of under-sampled k-space. Hence this method is limited because it has a restricted choice of k-space trajectory (e.g. echo-planar trajectory). Our proposed method also removes the excitation artifacts due to under-sampling of the k-space trajectory. However, the concept of removing

excitation artifacts is different between our method and Zhu's method. The major difference is that our proposed method focuses on the improvement of excitation artifacts that are not as predictable as aliasing artifacts. In addition, our proposed method is image-domain based only, and we have the flexibility to choose any k-space trajectory.

We found the choice of error tolerance in the CG algorithm affected the accuracy of the small FOV excitation. When we evaluated the performance of our proposed method, we found a relative improvement when comparing results to those of the original method (i.e. the first iteration). The resulting excitation and the Euclidean norm of excitation error were shown in Figure 4.12 and Table 4.2. Choosing a different error tolerance for the original method caused different excitation errors. In some cases, there were no obvious excitation artifacts. Hence, the performance of the proposed method may be misestimated. In general, the value of error tolerance must be much higher than the floating-point relative accuracy (e.g. eps(1) = 2.22e-16 in Matlab). In addition, choosing a small value does not always lead to the best solution. This is due to how the stopping criteria are defined in the algorithm. If the error tolerance is too small, the algorithm would fail to detect when it has converged and the iteration would not be terminated. In contrast, if the error tolerance is too large, it gives a poor result. Therefore, it is important to survey a wide range of error tolerances for the first iteration.

The total calculation time of the proposed method depends on the image size and the number of iterations. For the example of excitation of an MR-shape region in a 50-by-50 image size, the calculation time per iteration was about 1 minute. Although we used 100 iterations, Figure 4.14 show that the RMS errors reached steady-state after

about 20 iterations. We applied linear curve fitting to the RMS errors from the 21st to the 100th data point, and found that the fitted curve is a horizontal line. Although the minimum RMS error happened at the 89th iteration, this is misleading. We can always find a RMS error very close to the minimum one, although at a much lower iteration. Hence, this analysis suggests that using 100 iterations is not necessary and we can determine suitable RF pulses, which have sufficiently small excitation errors, with much less iteration (shorter time). The RMS error in the target pattern reached steady-state value of about 1.13. This suggests that our proposed method makes a trade-off between target pattern uniformity and artifacts reduction. In addition, the algorithm did not diverge as the iterations increased. Thus there is no penalty to doing too many iterations. If the configuration of the RF coil or the desired target pattern is altered, the required number of iterations might be different. We also investigated the example of the Ella phantom (see Figure 4.18). The results reached steady state faster than those using the cylinder phantom and the fitted curve is also a horizontal line. Hence our findings remain the same.

In summary, we have shown the advantage using multi-channel transmission over single-channel transmission for small FOV excitation. Our results support the hypothesis of negative excitation by using an Eigen-mode RF coil and incorporated this concept into the workflow of RF pulse design. In addition, we proposed a Bloch-simulation based CG algorithm to reduce excitation artifacts. Therefore, using the proposed method for RF pulse design could result in improved transmit array designs with reduced excitation errors.

Chapter 5: Transmit array design strategies for reducing excitation artifact and understanding the impact of inductive coupling on local SAR hot spots in parallel transmission MRI

A transmit array coil was designed and optimized for an application of small field-of-view (FOV) excitation. We investigated the impact of inductive coupling for receive coils in Chapter 3. Using the simulation procedure we established in chapter 3, we also investigated how inductive coupling affects specific absorption rate (SAR) estimation, and predict the estimation error due to shortening the RF pulses. In addition, we describe a method to reduce the excitation artifacts by tilting a coil element to further improve the performance of small FOV excitation.

5.1 Introduction

Parallel transmission is a state-of-the-art technique which has many applications including RF shimming [100], [101] and spatially selective RF excitation [40], [41], [102]. This technique is particularly important in high-field (≥ 3T) functional MRI studies where the MR imaging performance is dramatically increased due to an improvement in the B_1 or B_0 field homogeneity. In addition, the image quality in general is better than with conventional MRI and avoids the central brightening artifact [39] that plagues 3T MR systems. Cardiac and breast MRI are important fields that also benefit from this technique because of B_1 shimming [103]–[105]. Small field-of-view (FOV) RF excitation has a potential of improving cardiac MRI because of higher temporal resolution [106]. However, when applying small FOV RF excitation with single-channel transmission, the length of the multi-dimensional RF pulse is very long and is a concern with respect to specific absorption rate (SAR). However, the RF pulse length can be reduced by using

a parallel transmission technique called transmit SENSE (Tx-SENSE) [44], [107], [108]. A difficulty is the resulting RF waveforms are arbitrary and may lead to local SAR hot spots. Thus the SAR prediction should be carefully considered.

For scanners with higher B_0 field strength the RF power dissipated as heat in the human body becomes a major concern of RF safety: the RF power dissipation increases roughly with the square of the B_0 field strength [109]. In multi-transmit (multi-Tx) MRI systems, the predication of global and local SAR is based on numerical electromagnetic (EM) simulations. During a scan, the actual RF power applied to a specific pulse sequence is rescaled based on the simulated SAR values and is limited by FDA guidelines [73]. However, when multiple transmit channels are employed in parallel transmission, the prediction becomes more complex. The induced E-field distribution is a superposition of individual E-field distributions for each channel and may cause a high local SAR (i.e., a 'hot spot') due to constructive interference of the individual E-field distributions. In addition, the E-field distributions for individual transmit channels are affected by dielectric and conductive properties of the human body [110], causing further asymmetries in the induced E-field distributions. Although it is possible to monitor global SAR during multi-Tx MRI [111], there is no real-time in-vivo method of monitoring local SAR or temperature changes. Further complications arise in multi-Tx MRI because complex time-varying amplitude and phase modulations of the RF waveforms are applied to each transmit channel to form irregular spatial excitations, thus leading to local SAR hot spot distributions that are difficult to predict.

The complex interaction of the desired B_1^+ map and corresponding E-field distribution is the fundamental knowledge required for parallel transmission. Hence, the

performance of Tx-SENSE depends on RF coil design and RF pulse design, together with an accurate prediction of local SAR distribution. Clearly, design goals that include accurate predictions of local SAR and minimization of local SAR hot spots are particularly important for patient safety in parallel transmission MRI. The RF coil array for multi-Tx systems determines both the B_1^+ maps used for Tx-SENSE RF pulse design and the simulations of induced electric field distributions for SAR estimation. It is well known that inductive and resistive coupling between array elements affects the resulting B_1^+ maps and E-field distributions [112]. Therefore, to optimize transmit array (Tx-array) design and predict local SAR distribution through simulations, it is important to take into account the impact of array coupling. In Chapter 3, we showed the inductive coupling in receive arrays may be manipulated and incorporated into the simulation model by using a preamplifier model with appropriate input impedance termination.

Local hot spots from excitation are partially due to strong asymmetries in B_1^+ maps of individual elements of a transmit array. These hot spots are more prominent at higher B_0 fields used for cardiac and breast imaging. Therefore, improved symmetry and reduction of strong local B_1^+ maps of individual array elements will reduce such hot spots and consequently reduce local SAR.

5.1.1 Aim

The general procedure of optimizing coil design for Tx-SENSE is shown in Figure 5.1. Here we can see that coil design starts with EM simulation of individual transmit channels to give B_1^+ maps and E-field distributions, which are the outputs. The waveforms of these RF pulses are then used as weighting factors of individual E-field

distributions for SAR estimation. In addition, the B_1^+ maps are used along with the RF pulses to simulate the small FOV excitation. Using our constructed coil, we acquired B_1^+ maps in a MR scanner to compare with the simulated ones.

In the experiment, the coil elements are coupled to each other, especially during transmission. Typically, this coupling is not taken into account in the simulation. However, the problem is that this coupling will change the field distributions. For future clinical use, we would pre-calculate the RF pulses using the simulated B_1^+ maps and transmit these pulses with the constructed coil. If there is a mismatch between the EM-field maps from the constructed coil and the field maps from the simulations, then this may lead to incorrect SAR estimation and degrade the performance of small FOV excitation.

Hence, the aim of this chapter is to investigate how inductive coupling in transmit array coil design also influences the design of the RF pulse. Specifically, we show transmit array design strategies for reducing excitation artifacts and local SAR hot spots in small FOV excitation. This includes investigating the accuracy of small FOV excitation and evaluating SAR. In addition, we also investigated the feasibility of altering the coil geometry to improve small FOV excitation and to avoid local hot spots. In general, a coil element is not tilted with respective to the surface of the phantom or patient. However, we proposed that modifying coil geometry by tilting a coil element may generate a more symmetrical B_1^+ map that might avoid any hot spots. We simulated two coil configurations to evaluate the impact of inductive coupling in SAR and the asymmetry of EM fields in excitation errors. One coil configuration is simple and is designed to

evaluate overlap decoupling, and the second configuration is intended to be a cardiac coil [62].

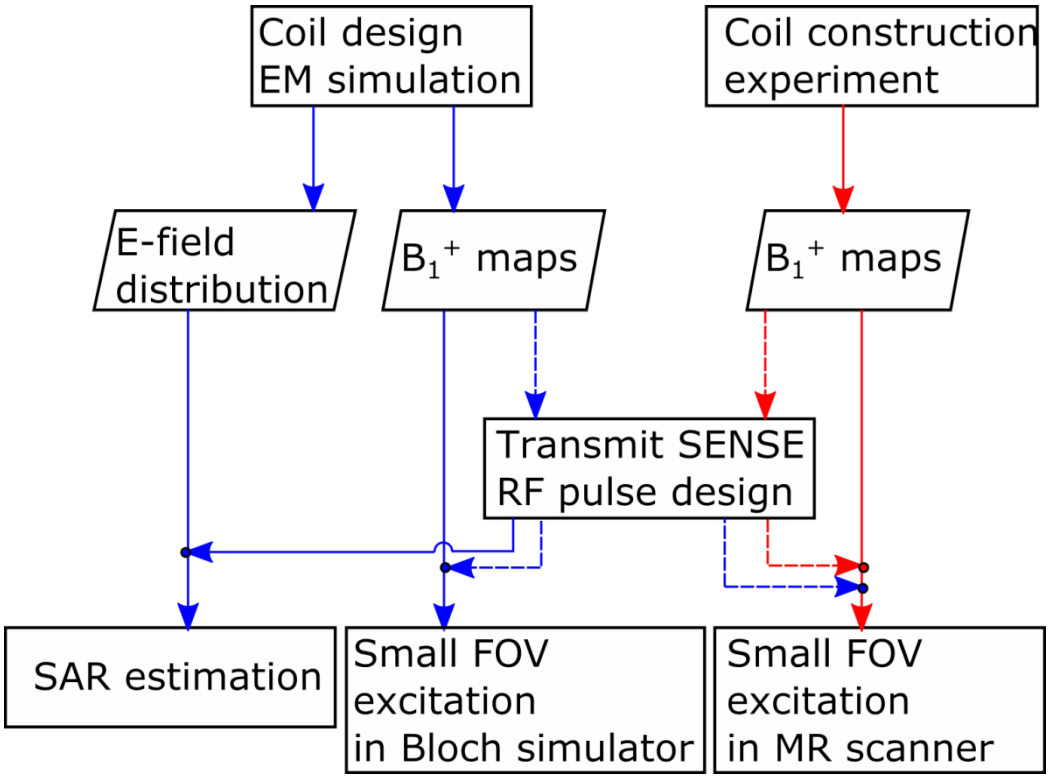

Figure 5.1 Flowchart showing the coil optimization for small FOV excitation and SAR estimation in a simulation (blue) and in an experiment (red). The dashed lines indicate that the B_1^+ maps are the inputs and outputs of RF pulse design

5.2 Materials and methods

5.2.1 RF coil configuration

Two eight-channel transmit-array coils were modeled in a finite difference time-domain (FDTD)-based EM simulator (SEMCAD X v14.8, SPEAG, Zurich, Switzerland). The theory of FDTD has been described in Chapter 2. The simulations were performed with a simplified cardiac torso model (60 cm x 47.4 cm x 24 cm) for two eight-channel cardiac transmit-array coils shown in Figure 5.1. Both coils were composed of anterior

and posterior sections and the coil layout is illustrated in Figure 5.2 as five and three overlapping loop coils respectively. Here we used different simulation models to evaluate the impact of coupling (Figure 5.2 A) and to evaluate excitation artifacts (Figure 5.2 B). Figure 5.2 A is the simplest model to show overlap decoupled coil elements and Figure 5.2 B is candidate coil design for small FOV excitation. For the coil configuration shown in Figure 5.2 B, the coils have a configuration of seven (anterior) and one hexagonal (posterior) coil elements. Each coil element contained either seven or six capacitors (28 or 20 pF) and was tuned to 123.2 MHz.

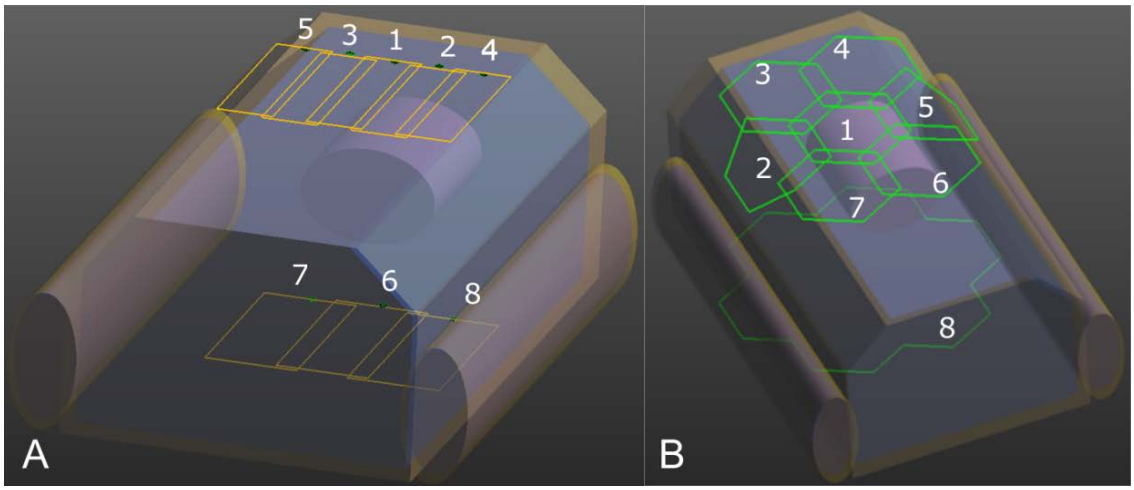

Figure 5.2 Schematics showing two transmit array coil configurations and the torso phantom for evaluating the impact of (A) inductive coupling and (B) excitation artifacts.

5.2.2 Inductive coupling model for SAR

To address the impact of inductive coupling, EM fields were calculated for the three scenarios shown in Figure 5.3 based on the model in Figure 5.2 A. Here, “isolation” (Figure 5.3 A) is where each element was simulated separately without inductive coupling, and “overlap decoupled” (Figure 5.3 B) is how the coil was constructed. In the overlap decoupled case, it is important to note that the next neighbouring coil elements

are still coupled. When we build a coil, the layout of the finished coil may be slightly different from the original design. To mimic this, one coil element was slightly shifted from its optimal position for overlap decoupling as illustrated in Figure 5.3 C. Here, “coupled” is where each element was simulated in the presence of other coupled elements that were terminated with 50 ohms.

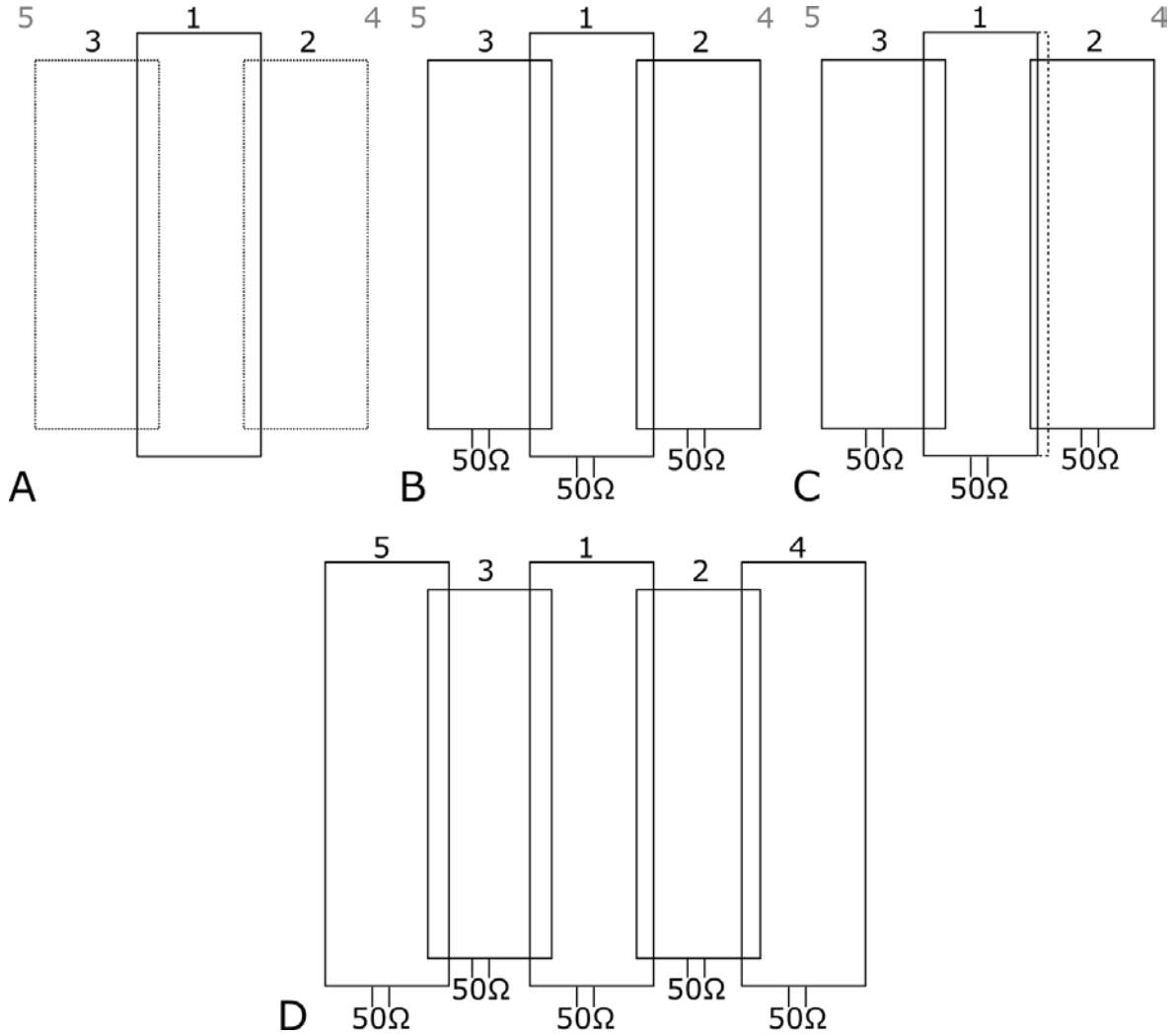

Figure 5.3 Diagrams showing different scenarios of coupling for the model shown in Figure 5.2, (A) isolated, (B) overlap decoupled, and (C) coupled coils. In (C) the one leg of the central element is shifted by 3mm from the dashed line to mimic a small variation during coil construction. In (D) the five coil elements are present in the model to include crosstalk between the next neighbouring coil elements. Note that all coil elements had identical lengths.

5.2.3 B_1^+ mapping for inductive coupling model

To validate the impact of coupling on the B_1^+ maps, the coil based on Figure 5.2 A was constructed and is shown in Figure 5.4. For simplicity, only the posterior section was used for validation. The coil was made from a copper-clad printed circuit board that was milled to give the layout of the three coil elements with a width of copper trace of 5 mm. Each coil element was tuned and matched at 123.2 MHz using a calibrated network analyzer (Agilent E5601A). A preamplifier (MPB-123R20-90, Hi-Q.A. Inc.), cable trap, T/R switch and matching circuit were added for each coil element. The double-angle method [113] was used to acquire the B_1^+ maps in a 3T MR scanner (Siemens, Trio). The parameters used in this gradient echo sequence were: acquisition matrix size = 128 x 512, TR/ TE = 2000 ms/15 ms and slice thickness = 5 mm. As built, the coil mimicked overlap decoupled scenario (Figure 5.3 B). To mimic an isolated coil (Figure 5.3 A), only the central loop was used to transmit and receive the MR signal, the other loops were physically open. The coupled scenario illustrated in Figure 5.3 C was also implemented on the constructed coil by shifting one leg of the central coil element by 3mm. The outer loops were not geometrically decoupled from each other. They were resonant loops and did not transmit or receive.

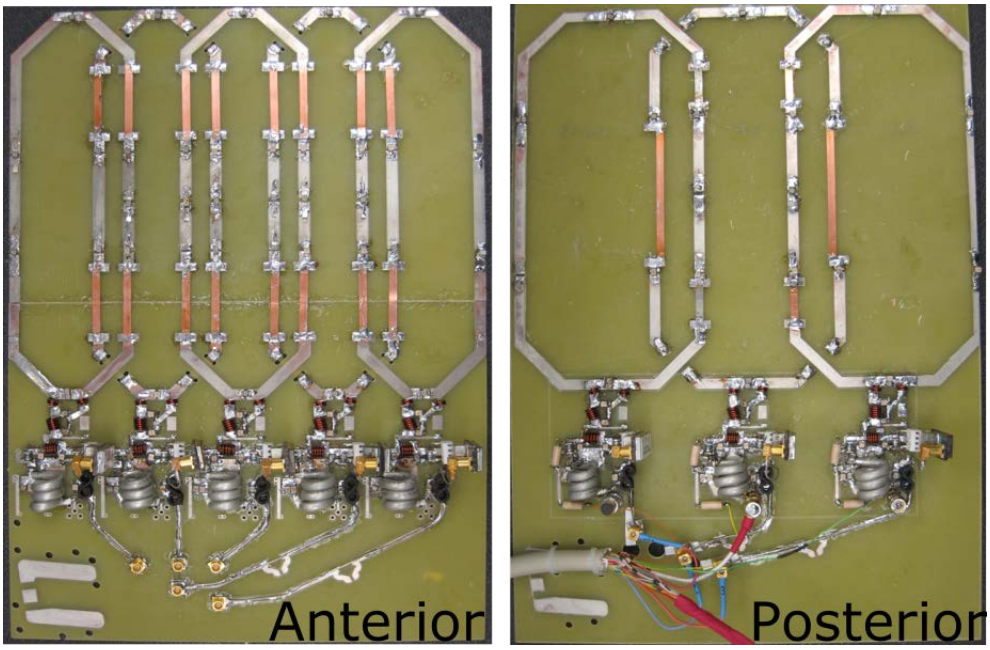

Figure 5.4 Photographs showing the constructed coil corresponding to Figure 5.1 A. Both sections cover size of 19 cm-by-22.68 cm.

5.2.4 B_1^+ mapping for reducing excitation artifacts

In order to investigate the excitation error in small FOV excitation associated with the asymmetry of the B_1^+ map, we simulated the central coil element of the anterior section in Figure 5.2 B. In general, a coil element is not tilted with respective to the surface of phantom or patient. When RF coil is design for receive MR signal, the amplitude and field distribution of its B_1^- magnetics field is optimized for high SNR. As mentioned before, inductive coupling would degrade the SNR. It has been shown that a venetian-blind design of receive array could reduce inductive coupling between coil elements and remain SNR [114]. Since our ultimate goal is to design a transmit-and-receive array coil, we proposed that a tilted or bent coil element may generate a more symmetrical B_1^+ map that might avoid any hot spots. To search for the suitable tilt or bend location, Figure 5.5 shows various ways the loop element was tilted or bent away from the torso surface. Initially, we arbitrarily chose a fixed angle of 25^o. The coil

element was either tilted or bent along different sagittal planes (Z-Y plane) to determine the degree of asymmetry of the B_1^+ map. After finding the best plane to tilt or bend the coil element, we compared the influence of varying the angle (Figure 5.6).

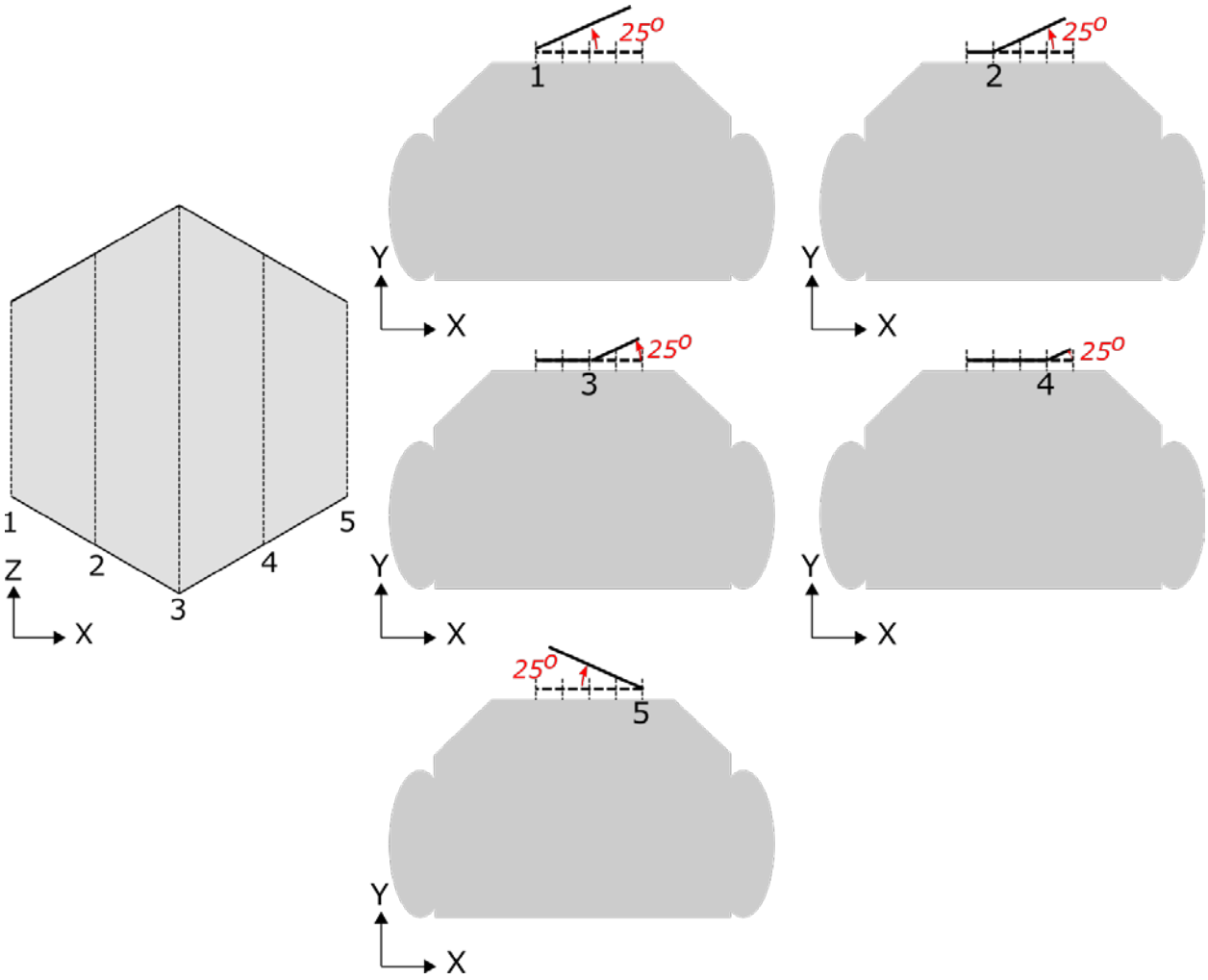

Figure 5.5 Diagram showing a single loop that is tilted or bent away from the surface of the torso phantom by an angle of 25° along five dashed lines.

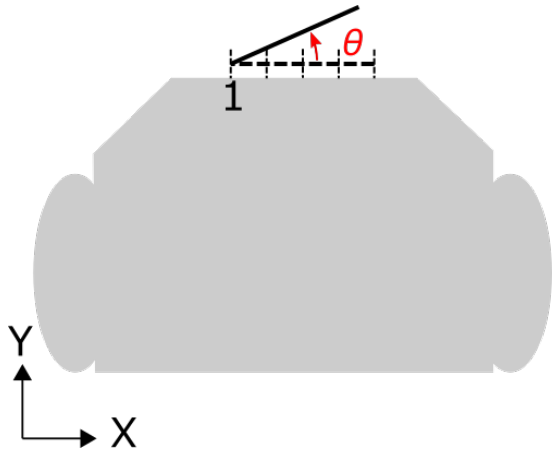

Figure 5.6 Diagram showing a single loop that is tilted away from the surface of the torso phantom by various angles (θ) with respect to the dashed line 1 in Figure 5.5.

5.2.5 Reducing excitation artifacts by titling coil elements

To evaluate the impact of asymmetric B_1^+ maps in the optimization of RF coil design for eight-channel small FOV excitation, Figure 5.7 A shows the planar coil configuration assigned as a reference design. In this design, the coil elements labeled 1, 2 and 5 fit the surface of the phantom to represent a clinically-used cardiac coil. The asymmetries of the resulting B_1^+ maps were compared with those of the tilted and bent coil configurations shown in Figure 5.7 B. Here, only coil elements in the excitation plane were tilted or bent (i.e. three of the seven coil elements in the anterior section). This coil configuration was determined based on the findings in the previous investigation where only the central coil element was tilted or bent.

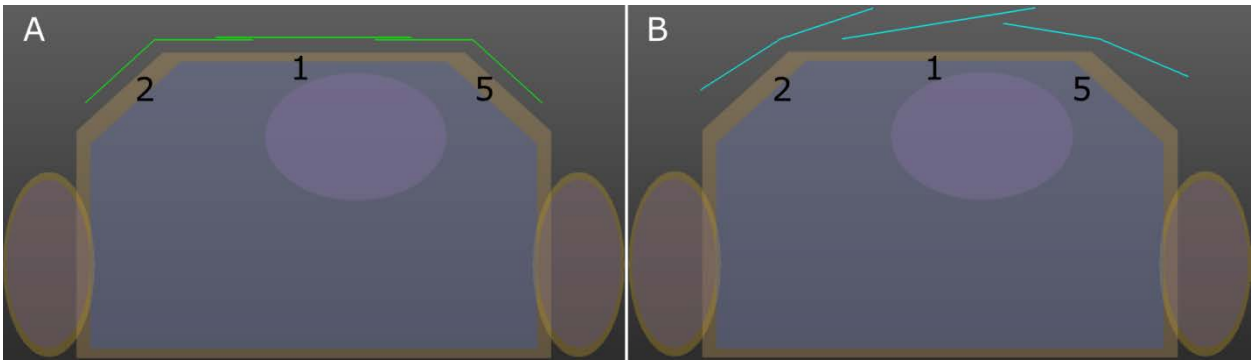

Figure 5.7 Diagrams showing a transverse plane through Figure 5.2 B. Visible are three of the seven channels for the anterior section of the coil. (A) is a reference design and (B) is where the three coil elements are tilted or bent.

5.2.6 RF pulse design for transmit SENSE

5.2.6.1 Inductive coupling model

To evaluate the impact of coupling on the multi-Tx array system, two sets of RF pulses were designed; one was based on isolated coil elements and the other on more realistic overlap decoupled coil elements. The RF pulse design software (Musaik Tx-array Beta version, ZMT, Zurich, Switzerland) used here is a spatial-domain based method and it determined a set of RF pulses by finding a pseudo-inversion of a least-squares problem (the theory of the RF pulse designer is discussed in Chapter 4). The design of these RF pulses used, as input, B_1^+ maps generated from either isolation or coupled simulations using the eight-channel transmit array shown in Figure 5.2 A. We chose for an excitation pattern a homogenous box covering the central region of the phantom near the heart. The parameters used for RF pulse calculation were: FOV = 55.5 cm x 35.8 cm, excitation FOV = 12 cm x 12 cm, object matrix size = 140 x 91, maximum amplitude of gradient = 40 mT/m, slew rate of the gradient = 200 T/m/s, number of spiral turns (N_t) = 16, and the length of RF pulse (T_p) = 5.1, 3.9, 3.1 and 2.6

ms associated with α = 1, 2, 3, and 4 in variable density k-space trajectory [115] (Full Nyquist sampled spiral: N_t/T_p = 70/46.3 ms).

5.2.6.2 Reduction of excitation artifacts

The same RF pulse design software was used to evaluate the impact of tilting or bending the coil elements as shown in Figure 5.7 B. Here we used eight-channel small FOV excitation with the model shown in Figure 5.2 B. To design the required RF pulses we used a target excitation pattern of a rectangular region shown in Figure 5.8. The parameters used for RF pulse calculation were: object matrix size = 92 x 52, pulse length = 4.7 ms, maximum gradient amplitude = 40 mT/m, slew rate=200 T/m/s, number of spiral turns =14, excitation FOV = 10.5 cm x 8 cm and FOV = 45.4 cm x 25.4 cm (transversal) in variable density k-space trajectory. The B_1^+ maps were simulated for the various tilt angles and locations, but the rest of the parameters for RF pulse design remained the same.

5.2.7 Estimation of excitation error of transmit SENSE for coil design comparison

To evaluate excitation error i.e., any excitation outside the desired target pattern, we used a Bloch simulator to predict the results of the excitation using various RF pulses. Normalized root-mean-square error (NRMSE) was calculated for each set of RF pulses to quantify the excitation error and is expressed as

$$\text{NRMSE} = \frac{\left\| M_{\text{Bloch}} - M_{\text{desired}} \right\|_w}{\left\| M_{\text{desired}} \right\|_w} \tag{5.1}$$

Here M_{desired} is the desired target pattern and M_{Bloch} is the simulated excitation pattern from the Bloch simulator. w is the spatial weighting matrix.. The notation of $\| M_{\text{Bloch}}$-

$M_{desired}\|$ is the Euclidean norm and is also called L^2 norm. W is a weighting matrix containing assigned error weighting factors and its matrix size is identical to that of $M_{desired}$. To take into account the usage of parallel imaging, this weighting matrix was designed to emphasize the errors in four region-of-interests (ROI), which are labeled as regions 1, 2, 3 and 4 in Figure 5.8. In additional, NRMSE were calculated within two ROIs shown in Figure 5.8: (1) a combination of region 1 and region 2 for evaluating parallel imaging and (2) region 5 for detection of hot spots. In order to compare the excitation error for different geometries, the NRMSE for each case was normalized to that of the benchmark coil shown in Figure 5.7 A.

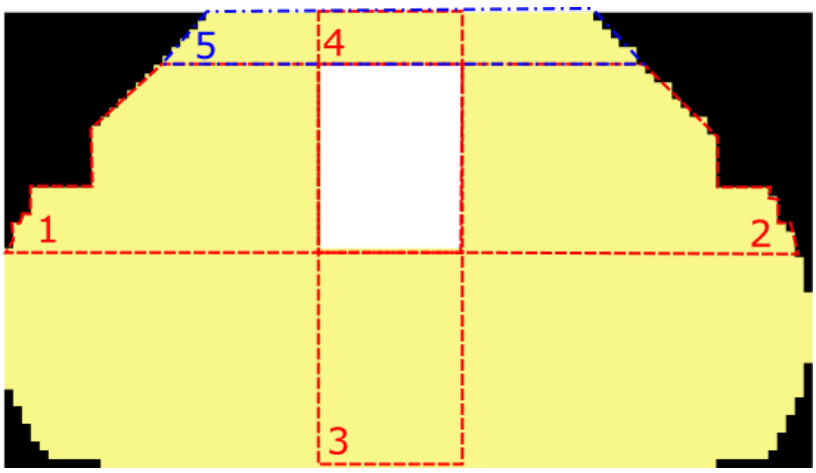

Figure 5.8 Diagram showing the target excitation pattern (white region) of a rectangular box which represents a position and size of a heart. Five ROIs are defined for the evaluation of excitation error.

5.2.8 SAR estimation in transmit SENSE

In order to estimate SAR for Tx-SENSE, the value of SAR per pixel was calculated by using the following equations.

$$SAR(\vec{r}) = \frac{\sigma(\vec{r})}{2\rho(\vec{r})}\frac{1}{T}\int_0^T \left\|E(\vec{r},t)\right\|^2 dt \qquad (5.2)$$

and $$E(\vec{r},t) = \sum_{p=1}^{P} a_p(t) \cdot E_p(\vec{r})$$

where σ and ρ are the conductivity and density of the phantom, r is the spatial position of each voxel, and T is the pulse length. The E-field distributions are spatial-temporal functions and are a superimposition of *P* transmit channels. Weighting factors a_p are the amplitudes of RF waveforms at time points t. It should be noticed that Equation 5.2 for SAR calculation is different from that was defined in Chapter 2. This is because the applied RF pulses have arbitrary waveforms and pulse lengths in small FOV excitation. Therefore, when we superimpose all the E-field distributions, the local hot spot can form at any location and is difficult to predict in small FOV excitation.

If the parameters, e.g. k-space trajectory, for RF pulse design are changed, the weighting factors for the SAR must be associated with the new set of RF pulses and change correspondingly. Here we first calculate local SAR per voxel over all voxels and then find the maximum value of local SAR, which is commonly called a hot spot or peak SAR. In addition, global SAR is also calculated by averaging the SAR values over the whole volume of the phantom. Global SAR is a scaling factor of the total power transmitted by the RF coil. Hence, for a given RF coil design, SAR varies with transmit RF pulses and was a criterion to optimize the RF coil design.

5.3 Results

5.3.1 B_1^+ mapping for inductive coupling model

To validate the impact of inductive coupling, the posterior section of the eight-channel transmit array was simulated and the EM fields determined. Figure 5.9 A shows the resulting B_1^+ maps of the central coil element. Enlargements of the dashed region

show the isolated scenario (Figure 5.9 C) and the coupled scenario (Figure 5.9 E). For comparison B_1^+ maps were acquired in the MR scanner using the constructed coil with identical configurations as the simulated coil. We acquired B_1^+ maps for isolated scenario (Figures 5.9 B and D) and the coupled scenario (Figure 5.9 F). The measured B_1^+ maps show a good qualitative agreement with the simulated B_1^+ maps. It can be seen that all B_1^+ maps are asymmetrical, but the coupled B_1^+ maps have fields extending towards the left-hand side (shown by the arrows) where the neighboring loop element was placed. This is expected because the crosstalk resulting from the mispositioned coil element (Figure 5.3 C) shares the field distribution.

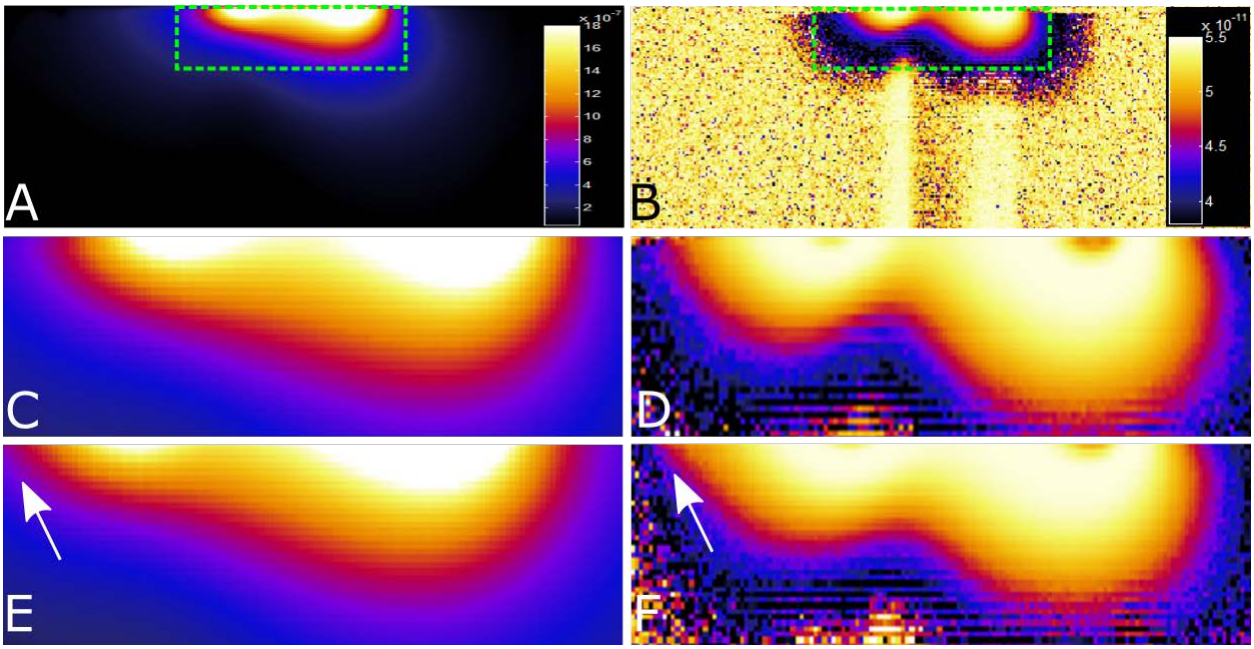

Figure 5.9 Images showing B_1^+ maps where the left column is the simulated results and the right column is the experimental measured results. for isolated (A through D) and coupled (E and F) scenarios. Images C and D are enlargements of the dashed regions shown in images A and B. The arrows show the regions where there is crosstalk with a neighboring element. Here three elements were located at the top of the images and only the central element was used to transmit and to receive.

5.3.2 Small FOV excitation for inductive coupling model

If there is a mismatch between the designed RF pulses and the B_1^+ maps, the predictions of the resulting excitation and SAR could be wrong. To show the influence of the three coupling scenarios on the resulting excitations, Figure 5.10 shows the prediction of the Bloch simulator with four different combinations of RF pulses and B_1^+ maps. In this case, eight coil elements were used. Assuming ideal fields exist in a MR scanner resulted in the excitation shown in Figure 5.10 A. This is the result of applying isolated RF pulses to isolated fields, i.e. no coupling. It can be seen that there are excitation artifacts near the top center of the image close to the position of the coil element. Because coupling between next neighbouring coil elements always exists, we applied coupled RF pulses to coupled fields, both of which were generated in the overlap decoupled scenario where only the neighbouring coil elements were decoupled (Figure 5.3 B). The resulting excitation is shown in Figure 5.10 B and this produced less excitation artifacts close to the surface of the phantom as compared to the result for the isolated scenario shown in Figure 5.10 A. In general, the procedure of small FOV excitation is to apply the RF pulses determined for the isolated scenario to the case that includes coupling between next neighbours coil elements. To mimic this procedure, coupled fields were generated by including crosstalk between the next neighbouring coil elements as shown in Figure 5.3 D. The excitation resulting from this procedure is shown in Figure 5.10 C. It can be seen that the average flip angle inside the target region is lower than the target flip angle. Although a coil may not have perfect overlap decoupling as illustrated Figure 5.3 C, we would still apply RF pulses determined from an overlap decoupled scenario, which could lead to misinterpretation of SAR estimation.

Figure 5.10 D shows the effect of applying RF pulses determined for the overlap decoupled scenario to coil elements that were not perfectly overlap decoupled (Figure 5.3 C). In this case, there are more excitation artifacts and the target pattern is less uniform. This resulting excitation has a poorer performance than for properly overlap decoupled coil shown in Figure 5.10 B.

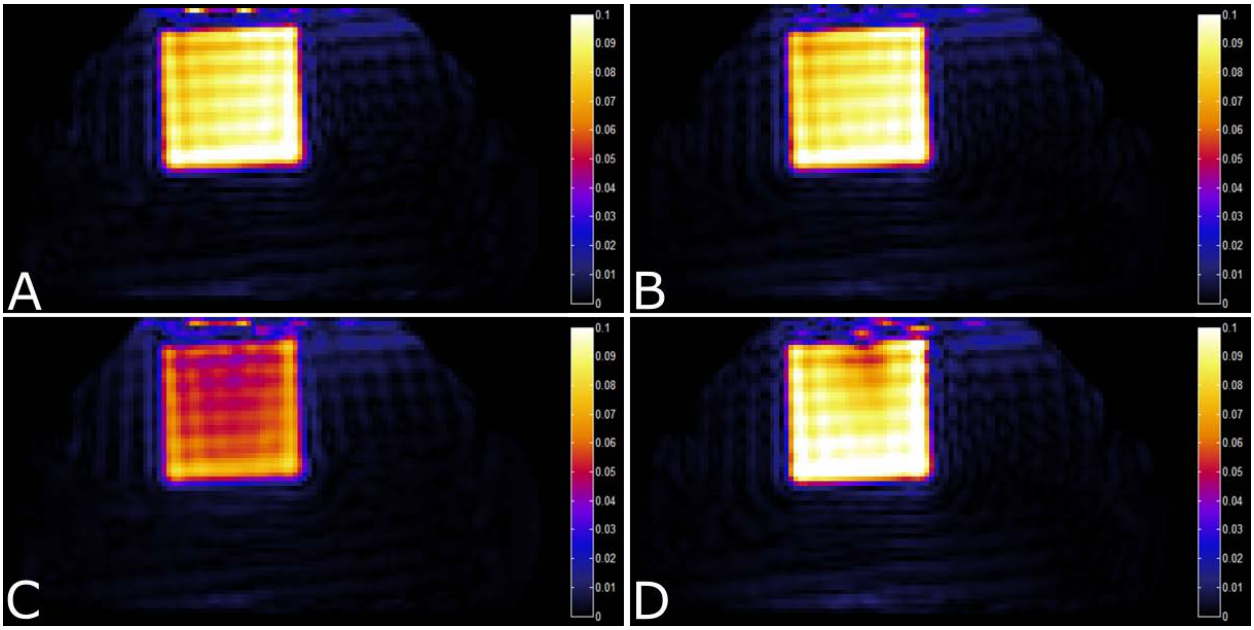

Figure 5.10 Images showing simulated small FOV excitation when both RF pulses and B_1^+ maps were either in isolation (A) or overlap decoupled (B) scenarios. In (C) the RF pulses assumed no coupling but the coil used overlap decoupling and this had some crosstalk. In (D) the RF pulses assumed overlap decoupling, but the coil was not perfectly overlap decoupled. The colour bar corresponds to the transverse magnetization relative to M_0. Here eight channels were used for excitation.

5.3.3 SAR map for inductive coupling model

For the small FOV excitation described above, we found the interactions of RF pulses and B_1^+ maps were affected by coupling. Subsequently, SAR distributions were expected to be directly affected by the combined effect of RF pulses and E-field distributions as described by Equation 5.2. To characterize this effect, we calculated

SAR values for each voxel of the phantom for the same four coupling combinations used for Figure 5.10. The results for the isolated scenario, i.e. no coupling, are shown in Figure 5.11 A. When the effect of coupling is taken into account, Figure 5.11 B shows that the prediction of the location of the maximum hot spots shown in Figure 5.11 A could be wrong. Here we can see the maximum hot spots appear at the anterior region for the isolated scenario (Figure 5.11 A), but move to the posterior region in the overlap decoupled scenario (Figure 5.11 B). The SAR map shown in Figure 5.11 C is generated for the case of applying RF pulses determined in the isolated scenario to the case where the E-field distributions were determined from an overlap decoupled scenario. Although SAR values appeared to be lower in this case, the RF power needs to be increased by about 25% to achieve the desired target pattern. To demonstrate the potential error in predicting hot spots resulting from variations in coil construction, Figure 5.11 D shows a SAR map generating by the RF pulses determined for the overlap decoupled scenario (Figure 5.3 B) but applied to coupled E-field distributions (Figure 5.3 C). It can be seen that this SAR distribution is very similar to Figure 5.11 B which uses overlap decoupled fields for both designing the RF pulses and for calculating SAR values. In addition, we searched for the location of the maximum hot spot over the whole phantom and found that in three of the four combinations, the maximum hot spots appeared in the same slice position as the slice of excitation. Figure 5.11 E is for the overlap decoupled scenario and shows where the maximum hot spot appeared in a different slice position. Comparing Figure 5.11 E with B, it can be seen that SAR distribution is very different and the hot spots are at more superficial positions. The slice is located at one leg of the coil element where the E-field intensity is high.

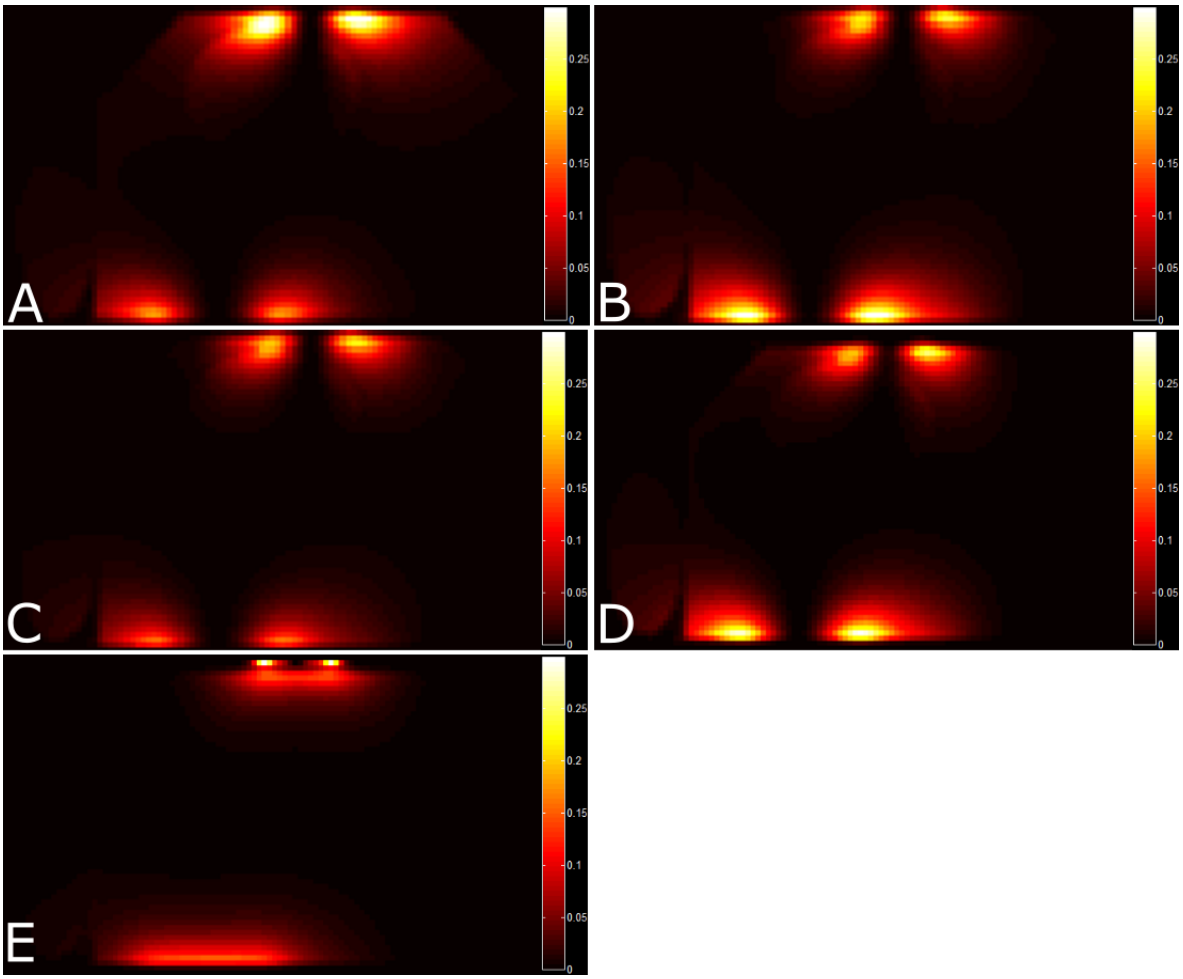

Figure 5.11 Images showing simulated SAR distributions when RF pulses and E-field distributions were in isolation (A) or were overlap decoupled (B). In (C) the RF pulses assumed no coupling but the coil used overlap decoupling and this had some crosstalk between next neighbouring elements. In (D) the RF pulses assumed overlap decoupling, but the coil was not completely overlap decoupled. Image (E) uses the same overlap decoupled condition as for (B) but shows the slice containing the maximum hot spot. Here the colour bar corresponds to the SAR value per voxel. For comparison, the slice position of the SAR maps shown in Figure. 5.11 A through D are identical to that of the small FOV excitation (Figure 5.10).

5.3.4 SAR estimation for inductive coupling model

We showed in Figure 5.10 and 5.11 how RF pulses determined from different coupling conditions affected both Tx-SENSE performance and SAR distributions. Because Equation 5.2 says that SAR depends on pulse length, we expect our results to

be directly affected by the pulse length. Hence, to quantify this effect, the value of SAR per voxel over the phantom (using the eight-channel coil in Figure 5.2 A) was calculated and used to determine global SAR, peak SAR, and the ratio of peak SAR to global SAR. These were calculated as a function of RF pulse length and are shown in Figures 5.12 and 5.13 for various coupling combinations. Figure 5.12 illustrates when both RF pulses and the EM fields are determined in either isolation (scenario 1) or overlap decoupling (scenario 2). It can be seen that the length of the RF pulse (T_p) significantly altered both global and peak SAR estimation. Both coupling scenarios had minimum global SAR and peak SAR values at T_p = 3.9 ms. Notably, global SAR is overestimated by up to 22% at T_p = 2.6 ms when the incorrect coupling condition (isolated) is used, whereas peak SAR using the incorrect coupling condition is underestimated 18% at T_p = 3.9 ms to as much as 35% at T_p = 3.1 ms. Similarly, the ratio of peak SAR to global SAR for the incorrect coupling condition (isolated) case was always underestimated with an error that varies with T_p. Specifically the errors are 20%, 31%, 67%, and 33% for T_p valued of 5.1, 3.9, 3.1, and 2.6 ms respectively.

In reality, determining the parameters of the RF pulses using the overlap decoupled scenario is a more accurate choice than assuming the inductive coupling is zero. However, if a constructed coil generates EM fields slightly different than those predicted by the simulated fields, both small FOV excitation and SAR maps would be adversely altered (see Figure 5.10 and 5.11). Hence, to estimate how the SAR evaluation was affected by the variations between the constructed and simulated coils, we used the coil configuration shown in Figure 5.3 C. Recall that this coil had one coil element that was shifted by 3 mm and thus the overlap decoupling was not perfect. We use the coupled

E-field distributions (from this coil) along with RF pulses determined in the (perfect) overlap decoupled scenario to determine SAR values. These are plotted as a function the RF pulse length in Figure 5.13. For reference, we also show SAR values for the perfect case resulting from overlap decoupled E-field distributions and overlap decoupled RF pulses. The minimum global SAR and peak SAR are at $T_p = 3.9$ ms for both scenarios. The worst case predictions for SAR values are: the global SAR is overestimated by 36% at $T_p = 3.1$ ms; peak SAR is underestimated by 16% at $T_p = 2.6$ ms; and the ratio of peak SAR to global SAR is underestimated by 37% at $T_p = 2.6$ ms.

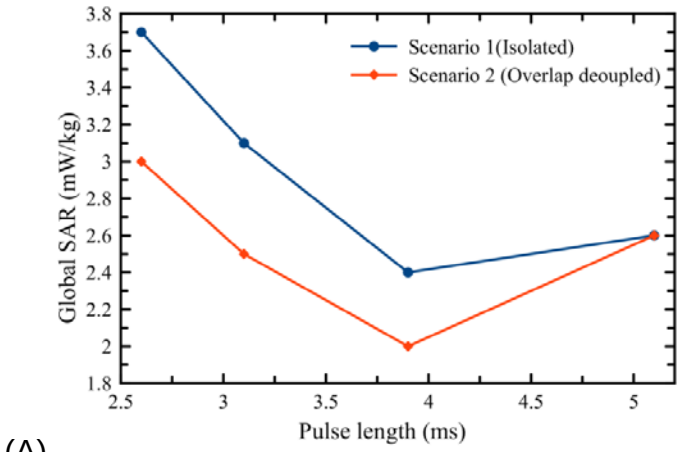

(A)

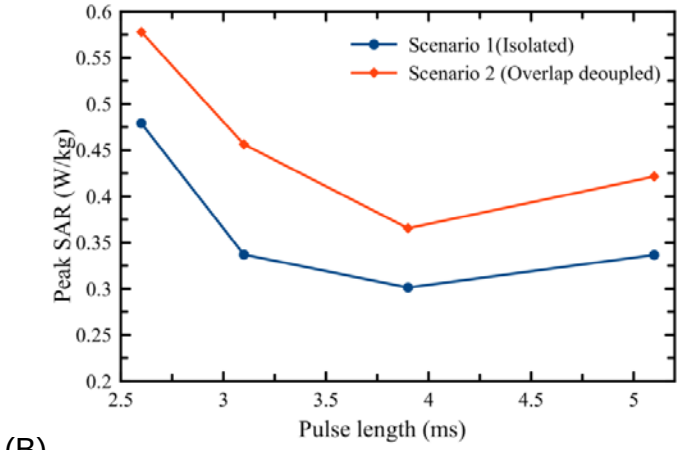

(B)

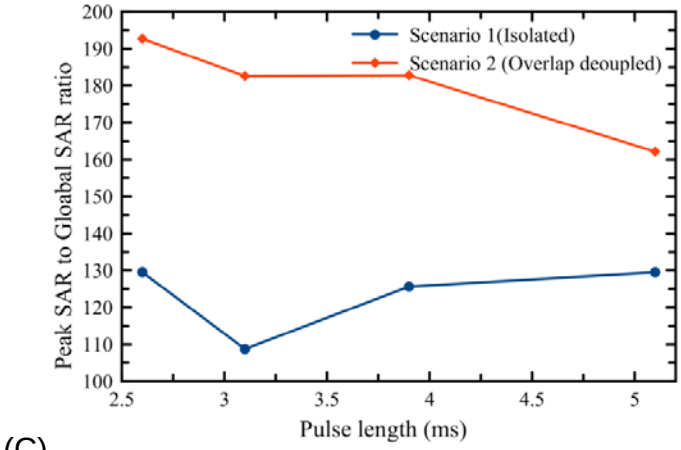

(C)

Figure 5.12 Graphs showing (A) global SAR, (B) peak SAR, and (C) global-to-peak SAR ratio as a function of RF pulse length determined from simulations of the coil shown in Figure 5.2 A and using the coupling scenarios illustrated in Figures 5.3 A and B. Circles use the E-field distributions and RF pulses determined with isolated elements. Diamonds use the E-field distributions and RF pulses determined using overlap decoupled elements.

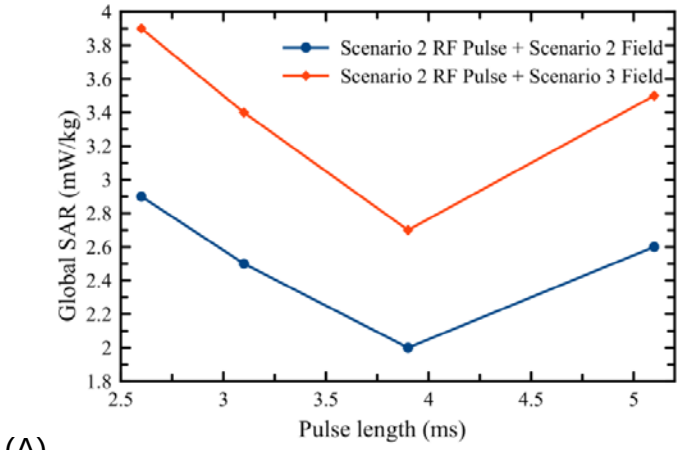

(A)

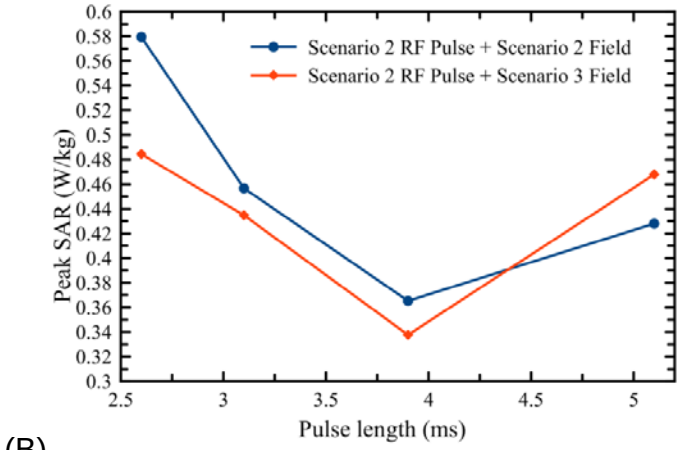

(B)

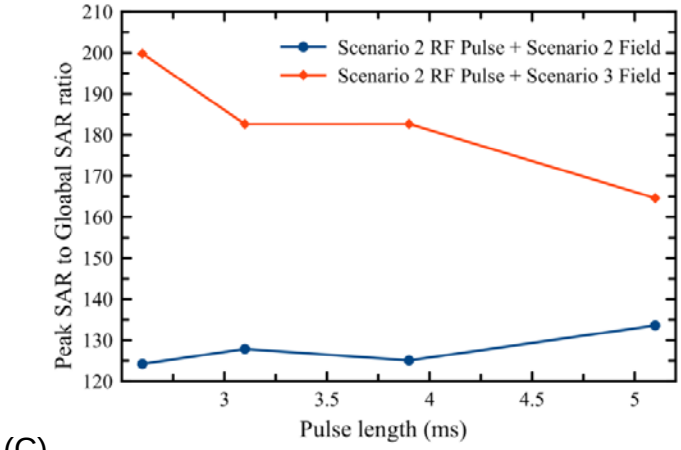

(C)

Figure 5.13 Graphs showing (A) global SAR, (B) peak SAR, and (C) peak-to-global SAR ratio as a function of RF pulse length determined from simulations of the coil shown in Figure 5.2 A. Circles use RF pulses and E-field distributions were determined from overlap decoupled elements illustrated in Figure 5.3 B. Diamonds use RF pulses determined from overlap decoupled elements illustrated in Figure 5.3 B but E-field distributions were determined from coupled elements illustrated in Figure 5.3 C.

5.3.5 Optimizing tilted coil to reducing excitation artifacts

We hypothesize that the B_1^+ maps can be made more symmetric by tilting or bending the coil element. To determine the degree of asymmetry, Figure 5.14 shows the simulated B_1^+ maps of a coil element which is bent or tilted away the surface of the phantom. It can be seen that the B_1^+ maps have varying degrees of asymmetry depending on how the geometry of the coil element was altered. In this case the tilt angle was arbitrarily fixed at 25^o. We expect if the tilt angle is varied, the pattern of the B_1^+ map will remain the same but the field intensity may be different. The results shown in Figure 5.14 are for a single coil element. To show the effect on the entire coil array, the B_1^+ map of the central coil element in the anterior section (see Figure 5.2 B) was sequentially replaced by these B_1^+ maps. To decide which axis to bend the coil along in order to give the best result, we calculated RMS errors between the designed target pattern and the resulting excitation pattern, and show these in Table 5.1. The ideal case would result in a RMS error of 0. These results show the coil element tilted along axis number 1 has the least error. Thus, we choose to use this axis location for further analysis of the tilt angle.

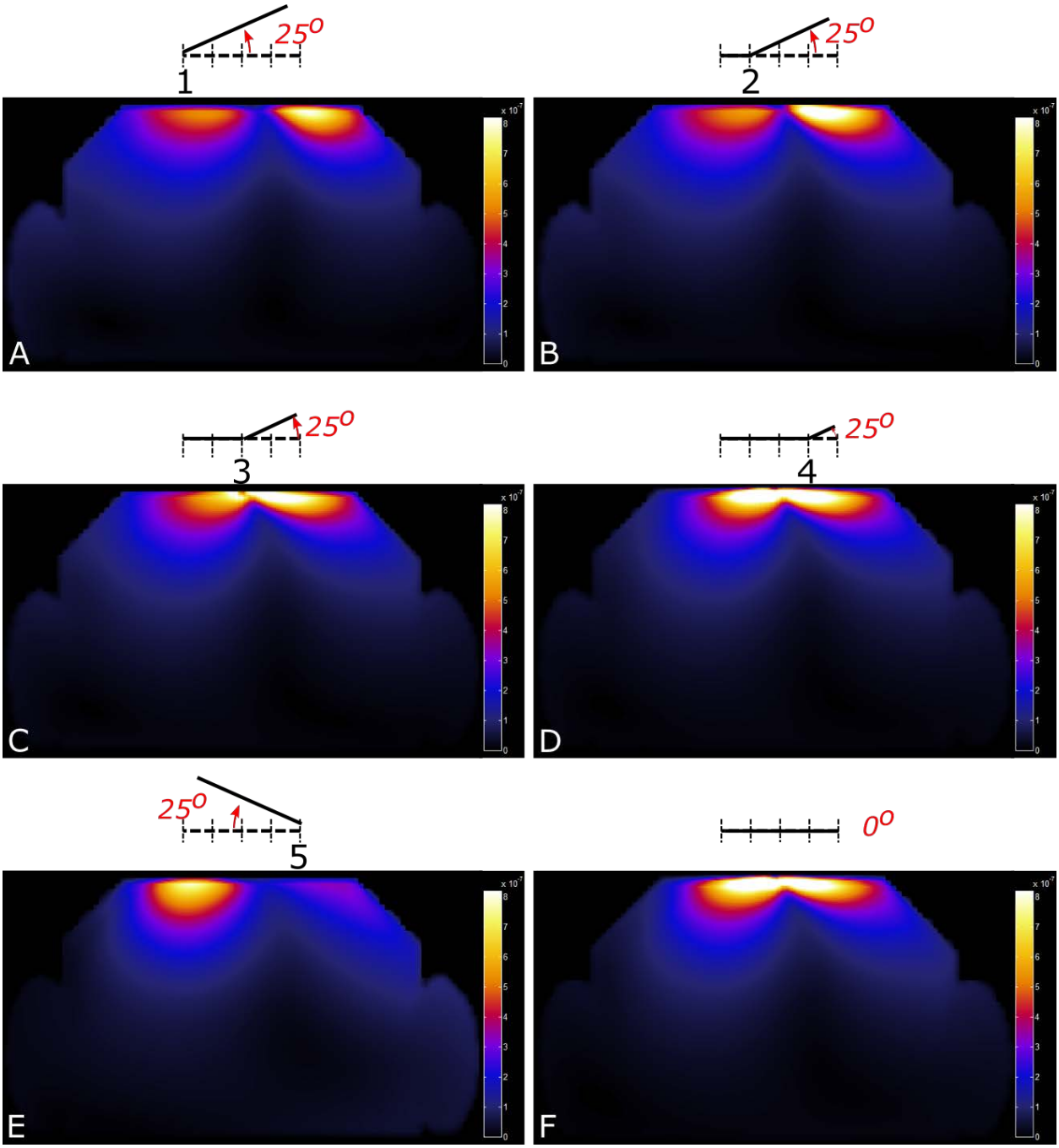

Figure 5.14 Transverse images, from simulations, showing B_1^+ maps of a single loop that is tilted or bent away from the surface of the torso phantom by an angle of 25° as illustrated by the corresponding positions shown above each map. (F) is the reference loop with angle of 0°.

Table 5.1 Normalized RMS errors between the reference coil element (no tilting) and a coil element tilted along five different axes. All eight coil elements were used to excite the target pattern. Lower error is better.

Axis number	Reference	1	2	3	4	5
Normalized RMS error	1.0	0.976	0.988	1.03	0.984	1.332

We have determined the axis along which the coil element was bent or tilted to give the lowest RMS error, i.e. axis 1 illustrated in Figure 5.5. To optimize the tilt angle for reducing the RMS error, the eight-channel transmit array was used to excite a rectangular target pattern and the tilt angle of the central coil element in the anterior section was varied. Figure 5.15 shows the RMS error of the excitation plotted as a function of the tilt angle in the range of 0^o to 45^o. The RMS errors were normalized to the results for an angle of 0^o. It can be seen that the minimum excitation error is at a tilt angle of 10^o and the maximum is at an angle of 45^o. The RMS error gradually increases for a tilt angle larger than 10^o and increases by 14% between 10^o and 45^o. Hence, a tilt angle of 10^o was used for further characterization of the coil design.

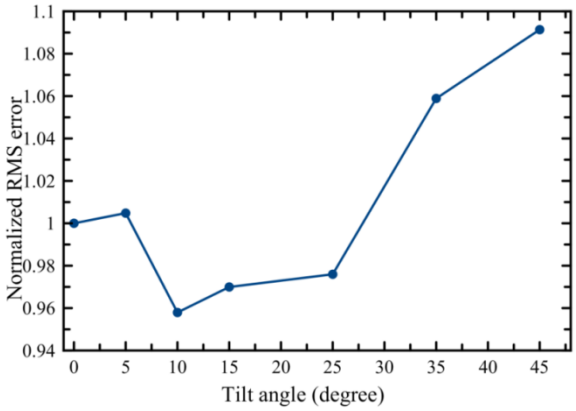

Figure 5.15 Plot showing RMS errors for the eight channel excitation as a single coil element was titled away from the surface of the torso phantom over a range of 10^o to 45^o.

5.3.6 Small FOV excitation using tilted coil design for reducing excitation artifacts

A typical design for a cardiac coil is shown in Figure 5.7 A. Here we determine if the coil shown in Figure 5.7 B is a better design for a transmit array. Each coil element was simulated in isolation and the resulting B_1^+ maps are shown in Figure 5.16. Maps are in the excitation plane of the three coil elements. Using the tilted design, it can be seen that the asymmetry in B_1^+ was reduced. In addition, the regions with higher intensity were reduced compared to the reference design. We used this new design geometry to excite a rectangular target pattern and compared this to the pattern excited by the reference design. Figure 5.17 illustrates the resulting excitations for both designs. Here the two designs show very similar excitation performance within the target pattern region and within regions 1 and 2. But the tilted design reduced a local excitation artifact, which may be related to SAR hot spots, as illustrated by the arrow in Figure 5.17. The RMS error was calculated for Region 5 (close to the transmit array) and the error was reduced by 25% compared to the reference transmit array design geometry (Figure 5.7 A). Horizontal line profiles through the hot spot and the target pattern region of Figure 5.17 are shown in Figure 5.18. It can be seen in the hot spot region (Figure 5.18 A) the tilted design has a lower transverse magnetization of 50% at the location of the hot spot than the reference design. There are no obvious differences in the profiles through the desired target pattern (Figure 5.18 B), which is expected. Hence, this result suggests that by properly tilting the coil elements, the excitation error can be reduced. In addition, local excitation artifacts, which are related to hot spots in SAR estimation, may be reduced.

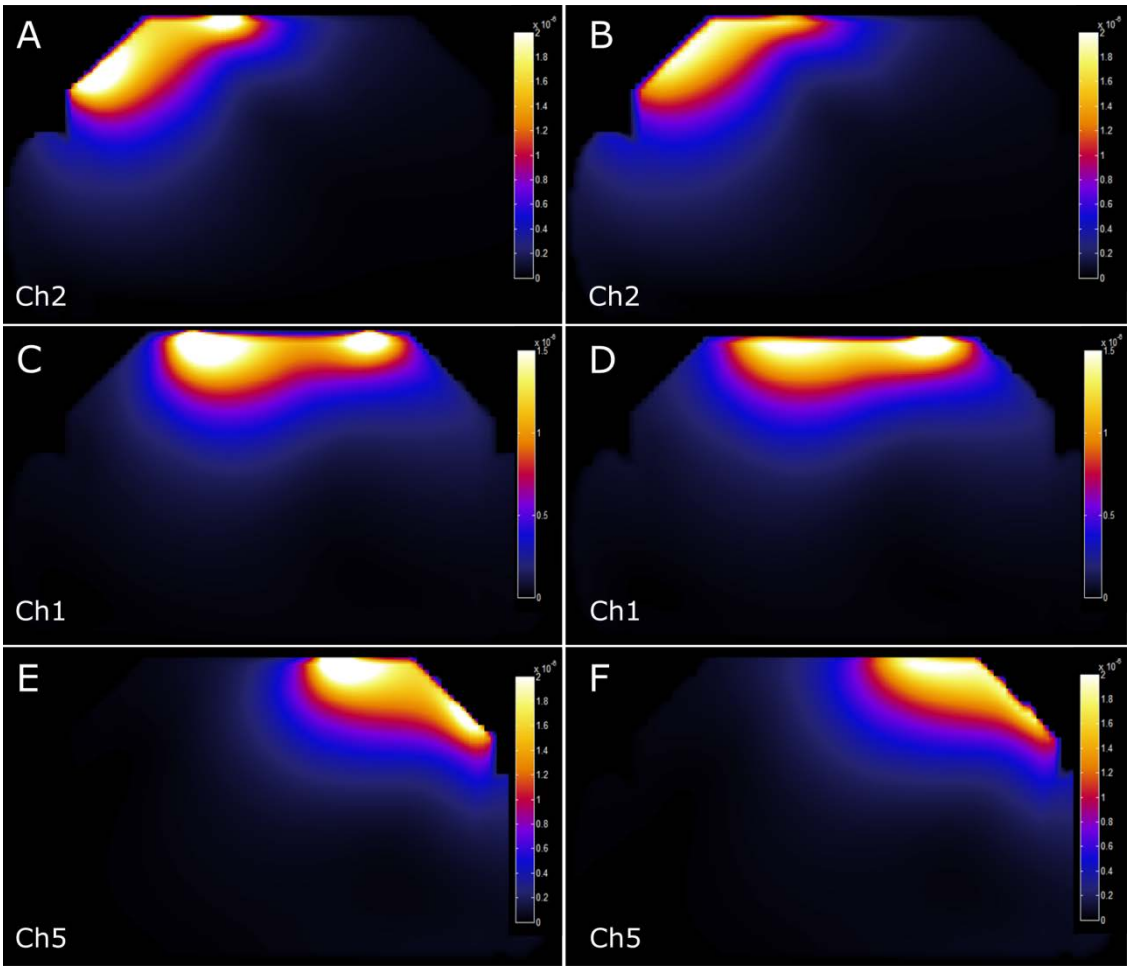

Figure 5.16 Images showing the B_1^+ maps for (left column) the reference design illustrated in Figure 5.7 A and (right column) the tilted design illustrated in Figure 5.7 B. Each coil element (Ch1, 2 and 5) was simulated in isolation.

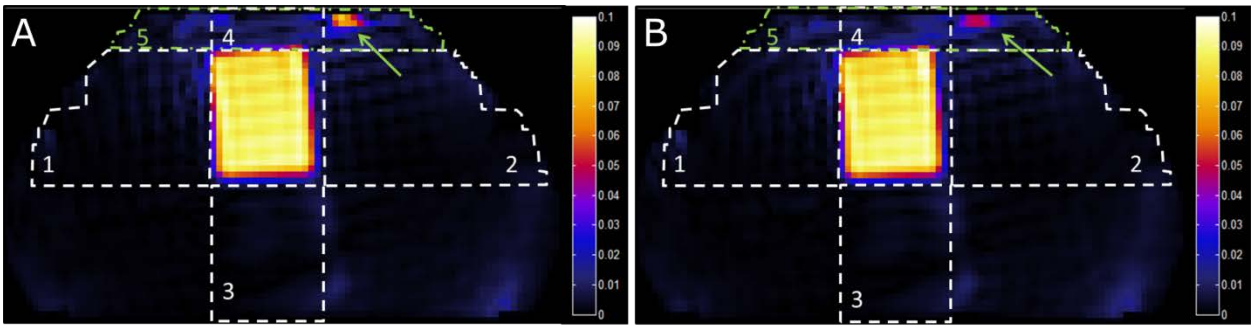

Figure 5.17 Images showing the results of a Bloch simulation for the (A) reference design and the (B) tilted design. This shows the resulting small FOV excitation, which is optimized in regions 1 to 4. The colour bar corresponds to the transverse magnetization normalised to M_0.

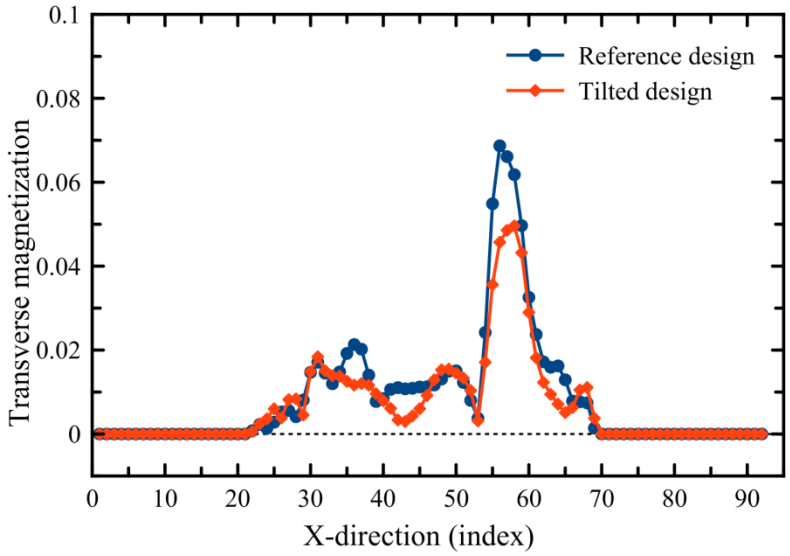

(A)

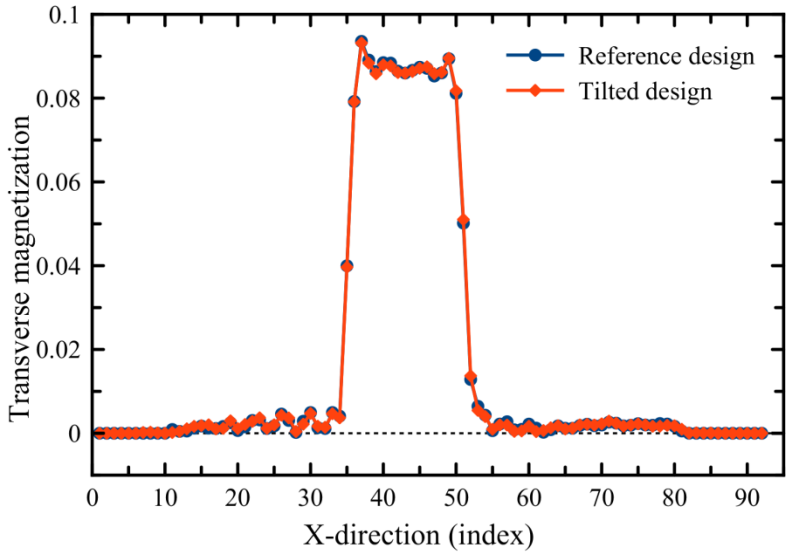

(B)

Figure 5.18 Plots showing horizontal line profiles through Figure 5.17. Here (A) is through the hot spots and (B) is through the target patterns.

5.4 Discussion and conclusions

Design strategies for optimizing the performance of Tx-SENSE with a transmit coil array have been described. We have investigated how inductive coupling affect the small FOV excitation and SAR estimation in different coupling scenarios. Our method was to quantify the impact of those factors and to describe the procedures of coil design. For validation, simulations of B_1^+ maps were compared with the experimental

measurements from the posterior section of the constructed eight-channel transmit coil array shown in Figure 5.4. The measured B_1^+ maps were found to be in good agreement with the simulated ones. This gives us confidence that coupling was properly included in the different simulated scenarios. Simulations of small FOV excitation and SAR estimation showed the predicted results were affected, to different degrees, by how the RF pulses were designed.

5.4.1 B_1^+ mapping for inductive coupling model

Bloch simulations of the small FOV excitation required B_1^+ maps, i.e. sensitivity maps, for each transmit channel. It also required applying RF pulses that were calculated using these B_1^+ maps. An additional constraint was the RF pulses needed to take into account a suitable k-space trajectory to control the image resolution and the pulse length. Hence, the design of RF pulses was affected by many parameters and these impacted the performance of Tx-SENSE. The B_1^+ maps required for Bloch simulations were generated using the different coupling scenarios illustrated in Figure 5.3. These coupling scenarios are the ones most commonly considered during RF coil simulation and construction.

5.4.2 SAR map for inductive coupling model

For the estimation of local SAR, considering inductive coupling while preparing the RF pulses and the associated EM fields is very important. Scaling the RF power is another factor that affects the value of the hot spots. This was illustrated in Figure 5.10 C where the average flip angle inside the target region was lower than the target flip angle. Therefore, the RF power for this combination of RF pulse and B_1^+ maps must be

scaled upwards to achieve the designed target pattern. Consequently, the absolute intensities of the hot spots in Figure 5.11 C seem lower than the other cases, but this is an unscaled SAR distribution and would lead to an underestimation of the local SAR value. Hence, once coupling has been considered, scaling of RF power is vital for accurate SAR estimation.

When we constructed the coil, it was slightly different from the coil model in the simulation because the model was simplified by ignoring some electric components, such as the detuning circuit. Thus, the simulated E-field distributions and the experimental E-field distributions are not expected to be identical. However, Figure 5.11 D shows that even though small variations in coil construction are likely, predictions of the locations of hot spots assuming an overlap decoupled scenario remain valid.

Since the E-field distributions of the coil array cannot be directly measured on a scanner, the performance of Tx-SENSE relied on the accuracy of the B_1^+ maps of each transmit channel. We have constructed an eight-channel transmit coil array and used it to acquire B_1^+ maps with and without coupling between the neighboring coil elements. These B_1^+ maps were then used to validate the coil simulations, and a qualitative agreement was observed. Hence, we used the simulated EM fields for further analysis.

5.4.3 B_1^+ mapping constrain

Here we used a conventional image intensity based technique, i.e. double-angle method [113], for B_1^+ mapping. This makes three assumptions: the relative phases of images must remain unchanged; the applied RF pulses are linear, and magnetization completely recovers during the repetition time. The TR duration was very long (i.e. 2000

ms) and each channel acquired two images to obtain a B_1^+ map. Therefore, the major drawback of this method is that the image acquisition time is very long. In addition, off-line post processing is required for calculating the B_1^+ maps. As the number of transmit channels is increased, the double-angle method becomes impractical, especially for in-vivo studies. Hence, for future work, a rapid B_1^+ mapping technique should be developed and implement for clinical use.

5.4.4 Small FOV excitation using tilted coil design for reducing excitation artifacts

We have validated the simulated B_1^+ maps for different coupling scenarios. We found different degrees of excitation error for Tx-SENSE between RF pulses that were determined with or without considering inductive coupling as shown in Figure 5.10 A and B. These results support our hypothesis that the inductive coupling would alter the B_1^+ map. Thus, during RF coil simulation, a coil element should be simulated when all coil elements are present. This observation agreed with that of Padoromo et al. [116], who investigated a whole-body coil. In addition, our modifications to the individual array element geometries, by tilting or bending them, resulted in more symmetric B_1^+ maps, and hence reduced excitation artifacts, in our case by 25%. In the future, more experimental validations are required.

A limitation for this comparison is the true input power of the scanner is not displayed to the user. The input power of the simulation was fixed at 1 Watt, but the transmit power of the MR must be much higher. Therefore, the amplitudes of the simulated and measured B_1^+ maps cannot be directly compared. However, the qualitative agreement between the simulations and measurements suggests that the

simulated field is able to appropriately incorporate the coupling information. Therefore, the simulations were used for further analysis of coil design.

5.4.5 SAR estimation for inductive coupling model

We have shown the necessity of incorporating mutual inductance coupling in simulating transmit arrays used for Tx-SENSE. If the coupling effect is ignored, the prediction of hot spots can be wrong. We found SAR values varied with various lengths of RF pulses as demonstrated in Figure 5.12. These results showed that with incorrect coupling, global SAR was overestimated by as much as 23%, peak SAR underestimated by as much as 35%, and the ratio of peak-to-global SAR underestimated by as much as 68%. For any pulse length, the percentage difference of SAR values between the two coupling scenarios is significant. The order of the percentage difference agreed with published findings for a whole-body coil where the SAR values were over or underestimated by 20~40 % [116]. If the constructed coil array was slightly different from the simulation model for the coupled coil array (see Figure 5.3 C), this leads to an increase from the expected values of global SAR of 36 % and 16% for peak SAR. In addition, the ratio of peak SAR to global SAR was underestimated by as much as 37%. Hence, in the worst case, the prediction error for SAR values was about 20 to 70%. We found that using a higher acceleration (shorter RF pulses) in Tx-SENSE increased SAR error significantly.

Although, the SAR values cannot be easily measured, proper coupling in simulations is absolutely necessary for RF coil designers to optimize the transmit array design for Tx-SENSE and for accurate prediction of peak local SAR distributions. From

the patient safety point of view, the underestimated local SAR prediction is particularly important and may need to be incorporated into the safety plan for any site using a transmit-array.

In summary, we have shown the necessity of taking mutual inductance coupling into account during RF coil simulation and SAR modeling. In addition, we built an eight-channel transmit array coil to validate the simulations of a coupled coil. We proposed a strategy to improve both the asymmetry of B_1^+ maps and to reduce local B_1^+ hot spots, which are strongly related to the local hot spots of SAR. Therefore, using these strategies for transmit array design will improve performance of small FOV excitation and may reduce local SAR hot spots relative to traditional transmit array designs.

Chapter 6: Summary, conclusions and future work

In this chapter, we summarize the contributions of this thesis and the work that can be explored in the future, such as using different ways to represent the source of MRI signals inside a phantom. We illustrate an optimized RF coil design that should be constructed as well as an anthropomorphic tissue-mimicking phantom for experimental verifications.

6.1 Summary

In this thesis we developed new methods to investigate inductive coupling in RF coil simulations and SAR estimation, to reduce excitation artifacts by adapting the concept of negative excitation in RF pulse design and by tilting coil elements. Using these methods we designed an optimized array coil that is both transmit and receive, and is intended for imaging the breasts and the heart. This coil was specifically optimized to the application of small FOV excitation, which allows zooming into a ROI, e.g. high resolution tumor imaging in breasts.

To achieve our goals, we have investigated two main technical tasks in thesis: 1) how to optimize the RF coil and 2) how to improve the RF pulse design for optimizing small FOV excitation. These tasks consisted of three outcomes.

6.1.1 Outcome 1: evaluating the impact of inductive coupling in RF coil simulations

According to the reciprocity theorem, the procedures of RF coil simulations for a receive coil and transmit coil are similar. We hypothesized that the impact of inductive coupling in both types of RF coils should be similar. Hence, we simulated a two-channel

saddle (receive) coil array to evaluate the impact of inductive coupling on the noise correlation matrix. The two-channel coil, which was identical to the simulated model, was constructed to verify the simulation. The coil was measured on the bench for validating tuning and matching. The inductive coupling was varied by altering the overlapping position of coil elements and by using a preamplifier circuit. We found that the noise correlation coefficient was predictable at different overlapping positions when the properly coupled EM fields for all coil elements are used. We also simulated a preamplifier circuit to vary the inductive coupling in simulations. However, due to using an over-simplified preamplifier circuit, the results of measurements disagreed with those of simulations. Although, we spent considerable effort on determining why the results disagreed, we did not find a suitable solution. Unfortunately, this problem still requires more work in the future.

6.1.2 Outcome 2: reducing excitation artifacts through RF pulse and coil design

The theory of designing transmit-SENSE pulses is based on using an under-sampled k-space that leads to excitation artifacts. The shorter the RF pulse length, the more excitation artifacts would expected to be seen. Bloch-simulation was used to predict the excitation result. We proposed an RF pulse design method, which adapted negative excitation artifacts predicted by Bloch-simulation in a previous iteration to pre-compensate artifacts in next iteration. A spatial weighting matrix was incorporated to emphasize the artifacts that appeared on the phase encoding direction of the ROI. The proposed method was tested on homogenous and heterogeneous phantoms to exam its

limitations. The results showed that the proposed method reduced excitation artifacts by about 20% outside the ROI.

We found the excitation artifacts were related to the asymmetry of B_1^+ fields and the local hot spots of SAR. We have shown the excitation artifact could be reduced by improving the RF pulse design method. We proposed a strategy, using tilted coil elements, which generated more symmetrical B_1^+ fields that reduced hot spots. The results showed that by using the proposed strategy in RF coil design, the RMS error was reduced by about 25%

6.1.3 Outcome 3: evaluating and understanding the impact of inductive coupling in SAR

The assumption that the coupling effect is negligible may cause a problem in both excitation performance and SAR estimation, and thus the inductive coupling issue should be investigated and accounted for in the design process [60]. Small FOV excitation requires using non-standard RF pulses. Hence the prediction of local hot spots is difficult. We have shown the inductive coupling changed the noise correlation coefficients for the receive array coil. When we designed a transmit array coil for small FOV excitation, we investigated the impact of different inductive coupling scenarios in SAR estimation, which is associated with patient safety. However, we could not directly acquire E-fields in a phantom. Hence, SAR estimations were made in simulations. We constructed a three-channel phased array coil (posterior section of an eight-channel cardiac coil) to acquire B_1^+ fields to validate the simulated EM fields that incorporated inductive coupling. SAR values were calculated by using the sample E-fields which are weighted by RF pulses. We found SAR values were affected by the length of the RF

pulse. The results showed that in the worst case, the peak SAR values were underestimated by 40% when extremely short RF pulses were applied. Hence, it is important to incorporate the inductive coupling in RF coil simulations.

In conclusion, the results from each outcome provided guidance for RF coil design and also for RF pulse design when optimizing for small FOV excitation. Specifically, we can predict noise correlation coefficients by creating a coupled EM field for each coil element. This is beneficial because it reflects the realistic EM fields, hence the coil performance can be accurately predicted in simulation. We also conclude that inductive coupling must be taken into account in SAR estimation. This is very important and should be considered in the design process for transmit coils. By reducing excitation artifacts through careful pulse design, we can also avoid local SAR hot spots. Finally, we conclude that using tilted coil elements is also able to reduce the excitation artifacts and thus avoid hot spots. The work we have done in this thesis contributes to the progress of clinical breast and cardiac MRI.

6.2 Future work

Chapters 3 to 5 described the work on a transmit/receive array coil. In this section, we describe the possible directions to expand this work.

6.2.1 Inductive coupling simulation

The two-channel coil can be considered as a two-port network: each loop has one feed point (cable attachment). Therefore, network analysis can be applied to show how coupling affects the impedance matrix. Hence, the noise covariance function in Equation 3.5 can be rewritten as

$$\left\langle V_i(t)\, V_j(t) \right\rangle = 4\, k\, T\, \Delta f\, \mathrm{Re}\{Z_{ij}\}$$

where Z_{ij} is the impedance matrix of the two-port network. The impedance matrix can be transformed to or from an S-parameter matrix of the same network. These matrices are complex numbers where the real part of each off-diagonal term of the impedance matrix is related to the shared resistances and the imaginary part is related to the mutual inductances [91], [117], [118]. We measured the impedance matrices in simulations and found that the noise correlation coefficient was highly correlated to the real part of the impedance matrix which suggests that the effect of inductive coupling is reflected in the noise correlation coefficients (see Equation 3.10). Therefore, the simulated impedance matrix is useful for estimating the electric coupling and can be further investigated in the future. For example, we simplified the entire preamplifier circuit by ignoring the transformer circuit. A more realistic model of the preamplifier circuit could be used in the simulation.

The simulation used a simple noise model. We also propose considering an alternative way to model a noise source that is composed of a lot of dipoles randomly distributed in a sample. This method is like a sample in a scanner, where the noise source originates from the sample and a noise voltage is induced in both loops at the same time. Hence, a noise correlation coefficient can be obtained directly without relying on reciprocity. This method might avoid a bias in the noise covariance analysis due to localized high-field intensities near the preamplifier. A more uniform current distribution could also be achieved by placing multiple voltage sources on the driven loop.

6.2.2 Modifications of preamplifier model and two-channel saddle coil

In Chapter 3, we built a two-channel rotating receive coil and used a model of this coil to characterize the prediction of simulations. Specifically, we characterized a simulation method that incorporated coupling between coil elements. The results throughout this chapter showed discrepancies between simulations and experiments of this two-channel saddle coil array. Although we have improved the simulation procedures to more accurately predict the coil, the results only partially validated the concept of including inductive coupling in the simulation. Hence, these results suggest that the simulation cannot perfectly model a real RF coil if the model is overly simplified. In spite of this, the simulation was able to roughly characterize the performance of the coil and consequently it is useful in the initial phase of a design process.

There are some possible modifications of the coil we could use to better match the assumption of the simulation. A preamplifier might not able to perfectly decouple two loops if the inductive coupling is too strong. The decoupling circuit could be adjusted for each coil separation angle to remove any inductive coupling between the loops. Hence, the noise covariance analysis would only be affected by electric coupling from the sample. With this modification, we could compare the new value of noise correlation coefficient to the old measurements. This method might be an alternative approach to characterize the relation between the inductive coupling and noise correlation coefficient.

Another modification would be to replace the saddle loops of the coil with planer loops. Then the loops would translate with respect to each other instead of rotating. The one-dimensional movement might reduce the measurement error. However, this two-

channel planer coil would lack the property of zero electric coupling coefficients (k_e) which we can find in a simulation for the rotating coil. Hence, this coil design would have limitations for the comparison of measurement and simulation.

6.2.3 Construction of the designed eight-channel transmit array

We have designed a two-dimensional planar coil for small FOV excitation. This design is able to use an acceleration factor of 3 in parallel imaging for all directions except superior-inferior direction. This coil consists of an anterior section and a posterior section. In the anterior section, seven hexagonal coil elements are distributed on both sides of a printed circuit board. These are coded as different colors in the Figure 6.1. The small square on each segment represents a capacitor. The posterior section only has single channel, which is a loop-buttery coil. Because the anterior section is predominantly responsible for the excitation, the imaging ROI can be placed at the breast or heart.

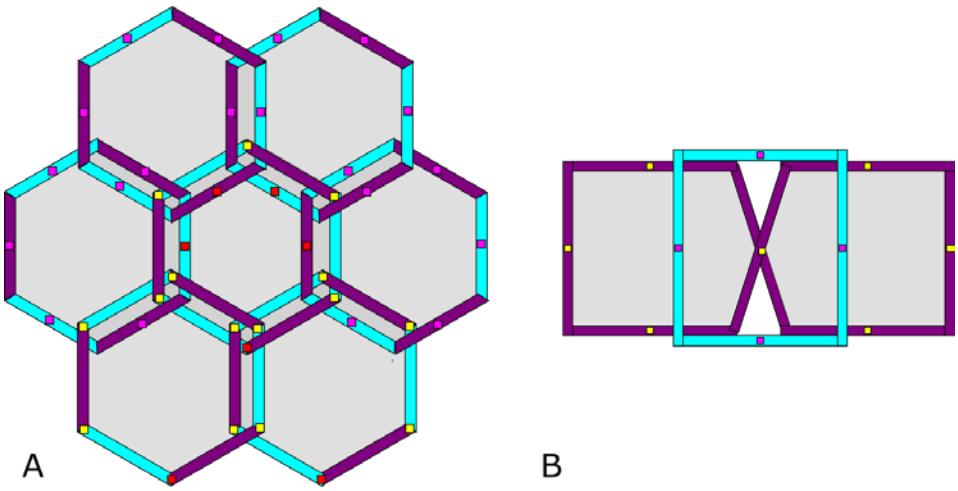

Figure 6.1 Diagram showing the layout of (A) the anterior section of the designed 2D hexagonal coil. (B) The posterior section is a single channel. The coil elements were made from a copper-clad printed circuit board (PCB), we used blue and purple colours to denote the copper traces were on different sides of the PCB. The colour dots were the lumped elements.

6.2.4 Anthropomorphic tissue-mimicking phantom

To push the limitations of the proposed RF pulse design, we tested it with a human model in simulations. The minimal voxel size in the model was a 2 mm^3 cube, hence the spatial resolution of the excited k-space was limited to 2mm. If a submillimeter-resolution model is developed in the future, it is possible to determine the boundary of a small tumor. The validation of the designed RF pulses for small FOV excitation requires an anthropomorphic tissue-mimicking phantom. We designed a phantom, which covers the chest region of the Ella phantom, and is shown in Figure 6.2. The upper surface of the phantom was printed by a 3D printer, and the top and the bottom are sealed with acrylic boards. Two 2-liter water bags are placed in the arm regions. The whole phantom is filled with homogenous fluid. A rugby ball-shaped object in the phantom is used to represent a tumor. It is made of silicon, which gives a different signal than the fluid. If a more realistic phantom is required, different materials should be used to represent different MR properties of each organ in the chest. Using this phantom, we can perform a more detail validation of the RF pulse design and coil.

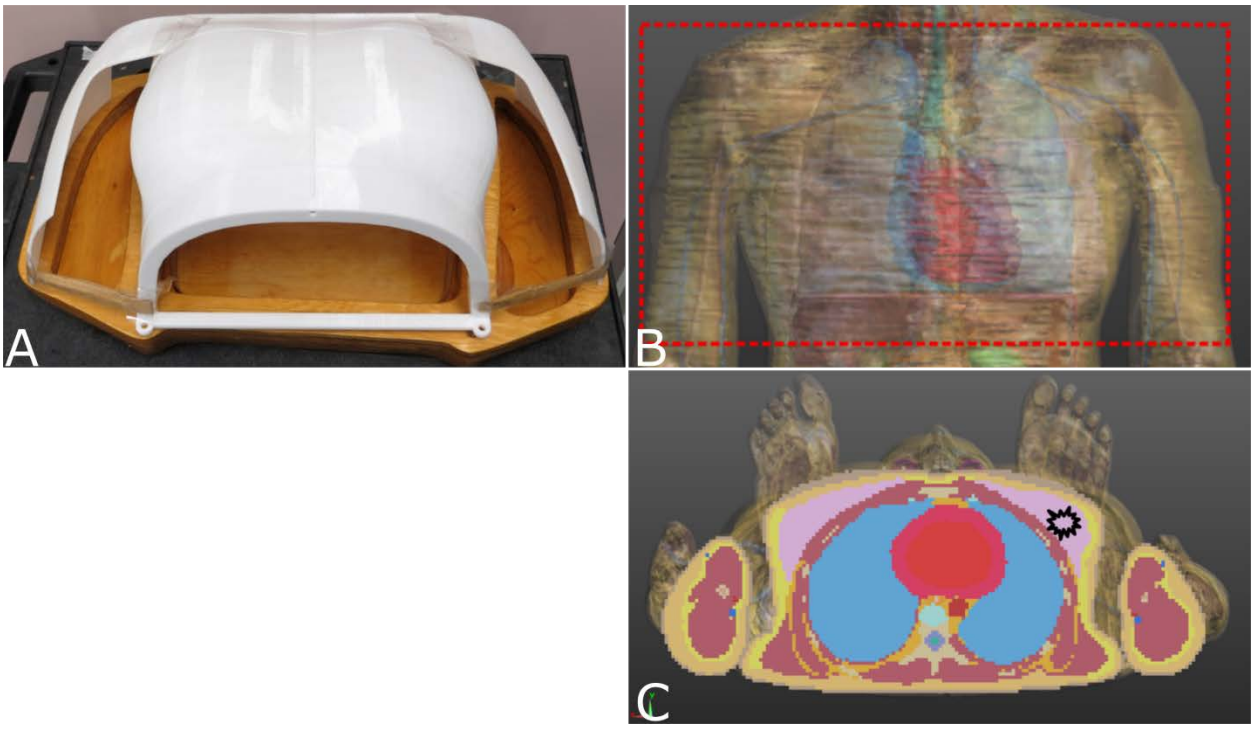

Figure 6.2 (A) photograph showing a phantom that is the chest region of the Ella phantom. (B and C) Corresponding images from simulations.

Most of the work in this thesis was done in simulations and requires further validation on a parallel transmission system with the designed coil and RF pulses. This requires an eight-channel transmit system, which is rare. In our case, the major issue restricting validation measurements was technical problems with our parallel transmission system. We have very limited access to the system and hence it was difficult to obtain required resources to repair the system. In the future, if we can repair the system or find another institution that owns the same system, we would validate our proposed methods.

Appendix I: Electromagnetic modeling for RF coil design in magnetic resonance imaging

Overview

It is important to accurately simulate the electromagnetic (EM) fields that are generated by magnetic resonance coils for safety and design reasons. Numerical methods have been applied to a wide variety of engineering problems for decades [77], [78], [119]–[124], e.g. microwave electronic and wireless communication. This appendix will review fundamental EM theory and discuss two major numerical simulation methods: Finite Element Method (FEM) [125]–[128] and Method of Moments (MoM) [129]–[132], used to solve Maxwell's equations. The other main method, Finite-Difference Time-Domain (FDTD) [80]–[83], [133]–[135], has been discussed in Chapter 2. These methods have various degrees of complexity and accuracy across the whole frequency range of EM radiation. However, only the scenarios relating to magnetic resonance imaging (MRI) will be focused on in this appendix [69], [74]. Specifically, the topics include the development of major numerical methods from physics theory to computational implementations, followed by a discussion of their strengths and weaknesses. Shown at the end of the appendix is the importance of accurately modeling EM in MRI.

Introduction

Relying on the rapid evolution of computer performance, computational electromagnetic methods have become a growing research field and widely applied to numerous electrical devices and systems. One particular area of interest is radiofrequency (RF) coil design in magnetic resonance imaging of humans.

Magnetic resonance primarily measures the signal from nuclei of hydrogen. The Larmor frequency (ω) of the spin of hydrogen nuclei is proportional to the magnetic field strength (B_0) following the relation of $\omega = \gamma B$ where γ is the gyromagnetic ratio. In the special case of low-field MRI, e.g. smaller than 1.5 T, the dimensions of the RF coil are much smaller than the wavelength of the RF field, which satisfies the quasi-static approximation [37], [74]. Then, it is straight forward to accurately transform the complicated RF coil structure and the loaded sample (e.g. the patient) into a simpler equivalent circuit and determine the electric current and voltage in the RF coil based on Kirchhoff's circuit laws. The magnetic field generated by the RF coil is then easily calculated using the Biot-Sarvat law [74].

As the operating frequency increases with increased magnetic field, the corresponding wavelength becomes comparable to the coil size and the assumption of quasi-static approximation starts to breakdown [37]. As a result, the alternative way to model the EM field behavior in the RF coil and the sample is using a full-wave EM analysis to solve the boundary condition problems for Maxwell equations. Several approaches have been implemented for MRI applications [69], [74] (e.g. FEM, MoM, and FDTD approach).

Fundamental Electromagnetic Theory

This section provides a brief review of the relevant EM theory.

Maxwell's equations

All electromagnetic phenomena in matter can be described by Maxwell's equations. Six physical quantities are listed in the following relations [75]:

$$\nabla \cdot D = q_e \quad \text{(Gauss' law-charge)} \tag{I.1}$$

$$\nabla \cdot B = 0 \quad \text{(Gauss' law-magnetic)} \tag{I.2}$$

$$\nabla \times E = -\frac{\partial B}{\partial t} \quad \text{(Faraday's law-induction)} \tag{I.3}$$

$$\nabla \times H = -\frac{\partial D}{\partial t} + J_\sigma + J_{imp} \quad \text{(Maxwell-Ampere law)} \tag{I.4}$$

where the seven physical quantities are

E: electrical field intensity (Volts/meter)

H: magnetic field intensity (Amperes/meter)

B: magnetic flux density (Webers/meter^2)

D: electric flux density or electric displacement field (Coulombs/ meter^2)

q_e: electric charge density (Coulombs/meter^3)

J_σ: electric current density at a given material with conductivity σ (Amperes/meter^2)

J_{imp}: impressed current density which can be the current source used to excite a RF coil (Amperes/meter^2)

The information regarding charge conservation is derived from Equation I.1 and Equation I.4 and is called the equation of continuity as follows:

$$\nabla \cdot J = -\frac{\partial q_e}{\partial t} \tag{I.5}$$

The sources of time-varying electric and magnetic fields in matter

Two Maxwell equations describe the sources of time-depend E- and H-fields. Faraday's law in Equation I.3 states the time-varying magnetic field is the source of induced electric field. The faster magnetic flux changes, the stronger the induced electrical field. In a linear and homogenous medium, the electric displacement field, D, is related to the E-field by $D = \varepsilon \cdot E$ where ε denotes the permittivity or dielectric constant that reflects the capacitance of the medium. In Gauss's law, Equation I.4, the source of

magnetic field is from moving charges in a dielectric material. The induced H-field has a relation $H = \mu^{-1} \times B$ where μ is called permeability or inductivity of the medium. The H-field has contributions from electric polarization associated with the displacement current due to the motion of bound charges. In addition to the polarization term, electric conduction and the impressed current, which are both associated with free moving charges, are sources of the H-field. The last term in Equation I.4, J_{imp}, denotes the impressed current density and can be the given source in the system. To help understand its role in RF coil modeling, the impressed current can be considered as a current flowing in the RF coil resulting from a given voltage source [71], [72], [75].

As an E-field is applied to a medium, positive charges move in the field direction and negative charges move in the opposite direction. The movement of free electric charges forms an electric current inside the medium which is called the conduction current. The corresponding conduction current density, J_σ, is proportional to the applied E-field and can be expressed as $J_\sigma = \sigma \cdot E$ where is the conductivity of the medium. If the conductivity of the medium is not infinite (e.g. lossy materials and conductors), there is energy loss that dissipates in the form of heat in the medium [69], [74]. As a result, the temperature of the medium will rise. For example, the concept of specific absorption rate (SAR) in MRI is associated with the power dissipation in human tissue. The importance of SAR in terms of RF coil modeling will be discussed in a later section.

Time-harmonic fields and boundary value problem

When both the current flowing in the RF coil and the generated fields are oscillating at a single frequency (ω), Equations I.3-4 can be written in complex form [74], [75]. Here only two equations related to the time-varying fields are needed.

$$\nabla \times E = -j\omega B \quad \text{(Faraday's law)} \tag{I.6}$$

$$\nabla \times H = -j\omega D + J_{\sigma} + J_{imp} \text{ (Maxwell-Ampere law)} \tag{I.7}$$

Simply substitute Equation I.6 into Equation I.7 or vice versa to eliminate the electrical or magnetic fields of the coupled partial differential equations. Then, the two decoupled partial differential equations shown below are obtained. The current densities are the sources of the electrical and magnetic fields [132].

$$\nabla \times (\nabla \times E) - \omega^2 \mu \varepsilon E = -j\omega\mu(J_{\sigma} + J_{imp}) \tag{I.8}$$

$$\nabla \times (\nabla \times H) - \omega^2 \mu \varepsilon E = \nabla \times (J_{\sigma} + J_{imp}) \tag{I.9}$$

In other words, a set of unique solutions can be found for EM fields by solving either coupled or decoupled partial differential equations in the time or frequency domain only if the boundary conditions are satisfied. The problem regarding finding the EM fields generated by MRI RF coils is expressed by Equations I.8-9 and is called the boundary value problem [69].

Numerical methods

The EM fields obtained by solving the boundary value problem are used for further RF coil performance evaluation and SAR analysis. Because RF coils and a loaded human tissue model have complicated geometry, analytical solutions cannot always be found. Often, analytical solutions are not suitable for RF coil design [69], [74]. Thus,

approximated solutions must be found using numerical methods. The FDTD method has been discussed in chapter 3. Here we described two other methods: finite element and method of moment.

Finite element method

The finite element method (FEM) was initially developed for analyzing structural and material problems in civil and mechanical engineering in the 1940s. But it wasn't applied to EM problems until the 1960s [125], [136]. Similar to the FDTD method, the FEM is a numerical method for finding an approximate solution to the differential form of Maxwell's equations, but in the frequency domain.

For any EM problem, the system equations can be expressed by a linear system $L[F] = s$, where L is the differential operator, F is the unknown field function to be found in a domain V and s is the driving source function in the system. In general, the FEM subdivides the solution domain into small elements where the solution domain F is approximated by a series of basis functions $\tilde{F} = \sum_{j=1}^{n} N_j f_j$ and $L(N_1 f_1 + N_2 f_2 + L + N_n f_n) = s$. Here N_j are the basis functions and f_j are the unknown coefficients to be determined. By replacing F with $\tilde{F}$, the residual $r = L[\tilde{F}] - s$ is formed and should be minimized. To find the best approximate solution, the weight residual method is used to enforce the condition $R_j = \int_V w_j r \, dV = 0$ where W_j is the weighted function at point j and R_j is the weighted residual integral which can be expressed in matrix form:

$$\begin{bmatrix} \langle w_1, L(f_1)\rangle & \langle w_1, L(f_2)\rangle & \cdots & \langle w_1, L(f_n)\rangle \\ \langle w_2, L(f_1)\rangle & \langle w_2, L(f_2)\rangle & \cdots & \langle w_2, L(f_n)\rangle \\ \vdots & \vdots & \cdots & \vdots \\ \langle w_n, L(f_1)\rangle & \langle w_n, L(f_2)\rangle & \cdots & \langle w_n, L(f_n)\rangle \end{bmatrix} \begin{bmatrix} N_1 \\ N_2 \\ \vdots \\ N_n \end{bmatrix} = \begin{bmatrix} \langle w_1, L(f_1)\rangle \\ \langle w_2, L(f_2)\rangle \\ \vdots \\ \langle w_n, L(f_n)\rangle \end{bmatrix} \Rightarrow [A][x] = [B] \quad \text{(I.10)}$$

If the basis functions are chosen for the weighting functions, the method is called Galerkin's method [78], [121], [125], [136]. The unknown basis functions, [x], are solved by matrix inversion and the values of the basis functions are applied to determine the solution field of the approximation.

The FEM finds the coefficients of basis functions using the following steps which are discussed in detail.

1. Formulating the governing functions of the system
2. Discretizing the solution domain V
3. Approximating the solution by an expansion using a finite number of *basis functions*
4. Solving the system equations obtained

Governing functions

In the time-harmonic problem, the H-field is either eliminated in Equation I.6 to get the following partial differential equation for the E-field or the E-field is similarly eliminated in Equation I.7 to obtain the equation for the H-field.

$$\nabla \times (\nabla \times E) - k_0^2 \varepsilon_r E = -jk_0 Z_0 J \quad \text{(I.11)}$$

where $\varepsilon_r = \varepsilon/\varepsilon_0 - j\sigma/\omega\varepsilon_0$ and ε_0 is the permittivity in free-space. Here $k_0 = \omega \times (\mu_0 \varepsilon_0)^{1/2}$ and $Z_0 = (\mu_0/\varepsilon_0)^{-1/2}$ represent the wave number in free space and the intrinsic impedance respectively [69], [74]. Instead of solving the equation directly, the problem is reformulated into a weak form to find a solution that is only satisfied in the integral of

the strong form over the computational domain. That is, the equation of the problem is reformulated as

$$\iiint_V \left[(W_i \cdot \nabla \times (\nabla \times E) - k_0^2 \varepsilon_r W_i \cdot E \right] dV = -jk_0 Z_0 \iiint_V W_i \cdot J_{imp} dV \tag{I.12}$$

where W_i is a weighting function that also satisfies the boundary condition of the original problem and V represents the volume of interest where fields are to be determined. Applying Green's theorem and a vector identity, Equation I.12 is rewritten as

$$\iiint_V \left[(\nabla \times W_i) \cdot (\nabla \times E) - k_0^2 \varepsilon_r W_i \cdot E \right] dV + jk_0 \iint_S (\hat{n} \times W_i) \cdot (\hat{n} \times E) dS = -jk_0 Z_0 \iiint_V W_i \cdot J_{imp} dV \tag{I.13}$$

which is the system equation to be solved [69], [74].

Domain discretization

The entire computational domain is discretized into a number of small elements with varying sizes and shapes. The elements are non-overlapping and are connected at vertices called nodes [125]. Adjacent elements can also share edges or faces. Figure A.1 shows an example of the discretization of a human tissue model where the different colour objects denote different types of sub-objects. Figure A.2 shows various types of elements for different dimensional problems. The basic triangular (3 nodes) and high order element, such as tetrahedral (4 nodes) elements are usually the default elements in 2D and 3D EM problems, respectively. The general properties of domain discretization include: geometry conformity that should sufficiently approximate the region of interest, high mesh density to reduce the discretization error, and a good element quality that includes ensuring the distortion is minimal and the aspect ratio is reasonable [128], [137].

In commercial software, the mesh is automatically generated. However, it is necessary to specify the type of mesh desired and the characteristics of the mesh before the mesh is formed. The mesh properties have a direct impact on the accuracy of the solution and the total computational time. Here the information regarding the mesh should include: 1) the type of the element and the number of nodes per element, 2) the minimum sizes of the elements, and 3) the location of different materials in the object [128], [137]. The procedure to construct the mesh starts with node generation along the edges of the object. This is followed by discretizing the whole boundary of the domain and then forming elements within the object. In general, the accuracy of the FEM depends on the number and sizes of the elements formed.

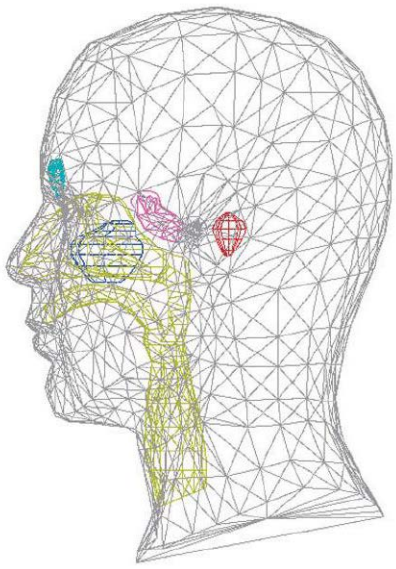

Figure A.1 A FEM mesh of the human head model with tetrahedral elements. Only the surfaces of the elements are shown [69].

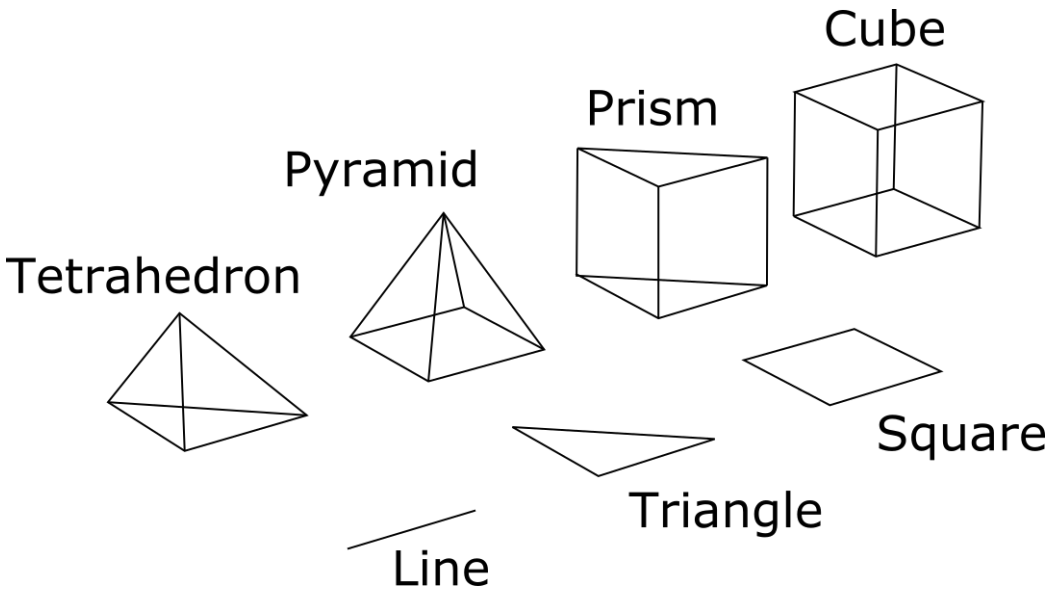

Figure A.2 The basic elements used in FEM: Line segment is for 1D problems, triangle and square elements are for 2D problems, the rest of the high-order elements are for 3D problems.

Approximation of the solution domain

The FEM approximates the solution domain with piecewise continuous functions and then determines the coefficients of the functions that minimize the residual of the weak form of the partial differential equations. In the governing function, Equation I.13, the tangential components of E-fields within each element are interpolated using basis functions [69].

$$E^{//}(\vec{r}) = \sum_{i=1}^{N_{edge}} N_i(\vec{r}) E_i^{//}(\vec{r}) \tag{I.14}$$

where r is the position vector , N_i is the vector basis function associated with edge i, and N_{edge} is the total number of edges on the element. Figure A.3 shows an example of a linear tetrahedral element. One of the six corresponding vector basis functions, referred to as a Whitney function, is given by

$$N_{lk}^{//}(\vec{r}) = L_{lk}(\lambda_l \nabla\lambda_k - \lambda_k \nabla\lambda_l) \quad \text{(I.15)}$$

where λ is the barycentric coordinates for the nodes l and k, and L_{lk} is the length of the edge connecting the nodes. This function guarantees tangential continuity and normal discontinuity of the interpolated field of each element because it has a tangential component only along the associated edge. This feature is not easy to show in tetrahedral elements, thus an example using triangular elements is shown in Figure A.3.

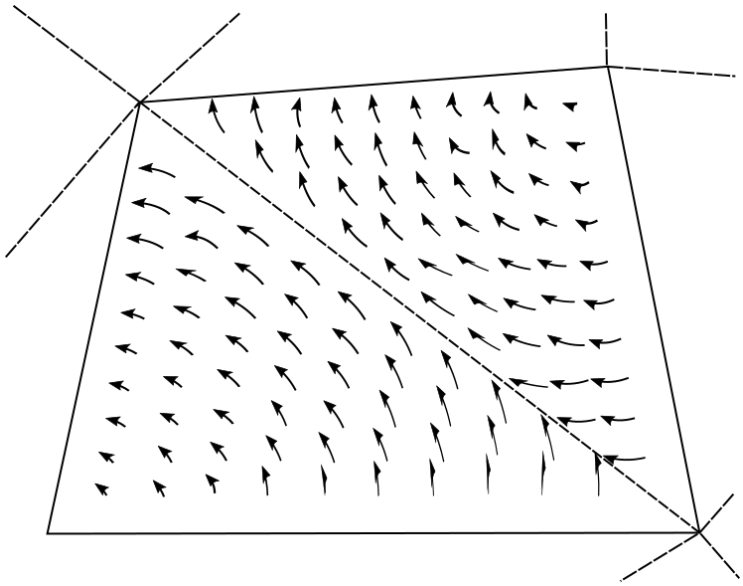

Figure A.3. Two connecting triangular elements share an edge but the vector plots (arrows) of the vector basis function for each element are different. Only the tangential components of the E-fields exit on the edge.

Solution of system equations

Once the E-field within each element is determined, all elements in the solution domain can be assembled to obtain the discretized governing equation [74]:

$$\sum_{j=1}^{N_{edge}} K_{ij}(\vec{r})E_i = b_i \quad \text{(I.16)}$$

and

$$K_{ij} = \iiint_V \left[(\nabla \times N_i) \cdot (\nabla \times N_j) - k_0^2 \varepsilon_r N_i \cdot N_j \right] dV + jk_0 \iint_S (\hat{n} \times N_i) \cdot (\hat{n} \times N_j) dS$$

$$b_i = -jk_0 Z_0 \iiint_V N_i \cdot J_{imp} dV$$

By assuming the weighting function is equal to the basis function, the governing equation can be converted into a matrix form:

$$[K][E] = [b] \tag{I.17}$$

where [E] is a vector of the unknown E-fields, [b] is a vector of the driving source, and [K] is a sparse and symmetric matrix. The non-zero values in [K] correspond to the edges that share an element. Finally, the vector [E] can be solved by using linear algebraic techniques such as Gaussian elimination and LU decomposition of the direct methods or Gaussian-Seidel Jacobi relaxation and conjugate gradient of the iterative methods [82] .

Summary of FEM

The main reason why FEM is widely applied in many aspects of engineering studies is because it is able to model an object with complicated geometric detail and incorporate materials with heterogeneous electromagnetic properties. On the other hand, FEM has the limitation of requiring a very large computational domain. This limitation is similar to the FDTD method when used for an unbounded problem where an absorbing boundary condition is required and high accuracy is specified. Consequently, a large computational domain leads to a long computational time. Parallel computing can sufficiently overcome this issue; however, it is still challenging to create a human tissue model and to generate a mesh with high-order elements (see Figure A.2) for it. Because using these high-order elements increase the complexity of the system matrix.

The FEM-based commercial software packages are HFSS (ANSYS, USA) and Multiphysics (COMSOL, Sweden).

Method of moments

The Method of Moments (MoM) was first introduced by Harrington in the 1960's and is often referred to as the boundary element method [130], which is used in most commercial MoM codes. The MoM is an integral method that calculates the boundary integral equations for Maxwell's equations in the frequency domain.

The MoM analysis steps are identical to the steps for the FEM method. The only difference is that the MoM method solves the field integral equations with Green's functions. Therefore, the system equations are also expressed as L[F] = s but L is an integral operator in the MoM method. In this section only the following topics will be discussed.

1. Representing the geometry as a distribution of an equivalent surface current density and a volume current density in the objects

2. Choosing the basis functions

Governing function

When an excitation is applied to a RF coil loaded with an inhomogeneous object, a surface current density (J_s) will be induced in the coil and a volume current density (J_v) will be induced within the loaded object according to the surface and volume equivalent theorems. The total EM field is the superposition of the fields generated by J_s and J_v,

and expressed as an electric field integral equation (EFIE) and a magnetic field integral equation (MFIE) [69].

$$\begin{aligned} E(\vec{r}) &= -j\omega\mu_0 \iint_S \overleftrightarrow{G}_{e0}(\vec{r},\vec{r}') \cdot J_s(\vec{r}')dS' - j\omega\mu_0 \iiint_V \overleftrightarrow{G}_{e0}(\vec{r},\vec{r}') \cdot J_V(\vec{r}')dV' \\ H(\vec{r}) &= \nabla \times \iint_S G_0(\vec{r},\vec{r}') \cdot J_s(\vec{r}')dS' + \nabla \times \iiint_V G_0(\vec{r},\vec{r}') \cdot J_V(\vec{r}')dV' \end{aligned} \quad \text{(I.18)}$$

where $\overleftrightarrow{G}_{e0}(\vec{r},\vec{r}')$ is the free-space dyadic Green's function for the electric type and $G_0(\vec{r},\vec{r}')$ is the free-space scalar Green's function. $J_V(\vec{r}) = j\omega\varepsilon_0[\varepsilon_r(\vec{r}) - 1]E(\vec{r})$ and ε_r is defined in Equation I.17. Here S denotes the surface of the conducting coil and V denotes the volume of the inhomogeneous object. The surface integral equation is formed by applying the perfect electrical conductor boundary condition to the EFIE. The volume integral equation is formed using the total field generated by J_s and J_v and is rewritten below by replacing the E-field with the electric flux density, D. The governing functions for solving J_s and D are formed by combining the surface and the volume integral equations [69]

$$\begin{aligned} &\hat{n}(\vec{r}) \times \iint_S \overleftrightarrow{G}_{e0}(\vec{r},\vec{r}') \cdot J_s(\vec{r}')dS' + \hat{n}(\vec{r}) \times \iiint_V \overleftrightarrow{G}_{e0}(\vec{r},\vec{r}') \cdot \chi(\vec{r}')D(\vec{r}')dV' = 0, \quad r \in S \\ &\frac{D(\vec{r})}{j\omega\mu_0\varepsilon_0\varepsilon_r(\vec{r})} + \iint_S \overleftrightarrow{G}_{e0}(\vec{r},\vec{r}') \cdot J_s(\vec{r}')dS' + \iiint_V \overleftrightarrow{G}_{e0}(\vec{r},\vec{r}') \cdot \chi(\vec{r}')D(\vec{r}')dV' = 0, \quad r \in V \end{aligned} \quad \text{(I.19)}$$

where $\chi(\vec{r}') = j\omega[\varepsilon_r(\vec{r}) - 1] / \varepsilon_r(\vec{r})$. The MFIE can also be rewritten, but only the EFIE is shown as an example.

Discretization of governing function

In the FEM, the objects in the whole computational domain are subdivided into small elements. However, in MoM only the surface of the RF coil is discretized with 2D

elements and the inhomogeneous object is discretized with 3D elements. Free space is ignored.

Similar to the FEM, the approximate J_s and D for MoM are expanded by divergence-conforming basis functions.

$$J_s(\vec{r}') = \sum_{n=1}^{N_s} J_n f_n^s(\vec{r}')$$
$$D(\vec{r}') = \sum_{n=1}^{N_v} D_n f_n^v(\vec{r}') \quad \text{(I.20)}$$

where J_n is the current flow in the RF coil surface, and f_n^s and f_n^v are the basis functions. The Rao-Wilton-Glisson (RWG) and the Schaubert-Wilton-Glisson (SWG) basis functions are defined in Equation I.21 and Equation I.22 for triangular elements and tetrahedral elements, respectively.

RWG basis function for triangular elements [69], [78], [121], [130]:

$$f_n^s(\vec{r}') = \begin{cases} \frac{l_n}{2A_n^+}\rho_n^+, & \vec{r}' \in T_n^+ \\ \frac{l_n}{2A_n^-}\rho_n^-, & \vec{r}' \in T_n^- \end{cases} \quad \text{(I.21)}$$

where T_n^+ and T_n^- are two triangular elements with areas of A_n^+ and A_n^- and share an edge with a length of l. The terms ρ_n^+ and ρ_n^- are the position vectors as shown in Figure A.4. The plus and minus signs present the vector direction associated with the shared edge.

SWG basis function for tetrahedral elements[129]:

$$f_n^v(\vec{r}') = \begin{cases} \frac{a_n}{3V_n^+}\rho_n^+, & \vec{r}' \in T_n^+ \\ \frac{a_n}{3V_n^-}\rho_n^-, & \vec{r}' \in T_n^- \end{cases} \quad \text{(I.22)}$$

where T_n^+ and T_n^- are a pair of tetrahedral elements with volumes V_n^+ and V_n^- and share a common face with an area a_n. The terms ρ_n^+ and ρ_n^- are the position vectors as shown in Figure A.5. The important feature of RWG and SWG functions is that they have no normal component to other edges or faces, but have a constant normal component on the shared edge or face. This feature ensures the continuity of J_s and D.

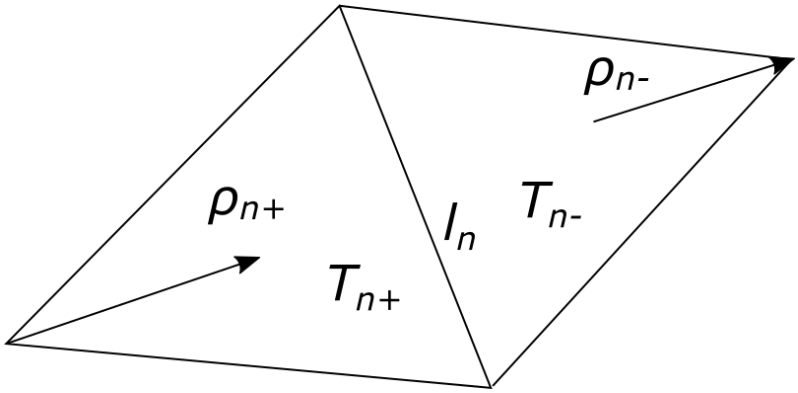

Figure A.4 The RWG basis function for triangular elements

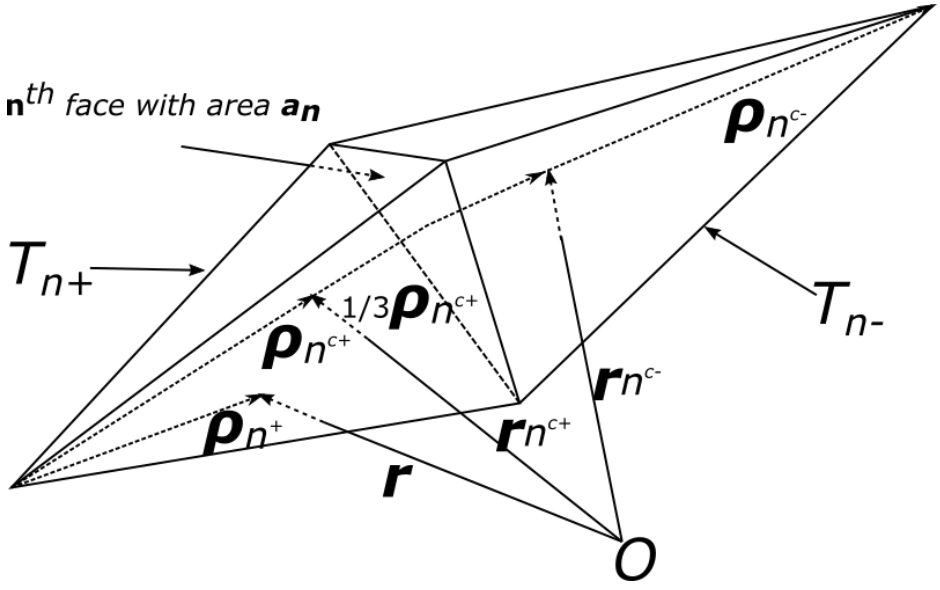

Figure A.5 The SWG basis function for tetrahedral elements

Excitation with voltage source

A voltage source is necessary for driving the current flow in the RF coil. Figure I.6 shows a delta-gap voltage source model used with a RWG basis function in MoM [137]. A voltage source is impressed across two triangular elements. Since RWG functions ensure the normal component along the common edge is equal to one, the gap d should be close to zero. The impressed E-field produced within the gap is expressed in Equation I.23. From Equation I.23, it is clear that that the E-field within the gap is equal to the negative of the norm component of impressed voltage

$$E^i = \lim_{d\to 0} \frac{-V_i}{d}\hat{n} = -V_i\delta(h)\hat{n} \tag{I.23}$$

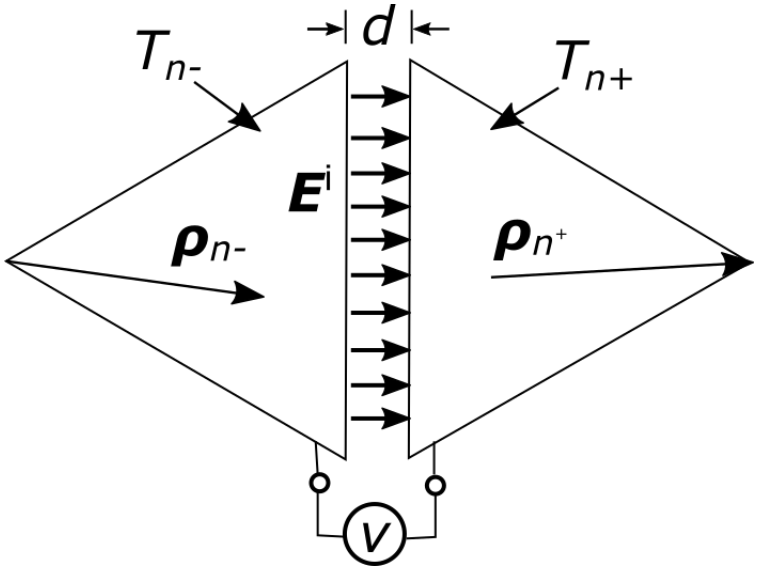

Figure A.6 The delta-gap voltage source model

Solution of system equations

To generate the system equations, substitute Equations I.20-22 into Equation I.19 and incorporate the impressed E-field as the driving source. By assuming the weighted

functions are $\hat{n}\times f_m^s(\vec{r})$ and $f_m^v(\vec{r})$, the governing functions are converted to the following matrix form [84], [138]

$$\begin{bmatrix} Z^{ss} & Z^{sv} \\ Z^{vs} & Z^{vv} \end{bmatrix}\begin{bmatrix} J \\ D \end{bmatrix} = \begin{bmatrix} b^s \\ b^v \end{bmatrix} \tag{I.24}$$

where

$$Z_{mn}^{ss} = \iint_S f_m^s(\vec{r})\iint_S \overleftrightarrow{G}_{e0}(\vec{r},\vec{r}')f_n^v(\vec{r}')dS'dS,\ \ m=1,2,\cdots,N_s,\ \text{and}\ \vec{r}\in S$$

$$Z_{mn}^{sv} = \iint_S f_m^s(\vec{r})\iiint_V \overleftrightarrow{G}_{e0}(\vec{r},\vec{r}')\cdot\chi(\vec{r}')\cdot f_n^v(\vec{r}')dV'dS,\ \ m=1,2,\cdots,N_s,\ \text{and}\ \vec{r}\in S$$

$$Z_{mn}^{vs} = \iiint_V f_m^v(\vec{r})\iint_S \overleftrightarrow{G}_{e0}(\vec{r},\vec{r}')f_n^s(\vec{r}')dS'dV,\ \ m=1,2,\cdots,N_V,\ \text{and}\ \vec{r}\in V$$

$$Z_{mn}^{vv} = \frac{1}{j\omega\mu_0\varepsilon_0}\iiint_V \frac{f_m^v(\vec{r})\cdot f_n^v(\vec{r})}{\varepsilon_r(\vec{r})} + \iiint_V f_m^v(\vec{r})\cdot\iiint_V \overleftrightarrow{G}_{e0}(\vec{r},\vec{r}')\cdot\chi(\vec{r}')\cdot D(\vec{r}')dV'dV,\ \ m=1,2,\cdots,N_V,\ \text{and}\ \vec{r}\in V$$

$$b_m^s = \iint_S f_m^s(\vec{r})\cdot E(\vec{r})dr,\ m=1,2,\cdots,N_s$$

$$b_m^V = \iint_S f_m^V(\vec{r})\cdot E(\vec{r})dr,\ m=1,2,\cdots,N_v$$

The elements in the above matrix involve matrix-vector multiplication corresponding to Green's functions, thus it has a complicated implementation. The solution of the matrix can be solved using the linear algebra techniques previously mentioned in the FEM section. However, evaluating the integrals in Equation I.24 is challenging due to the singularity of the matrix when the $|r-r'|$ term in the Green's function approaches zero [69], [121], [138]. New techniques, including the fast multipole method and the adaptive integral method, can handle this problem and also reduce the required computational resources [69], [121].

Summary of MoM

The major advantage with MoM is that only the objects of interest in the model are discretized, which leads to a significant reduction in the number of unknowns in the matrix. Therefore, it is useful for radiation and scattering problems. In addition, in the free-space region an absorbing boundary condition is not required. As a result, there is no truncation error in the MoM. The drawback of the MoM is the complexity of algorithm implementation because the solutions of the system equations use the Green's function where singularities need to be handled [69]. The system equations become very complicated when an inhomogeneous object is used. Therefore, solving the system equations is computationally expensive. An example of a MoM-based software is the commercial package from FEKO (EM Software & Systems Inc., South Africa).

Comparison of FDTD, FEM, and MoM

The basic theories of the FDTD, FEM, and MoM methods have been discussed. The fundamental difference in these numerical methods is that the boundary value problems for Maxwell's equations are expressed in different forms. For the frequency domain solvers, the MoM discretizes the boundary integral equations. In contrast, the FEM method discretizes the partial differential equations. For the time domain solver, the FDTD method directly discretizes the differential form of Maxwell's equations. Thus, the numerical properties associated with discretized equations vary with the applied method [121]. The remaining question is which method is the best in terms of MRI RF coil simulation. To answer this question the numerical properties including computational complexity, solution accuracy and any error will be compared over three methods in this section.

Both MoM and FEM convert the linear equations of the boundary value problem into a matrix form. Therefore, the accuracy of MoM and FEM rely on how the system equations are solved. In the numerical analysis, the way in which inaccuracies affect the solution is characterized by the condition number. The condition number of a matrix affects convergence for iterative methods [139] and the accuracy for direct matrix inversion methods. The MoM has a higher condition number than the FEM [121]. This suggests the matrix in the MoM is ill-conditioned and is almost singular. Thus, the solution of matrix inversion is inaccurate but its iterative process convergences faster than the FEM. In contrast, the FEM matrix has a low condition number, and is considered a well-conditioned matrix [140]. The solution obtained using a direct matrix inversion method is accurate. If computational resources are not an issue, direct methods are good alternatives.

The method of solving the discretized equations in FDTD is fundamentally different from that of MoM and FEM. Instead of solving a linear system, the conventional FDTD solves its discretized equations in a leap-frog manner. Once the grid of the FDTD is built, the relationship between the time step and the spatial step is restricted by the CFL criterion. Therefore, the FDTD method is not easily compared to the MoM and the FEM with respect to the discretized equations.

Considering the system equation has N number of unknowns, the computational complexities in terms of memory cost and CPU time in MoM, FEM, and FDTD are $O[N^2]$, $O[(\Delta x)^{3/2}]$, and $O[(\Delta x)^{4/3}]$ respectively [69], [141], [142]. Although the number of unknowns in MoM is less than that for the FEM and FDTD method, MoM shows the highest computational complexity which comes from using Green's functions and RWG

and SWG basis functions. In FEM, the increased computational cost is due to the high-order elements used (e.g. pyramid). The FDTD method is the easiest method to implement with a reliable accuracy. That is the reason why the FDTD method is a popular choice. Furthermore, if an inhomogeneous object is simulated using the MoM and FEM, the computational complexities increase significantly [69].

Accuracy is affected by various errors that are summarized here. When a continuous function is discretized, a truncation error is unavoidable in any numerical technique [121], [124]. Because an absorbing boundary condition is not required, the MoM does not suffer from the truncation error associated with the wave reflection from the truncated boundary [69]. A numerical dispersion error introduced in FDTD and FEM diminishes the accuracy as well. Moreover, round-off error contributes to the solution when a computer is used for all methods [79], [81], [135].

In theory, the MoM, FEM, and FDTD method have reasonable accuracies. However, the MoM is less flexible than the other methods in terms of code implementation because the boundary integral equations vary with the object types (e.g. surface or volume). The trade-off between flexibility and accuracy suggests the MoM has best accuracy among these methods [121], [124]. It has been discussed here that the MoM shows the highest accuracy and the FDTD is least accurate [121], [124]. When the need for computational resources is taken into account, the answer to the question of which method is the best choice for MRI RF coil simulations is still open.

Conclusions

This appendix, along with Chapter 2, reviews the three most popular numerical methods, FDTD, FEM and MoM used for the electromagnetic modeling of RF coils for design and related safety issues. The advantages and the weakness of each method, from the derivation of the physics expressions of the boundary value problems to the computational implementations, were discussed. These three methods all have promising accuracies, but show different levels of computational complexity. Although the FDTD method, as a time-domain solver, may contain additional error (less accurate) compare to the other methods associated with dispersion, it is much simpler to implement and is able to handle inhomogeneous human tissue objects more easily than FEM and MoM. So is often the method of choice in MRI simulations involving inhomogeneous human tissue models. Moreover, among all numerical methods, FDTD is recommended by the International Electro-technical Commission for RF coil design in MRI SAR measurements in human tissue models [13].

REFERENCES

[1] “The 10 leading causes of death, 2013,” *Statistics Canada*.

[2] “Economic Burden of Illness in Canada, 2005-2008,” *Public Health Agency of Canada*.

[3] “2009 Tracking Heart Disease and Stroke in Canada - Public Health Agency of Canada,” Jun. 2009.

[4] Canadian Cancer Society, “What is breast cancer?,” *www.cancer.ca*. [Online]. Available: http://www.cancer.ca/en/cancer-information/cancer-type/breast/breast-cancer/?region=mb. [Accessed: 28-May-2017].

[5] American Cancer Society, “Breast Cancer.” [Online]. Available: https://www.cancer.org/cancer/breast-cancer.html. [Accessed: 28-May-2017].

[6] H. Gray, *Anatomy of the Human Body*. Lea & Febiger, 1918.

[7] L. A. Torre, F. Bray, R. L. Siegel, J. Ferlay, J. Lortet-Tieulent, and A. Jemal, “Global cancer statistics, 2012,” *CA. Cancer J. Clin.*, vol. 65, no. 2, pp. 87–108, Mar. 2015.

[8] E. J. Kim, B. J. Kang, S. H. Kim, I. K. Youn, J. E. Baek, and H. S. Lee, “Diagnostic Performance of and Breast Tissue Changes at Early Breast MR Imaging Surveillance in Women after Breast Conservation Therapy,” *Radiology*, p. 162123, Apr. 2017.

[9] B. Branson, *Mammography Machine (National Cancer Institute)*. 1991.

[10] National Cancer Institute, “Breast Cancer Risk in American Women,” *National Cancer Institute*. [Online]. Available: https://www.cancer.gov/types/breast/risk-fact-sheet. [Accessed: 28-May-2017].

[11] W. DeMartini, C. Lehman, and S. Partridge, “Breast MRI for Cancer Detection and Characterization,” *Acad. Radiol.*, vol. 15, no. 4, pp. 408–416, Apr. 2008.

[12] E. Wellings, L. Vassiliades, and R. Abdalla, “Breast Cancer Screening for High-Risk Patients of Different Ages and Risk - Which Modality Is Most Effective?,” *Cureus*, vol. 8, no. 12.

[13] J. Melnikow *et al.*, *Supplemental Screening for Breast Cancer in Women With Dense Breasts: A Systematic Review for the U.S. Preventive Service Task Force*. Rockville (MD): Agency for Healthcare Research and Quality (US), 2016.

[14] C. C. Riedl *et al.*, “Triple-Modality Screening Trial for Familial Breast Cancer Underlines the Importance of Magnetic Resonance Imaging and Questions the Role of Mammography and Ultrasound Regardless of Patient Mutation Status, Age, and Breast Density,” *J. Clin. Oncol.*, vol. 33, no. 10, pp. 1128–1135, Apr. 2015.

[15] S. C. Partridge *et al.*, “Improved diagnostic accuracy of breast MRI through combined apparent diffusion coefficients and dynamic contrast-enhanced kinetics,” *Magn. Reson. Med.*, vol. 65, no. 6, pp. 1759–1767, Jun. 2011.

[16] M. L. Marinovich *et al.*, “Early prediction of pathologic response to neoadjuvant therapy in breast cancer: Systematic review of the accuracy of MRI,” *The Breast*, vol. 21, no. 5, pp. 669–677, Oct. 2012.

[17] S. J. Lord *et al.*, “A systematic review of the effectiveness of magnetic resonance imaging (MRI) as an addition to mammography and ultrasound in screening young women at high risk of breast cancer,” *Eur. J. Cancer*, vol. 43, no. 13, pp. 1905–1917, Sep. 2007.

[18] *Dynamic Contrast-Enhanced Magnetic Resonance Imaging in Oncology | Alan Jackson | Springer*. .

[19] H. Poptani, N. Bansal, R. A. Graham, A. Mancuso, D. S. Nelson, and J. D. Glickson, “Detecting early response to cyclophosphamide treatment of RIF-1 tumors using selective multiple quantum spectroscopy (SelMQC) and dynamic contrast enhanced imaging,” *NMR Biomed.*, vol. 16, no. 2, pp. 102–111, Apr. 2003.

[20] P. S. Tofts and A. G. Kermode, “Measurement of the blood-brain barrier permeability and leakage space using dynamic MR imaging. 1. Fundamental concepts,” *Magn. Reson. Med.*, vol. 17, no. 2, pp. 357–367, Feb. 1991.

[21] P. S. Tofts *et al.*, “Estimating kinetic parameters from dynamic contrast-enhanced t1-weighted MRI of a diffusable tracer: Standardized quantities and symbols,” *J. Magn. Reson. Imaging*, vol. 10, no. 3, pp. 223–232, Sep. 1999.

[22] H. Yabuuchi *et al.*, “Non-mass-like enhancement on contrast-enhanced breast MR imaging: Lesion characterization using combination of dynamic contrast-enhanced and diffusion-weighted MR images,” *Eur. J. Radiol.*, vol. 75, no. 1, pp. e126–e132, Jul. 2010.

[23] T. H. O. Munnink *et al.*, “Molecular imaging of breast cancer,” *The Breast*, vol. 18, pp. S66–S73, Oct. 2009.

[24] H. Revets, P. D. Baetselier, and S. Muyldermans, “Nanobodies as novel agents for cancer therapy,” *Expert Opin. Biol. Ther.*, vol. 5, no. 1, pp. 111–124, Jan. 2005.

[25] K. J. Jørgensen, J. D. Keen, and P. C. Gøtzsche, “Is Mammographic Screening Justifiable Considering Its Substantial Overdiagnosis Rate and Minor Effect on Mortality?,” *Radiology*, vol. 260, no. 3, pp. 621–627, Sep. 2011.

[26] “What Is Coronary Heart Disease?” [Online]. Available: https://www.nhlbi.nih.gov/health/health-topics/topics/cad. [Accessed: 28-May-2017].

[27] *Clinical Cardiac MRI* | *Jan Bogaert* | *Springer*. .

[28] D. J. Atkinson, D. Burstein, and R. R. Edelman, “First-pass cardiac perfusion: evaluation with ultrafast MR imaging.,” *Radiology*, vol. 174, no. 3, pp. 757–762, Mar. 1990.

[29] N. Wilke *et al.*, “Myocardial perfusion reserve: assessment with multisection, quantitative, first-pass MR imaging.,” *Radiology*, vol. 204, no. 2, pp. 373–384, Aug. 1997.

[30] J. Rieber *et al.*, “Cardiac magnetic resonance perfusion imaging for the functional assessment of coronary artery disease: a comparison with coronary angiography and fractional flow reserve,” *Eur. Heart J.*, vol. 27, no. 12, pp. 1465–1471, Jun. 2006.

[31] P. Kellman, F. H. Epstein, and E. R. McVeigh, “Adaptive sensitivity encoding incorporating temporal filtering (TSENSE)†,” *Magn. Reson. Med.*, vol. 45, no. 5, pp. 846–852, May 2001.

[32] J. Tsao, P. Boesiger, and K. P. Pruessmann, “k-t BLAST and k-t SENSE: Dynamic MRI with high frame rate exploiting spatiotemporal correlations,” *Magn. Reson. Med.*, vol. 50, no. 5, pp. 1031–1042, Nov. 2003.

[33] R. Otazo, D. Kim, L. Axel, and D. K. Sodickson, “Combination of compressed sensing and parallel imaging for highly accelerated first-pass cardiac perfusion MRI,” *Magn. Reson. Med.*, vol. 64, no. 3, pp. 767–776, Sep. 2010.

[34] F. Schmitt *et al.*, “3 Tesla MRI: successful results with higher field strengths,” *Radiol.*, vol. 44, no. 1, pp. 31–47, Jan. 2004.

[35] K. T. Baudendistel, J. T. Heverhagen, and M. V. Knopp, “Clinical MR at 3 Tesla: current status,” *Radiol.*, vol. 44, no. 1, pp. 11–18, Jan. 2004.

[36] J. Alvarez-Linera, “3 T MRI: Advances in brain imaging,” *Eur. J. Radiol.*, vol. 67, no. 3, pp. 415–426, Sep. 2008.

[37] T. S. Ibrahim, R. Lee, B. A. Baertlein, Y. Yu, and P.-M. L. Robitaille, “Computational analysis of the high pass birdcage resonator: finite difference time domain simulations for high-field MRI,” *Magn. Reson. Imaging*, vol. 18, no. 7, pp. 835–843, 2000.

[38] T. S. Ibrahim, R. Lee, A. M. Abduljalil, B. A. Baertlein, and P. M. Robitaille, “Dielectric resonances and B(1) field inhomogeneity in UHFMRI: computational analysis and experimental findings,” *Magn. Reson. Imaging*, vol. 19, no. 2, pp. 219–226, Feb. 2001.

[39] C. M. Collins, W. Liu, W. Schreiber, Q. X. Yang, and M. B. Smith, “Central brightening due to constructive interference with, without, and despite dielectric resonance,” *J. Magn. Reson. Imaging*, vol. 21, no. 2, pp. 192–196, Feb. 2005.

[40] U. Katscher, P. Börnert, C. Leussler, and J. S. van den Brink, “Transmit SENSE,” *Magn. Reson. Med.*, vol. 49, no. 1, pp. 144–150, Jan. 2003.

[41] Y. Zhu, “Parallel excitation with an array of transmit coils,” *Magn. Reson. Med.*, vol. 51, no. 4, pp. 775–784, 2004.

[42] P. Ullmann, S. Junge, M. Wick, F. Seifert, W. Ruhm, and J. Hennig, “Experimental analysis of parallel excitation using dedicated coil setups and simultaneous RF transmission on multiple channels,” *Magn. Reson. Med.*, vol. 54, no. 4, pp. 994–1001, Oct. 2005.

[43] Y. Zhu and R. Giaquinto, “Improving flip angle uniformity with parallel excitation,” in *Proc. Intl. Soc. Mag. Reson. Med*, 2005, vol. 13, p. 2752.

[44] K. Setsompop *et al.*, “Parallel RF transmission with eight channels at 3 Tesla,” *Magn. Reson. Med.*, vol. 56, no. 5, pp. 1163–1171, Nov. 2006.

[45] W. Grissom, C. Yip, Z. Zhang, V. A. Stenger, J. A. Fessler, and D. C. Noll, “Spatial domain method for the design of RF pulses in multicoil parallel excitation,” *Magn. Reson. Med.*, vol. 56, no. 3, pp. 620–629, Sep. 2006.

[46] U. Fontius, “A flexible 8-channel RF transmit array system for parallel excitation,” in *Proc. Intl. Soc. Mag. Reson. Med*, 2006, p. 127.

[47] I. Graesslin *et al.*, “Whole body 3T MRI system with eight parallel RF transmission channels,” in *Proc. Intl. Soc. Mag. Reson. Med*, 2006, p. 129.

[48] D. A. Feinberg, R. Turner, P. D. Jakab, and M. von Kienlin, “Echo-planar imaging with asymmetric gradient modulation and inner-volume excitation,” *Magn. Reson. Med. Off. J. Soc. Magn. Reson. Med. Soc. Magn. Reson. Med.*, vol. 13, no. 1, pp. 162–169, Jan. 1990.

[49] V. Alagappan *et al.*, “Degenerate mode band-pass birdcage coil for accelerated parallel excitation,” *Magn. Reson. Med.*, vol. 57, no. 6, pp. 1148–1158, Jun. 2007.

[50] G. Adriany *et al.*, “A 32-channel lattice transmission line array for parallel transmit and receive MRI at 7 tesla,” *Magn. Reson. Med.*, vol. 63, no. 6, pp. 1478–1485, Jun. 2010.

[51] K. M. Gilbert, A. T. Curtis, J. S. Gati, L. Martyn Klassen, L. E. Villemaire, and R. S. Menon, “Transmit/receive radiofrequency coil with individually shielded elements,” *Magn. Reson. Med.*, vol. 64, no. 6, pp. 1640–1651, Dec. 2010.

[52] J. T. Vaughan *et al.*, “Whole-body imaging at 7T: Preliminary results,” *Magn. Reson. Med.*, vol. 61, no. 1, pp. 244–248, Jan. 2009.

[53] I. Graesslin, S. Biederer, F. Schweser, K. H. Zimmermann, U. Katscher, and P. Börnert, “SAR reduction for parallel transmission using VERSE and k-space filtering,” in *Proc. Intl. Soc. Mag. Reson. Med*, 2007, p. 674.

[54] X. Wu, C. Akgun, J. T. Vaughan, K. Ugurbil, and P. F. Van de Moortele, “SAR reduction in transmit SENSE using adapted excitation k-space trajectories,” in *Proc. Intl. Soc. Mag. Reson. Med*, 2007, p. 673.

[55] Y. Liu, K. Feng, M. P. McDougall, S. M. Wright, and J. Ji, “Reducing SAR in parallel excitation using variable-density spirals: a simulation-based study,” *Magn. Reson. Imaging*, vol. 26, no. 8, pp. 1122–1132, Oct. 2008.

[56] D. Lee, M. Lustig, W. A. Grissom, and J. M. Pauly, “Time-optimal design for multidimensional and parallel transmit variable-rate selective excitation,” *Magn. Reson. Med.*, vol. 61, no. 6, pp. 1471–1479, Jun. 2009.

[57] M. A. Cloos, M. Luong, G. Ferrand, A. Amadon, D. Le Bihan, and N. Boulant, “Local SAR reduction in parallel excitation based on channel-dependent Tikhonov parameters,” *J. Magn. Reson. Imaging*, vol. 32, no. 5, pp. 1209–1216, Nov. 2010.

[58] D. O. Brunner and K. P. Pruessmann, “Optimal design of multiple-channel RF pulses under strict power and SAR constraints,” *Magn. Reson. Med.*, vol. 63, no. 5, pp. 1280–1291, May 2010.

[59] X. Wu *et al.*, “Adapted RF pulse design for SAR reduction in parallel excitation with experimental verification at 9.4 T,” *J. Magn. Reson.*, vol. 205, no. 1, pp. 161–170, 2010.

[60] P.-S. Wei, M. J. Smith, C. P. Bidinisti, J. Matwiy, and S. B. King, “Impact of coupling in Tx-array coil design for transmit SENSE at 3T,” in *Proc. Intl. Soc. Mag. Reson. Med*, 2014, p. 0549.

[61] P.-S. Wei, S. B. King, M. J. Smith, J. Matwiy, and C. P. Bidinosti, “Accurate phased array modeling in the presence of coupling,” in *Proc. Intl. Soc. Mag. Reson. Med*, 2013, p. 2721.

[62] P.-S. Wei, M. J. Smith, C. P. Bidinisti, and S. B. King, “Tx-array design strategies for reducing excitation artifact and local SAR hot spots in pTx MRI,” in *Proc. Intl. Soc. Mag. Reson. Med*, 2015, p. 3171.

[63] E. M. Haacke, R. W. Brown, M. R. Thompson, and R. Venkatesan, *Magnetic Resonance Imaging: Physical Principles and Sequence Design*. Wiley, 1999.

[64] Z.-P. Liang and P. C. Lauterbur, *Principles of Magnetic Resonance Imaging: A Signal Processing Perspective*. Wiley, 1999.

[65] M. A. Bernstein, K. F. King, and X. J. Zhou, *Handbook of MRI Pulse Sequences*. Elsevier, 2004.

[66] F. E. Terman, *Electronic and Radio Engineering. 4th Ed. by Frederick Emmons Terman, Assisted by Robert Arthur Helliwell and Others*. 1955.

[67] J. Mispelter, M. Lupu, and A. Briguet, *NMR Probeheads for Biophysical and Biomedical Experiments: Theoretical Principles and Practical Guidelines*. World Scientific Publishing Co Inc, 2015.

[68] C. Bowick, *RF Circuit Design*. Newnes, 2014.

[69] J. T. Vaughan and J. R. Griffiths, *RF Coils for MRI*. John Wiley & Sons, 2012.

[70] “Magnetic Resonance Imaging Handbook,” *CRC Press*, 22-Sep-2016. [Online]. Available:https://www.crcpress.com/Magnetic-Resonance-Imaging-Handbook/Saba/p/book/9781482216288. [Accessed: 09-Jul-2017].

[71] D. Christensen, C. Furse, and C. Durney, *Basic Introduction to Bioelectromagnetics, Second Edition*. CRC Press, 2009.

[72] B. Greenebaum and F. S. Barnes, *Bioengineering and Biophysical Aspects of Electromagnetic Fields*. CRC Press, 2006.

[73] “Criteria for Significant Risk Investigations of Magnetic Resonance Diagnostic Devices,” U.S Food and Drug Administration, 2014.

[74] J. Jin, *Electromagnetic Analysis and Design in Magnetic Resonance Imaging*. CRC Press, 1998.

[75] K. S. Yee and others, “Numerical solution of initial boundary value problems involving Maxwell’s equations in isotropic media,” *IEEE Trans Antennas Propag*, vol. 14, no. 3, pp. 302–307, 1966.

[76] T. Namiki, “A new FDTD algorithm based on alternating-direction implicit method,” *Microw. Theory Tech. IEEE Trans. On*, vol. 47, no. 10, pp. 2003–2007, 1999.

[77] T. Rylander, P. Ingelström, and A. Bondeson, *Computational Electromagnetics*. Springer New York, 2013.

[78] L. Sevgi, *Electromagnetic Modeling and Simulation*. John Wiley & Sons, 2014.

[79] A. Taflove and S. C. Hagness, *Computational Electrodynamics: The Finite-difference Time-domain Method*. Artech House, 2005.

[80] D. M. Sullivan, *Electromagnetic Simulation Using the FDTD Method*. John Wiley & Sons, 2013.

[81] Y. Hao and R. Mittra, *FDTD Modeling of Metamaterials: Theory and Applications*. Artech House, 2008.

[82] W. Yu, *Advanced FDTD Methods : Parallelization, Acceleration, and Engineering Applications*. Artech House, 2011.

[83] H. Bruns, C. Schuster, and H. Singer, “Numerical Electromagnetic Field Analysis for EMC Problems,” *IEEE Trans. Electromagn. Compat.*, vol. 49, no. 2, pp. 253–262, May 2007.

[84] D. I. Hoult, “The principle of reciprocity in signal strength calculations—A mathematical guide,” *Concepts Magn. Reson.*, vol. 12, no. 4, pp. 173–187, Jan. 2000.

[85] P. B. Roemer, W. A. Edelstein, C. E. Hayes, S. P. Souza, and O. M. Mueller, “The NMR phased array,” *Magn. Reson. Med.*, vol. 16, no. 2, pp. 192–225, 1990.

[86] S. B. King, S. M. Varosi, and G. R. Duensing, “Eigenmode analysis for understanding phased array coils and their limits,” *Concepts Magn. Reson. Part B Magn. Reson. Eng.*, vol. 29B, no. 1, pp. 42–49, Feb. 2006.

[87] C. E. Hayes and P. B. Roemer, “Noise correlations in data simultaneously acquired from multiple surface coil arrays,” *Magn. Reson. Med.*, vol. 16, no. 2, pp. 181–191, Nov. 1990.

[88] G. R. Duensing, H. R. Brooker, and J. R. Fitzsimmons, “Maximizing Signal-to-Noise Ratio in the Presence of Coil Coupling,” *J. Magn. Reson. B*, vol. 111, no. 3, pp. 230–235, Jun. 1996.

[89] K. P. Pruessmann, M. Weiger, M. B. Scheidegger, P. Boesiger, and others, “SENSE: sensitivity encoding for fast MRI,” *Magn. Reson. Med.*, vol. 42, no. 5, pp. 952–962, 1999.

[90] J. W. Carlson, “Power deposition and noise correlation in NMR samples,” *Magn. Reson. Med.*, vol. 10, no. 3, pp. 399–403, Jun. 1989.

[91] S. M. Wright and L. L. Wald, “Theory and application of array coils in MR spectroscopy,” *NMR Biomed.*, vol. 10, no. 8, pp. 394–410, Dec. 1997.

[92] P. J. Petersan and S. M. Anlage, “Measurement of resonant frequency and quality factor of microwave resonators: Comparison of methods,” *J. Appl. Phys.*, vol. 84, no. 6, pp. 3392–3402, Sep. 1998.

[93] R. G. Pinkerton, E. A. Barberi, and R. S. Menon, “Noise properties of a NMR transceiver coil array,” *J. Magn. Reson.*, vol. 171, no. 1, pp. 151–156, Nov. 2004.

[94] M. A. Ohliger, P. Ledden, C. A. McKenzie, and D. K. Sodickson, “Effects of inductive coupling on parallel MR image reconstructions,” *Magn. Reson. Med.*, vol. 52, no. 3, pp. 628–639, 2004.

[95] C. D. Constantinides, E. Atalar, and E. R. McVeigh, “Signal-to-noise measurements in magnitude images from NMR phased arrays,” *Magn. Reson. Med.*, vol. 38, no. 5, pp. 852–857, Nov. 1997.

[96] D. K. Sodickson and W. J. Manning, “Simultaneous acquisition of spatial harmonics (SMASH): Fast imaging with radiofrequency coil arrays,” *Magn. Reson. Med.*, vol. 38, no. 4, pp. 591–603, Oct. 1997.

[97] M. A. Griswold *et al.*, “Generalized autocalibrating partially parallel acquisitions (GRAPPA),” *Magn. Reson. Med.*, vol. 47, no. 6, pp. 1202–1210, Jun. 2002.

[98] A. Christ *et al.*, “The Virtual Family—development of surface-based anatomical models of two adults and two children for dosimetric simulations,” *Phys. Med. Biol.*, vol. 55, no. 2, p. N23, 2010.

[99] D. Stokes, *Principles and Practice of Variable Pressure: Environmental Scanning Electron Microscopy (VP-ESEM)*. John Wiley & Sons, 2008.

[100] D. I. Hoult, “Sensitivity and Power Deposition in a High-Field Imaging Experiment,” *J. Magn. Reson. Imaging*, vol. 12, no. 1, pp. 46–67, 2000.

[101] T. S. Ibrahim, R. Lee, B. A. Baertlein, A. M. Abduljalil, H. Zhu, and P.-M. L. Robitaille, “Effect of RF coil excitation on field inhomogeneity at ultra high fields: a field optimized TEM resonator,” *Magn. Reson. Imaging*, vol. 19, no. 10, pp. 1339–1347, 2001.

[102] P. Ullmann, S. Junge, M. Wick, W. Ruhm, and J. Hennig, “Experimental verification of transmit SENSE with simultaneous RF-transmission on multiple channels,” in *Proc. Intl. Soc. Mag. Reson. Med*, 2005, p. 15.

[103] W. M. Brink, V. Gulani, and A. G. Webb, “Clinical applications of dual-channel transmit MRI: A review,” *J. Magn. Reson. Imaging*, vol. 42, no. 4, pp. 855–869, Oct. 2015.

[104] W. A. Willinek *et al.*, “Dual-source parallel radiofrequency excitation body MR imaging compared with standard MR imaging at 3.0 T: initial clinical experience 1,” *Radiology*, vol. 256, no. 3, pp. 966–975, 2010.

[105] R. Krishnamurthy, A. Pednekar, M. Kouwenhoven, B. Cheong, and R. Muthupillai, “Evaluation of a Subject specific dual-transmit approach for improving B1 field

homogeneity in cardiovascular magnetic resonance at 3T," *J. Cardiovasc. Magn. Reson.*, vol. 15, p. 68, 2013.

[106] M. J. Smith *et al.*, "Improved Parallel Imaging using Small FOV Excitation on an 8-Channel Transmit Array System," in *Proc. Intl. Soc. Mag. Reson. Med*, 2008, vol. 16, p. 1086.

[107] U. Katscher, P. Börnert, and J. S. van den Brink, "Theoretical and numerical aspects of transmit SENSE," *Med. Imaging IEEE Trans. On*, vol. 23, no. 4, pp. 520–525, 2004.

[108] U. Katscher and P. Börnert, "Parallel RF transmission in MRI," *NMR Biomed.*, vol. 19, no. 3, pp. 393–400, May 2006.

[109] L. N. Tanenbaum, "Clinical 3T MR Imaging: Mastering the Challenges," *Magn. Reson. Imaging Clin. N. Am.*, vol. 14, no. 1, pp. 1–15, Feb. 2006.

[110] C. A. T. Van den Berg *et al.*, "Simultaneous B 1+ homogenization and specific absorption rate hotspot suppression using a magnetic resonance phased array transmit coil," *Magn. Reson. Med.*, vol. 57, no. 3, pp. 577–586, Mar. 2007.

[111] Y. Zhu, L. Alon, C. M. Deniz, R. Brown, and D. K. Sodickson, "System and SAR characterization in parallel RF transmission," *Magn. Reson. Med.*, vol. 67, no. 5, pp. 1367–1378, May 2012.

[112] A. Beqiri, J. W. Hand, J. V. Hajnal, and S. J. Malik, "Comparison between simulated decoupling regimes for specific absorption rate prediction in parallel transmit MRI," *Magn. Reson. Med.*, vol. 74, no. 5, pp. 1423–1434, Nov. 2015.

[113] E. K. Insko and L. Bolinger, "Mapping of the Radiofrequency Field," *J. Magn. Reson. A*, vol. 103, no. 1, pp. 82–85, Jun. 1993.

[114] C. J. Hardy, J. S. Pelc, Y. Zhu, J. E. Piel, R. O. Giaquinto, and D. K. Sodickson, "Low Coupling With Low g Factor Using Venetian-Blind Arrays," in *Proc. Intl. Soc. Mag. Reson. Med*, 2005, p. 675.

[115] J. M. Santos *et al.*, "Single breath-hold whole-heart MRA using variable-density spirals at 3t," *Magn. Reson. Med.*, vol. 55, no. 2, pp. 371–379, Feb. 2006.

[116] F. Padormo, A. Beqiri, J. V. Hajnal, and S. J. Malik, "Parallel transmission for ultrahigh-field imaging," *NMR Biomed.*, vol. 29, no. 9, pp. 1145–1161, Sep. 2016.

[117] T. W. Redpath, “Noise correlation in multicoil receiver systems,” *Magn. Reson. Med.*, vol. 24, no. 1, pp. 85–89, Mar. 1992.

[118] R. Brown, Y. Wang, P. Spincemaille, and R. F. Lee, “On the noise correlation matrix for multiple radio frequency coils,” *Magn. Reson. Med.*, vol. 58, no. 2, pp. 218–224, Aug. 2007.

[119] R. Mittra, *Computational Electromagnetics: Recent Advances and Engineering Applications*. Springer Science & Business Media, 2013.

[120] A. F. Peterson, S. L. Ray, and R. Mittra, *Computational Methods for Electromagnetics*. Wiley, 1998.

[121] X.-Q. Sheng and W. Song, *Essentials of Computational Electromagnetics*. John Wiley & Sons, 2012.

[122] R. F. Harrington, *Introduction to Electromagnetic Engineering*. Courier Dover Publications, 2003.

[123] J.-M. Jin, *Theory and Computation of Electromagnetic Fields*. John Wiley & Sons, Inc., 2010.

[124] R. Garg, *Analytical and Computational Methods in Electromagnetics*. Boston: Artech House, 2008.

[125] J.-M. Jin, *The Finite Element Method in Electromagnetics*. John Wiley & Sons, 2015.

[126] J. L. Volakis, A. Chatterjee, and L. C. Kempel, *Finite element method for electromagnetics: antennas, microwave circuits, and scattering applications*. IEEE Press, 1998.

[127] J.-M. Jin and D. J. Riley, *Finite Element Analysis of Antennas and Arrays*. John Wiley & Sons, 2009.

[128] Olek C. Zienkiewicz, *The Finite Element Method Its Basis and Fundamentals*, 6th ed.. Burlington: Elsevier Science, 2005.

[129] D. H. Schaubert, D. R. Wilton, and A. W. Glisson, “A tetrahedral modeling method for electromagnetic scattering by arbitrarily shaped inhomogeneous dielectric bodies,” *IEEE Trans. Antennas Propag.*, vol. 32, no. 1, pp. 77–85, Jan. 1984.

[130] R. F. Harrington, *Field Computation by Moment Methods*. IEEE, 1996.

[131] J. Volakis and K. Sertel, *Integral Equation Methods for Electromagnetics*. Institution of Engineering and Technology, 2012.

[132] W. C. Gibson, *The Method of Moments in Electromagnetics, Second Edition*. CRC Press, 2014.

[133] S. D. Gedney, *Introduction to the Finite-Difference Time-Domain (FDTD) Method for Electromagnetics*. Morgan & Claypool Publishers, 2011.

[134] U. S. Inan and R. A. Marshall, *Numerical Electromagnetics: The FDTD Method*. Cambridge University Press, 2011.

[135] Schneider John B., "Understanding the Finite-Difference Time-Domain.pdf." www.eecs.wsu.edu/~schneidj/ufdtd, 2010.

[136] R. F. Harrington, *Time-Harmonic Electromagnetic Fields*. Wiley, 2001.

[137] T. Hubing, C. Su, H. Zeng, and H. Ke, "Survey of Current Computational Electromagnetics Techniques and Software," Clemson Vehicular Electronics Laboratory, Technical Report: CVEL-08-011.2, 2008.

[138] D. S. H. Lo, *Finite Element Mesh Generation*. CRC Press, 2015.

[139] W. Gibson, *The Method of Moments in Electromagnetics, Second Edition*. Chapman and Hall/CRC, 2014.

[140] A. Pyzara, B. Bylina, and J. Bylina, "The influence of a matrix condition number on iterative methods' convergence," in *2011 Federated Conference on Computer Science and Information Systems (FedCSIS)*, 2011, pp. 459–464.

[141] E. Cheney and D. Kincaid, *Numerical Mathematics and Computing*. Cengage Learning, 2012.

[142] Q. H. Liu, Y. Lin, J. Liu, J.-H. Lee, and E. Simsek, "A 3-D Spectral Integral Method (SIM) for Surface Integral Equations," *IEEE Microw. Wirel. Compon. Lett.*, vol. 19, no. 2, pp. 62–64, Feb. 2009.

[143] H. Liu and D. Jiao, "A direct finite-element-based solver of significantly reduced complexity for solving large-scale electromagnetic problems," presented at the Microwave Symposium Digest, 2009. MTT '09. IEEE MTT-S International, 2009, pp. 177–180.